UNIVERSITY OF CALIFORNIA, SAN DIEGO

Exploring Heavy Fermion Materials near a Quantum Critical Point

A dissertation submitted in partial satisfaction of the
requirements for the degree Doctor of Philosophy

in

Materials Science and Engineering

by

Sooyoung Jang

Committee in charge:

Professor M. Brian Maple, Chair
Professor Renkun Chen
Professor Eric E. Fullerton
Professor Oleg Shpyrko
Professor Sunil K. Sinha

2015

The dissertation of Sooyoung Jang is approved, and it is acceptable in quality and form for publication on microfilm and electronically:

Chair

University of California, San Diego

2015

DEDICATION

To my parents and my wonderful husband Jinkyu

TABLE OF CONTENTS

Signature Page . . . iii

Dedication . . . iv

Table of Contents . . . v

List of Figures . . . vii

Acknowledgements . . . x

Vita . . . xii

Abstract of the Dissertation . . . xiv

I Introduction . . . 1
I. A. Strongly Correlated Electron Behavior . . . 1
I. A. 1. Kondo effect . . . 1
I. A. 2. Fermi Liquid Theory . . . 5
I. A. 3. Heavy Fermions . . . 6
I. B. Quantum Criticality . . . 8
I. B. 1. Doniach Diagram . . . 8
I. B. 2. Non-Fermi liquid behavior . . . 11
Bibliography . . . 12

II Experimental Details . . . 14
II. A. Sample Synthesis . . . 14
II. A. 1. Flux Growth . . . 14
II. B. Characterization . . . 16
II. B. 1. Energy Dispersive X-ray spectroscopy (EDS) . . . 16
II. B. 2. Powder X-ray Diffraction . . . 16
II. B. 3. Electrical Resistivity . . . 17
II. B. 4. Magnetization . . . 17
II. B. 5. Specific Heat . . . 18
Bibliography . . . 18

III Crossover between Fermi liquid and non-Fermi liquid behavior in the non-centrosymmetric compound $Yb_2Ni_{12}P_7$ . . . 20
III. A. Introduction . . . 20
III. B. Experimental details . . . 23
III. C. Result . . . 25
III. C. 1. Crystal structure . . . 25
III. C. 2. Magnetic susceptibility . . . 27

III. C. 3. Electrical resistivity . . . 31
III. C. 4. Specific heat . . . 33
III. C. 5. Thermoelectric power . . . 36
III. D. Discussion . . . 39
III. E. Concluding remarks . . . 42
Bibliography . . . 44

IV Itinerant ferromagnetism in the noncentrosymmetric heavy-fermion compound $Sm_2Ni_{12}P_7$ . . . 47
IV. A. Introduction . . . 47
IV. B. Experimental details . . . 49
IV. C. Results . . . 50
IV. D. Discussion . . . 61
IV. E. Summary . . . 63
Bibliography . . . 65

V Synthesis and characterization of the $Zr_2Fe_{12}P_7$-type compound $Hf_2Fe_{12}P_7$ 68
V. A. Introduction . . . 68
V. B. Experimental details . . . 69
V. C. Results and discussion . . . 72
V. D. Summary . . . 82
Bibliography . . . 84

VI Resolution of the discrepancy between the variation of the physical properties of $Ce_{1-x}Yb_xCoIn_5$ single crystals and thin films with Yb composition 85
VI. A. Introduction . . . 85
VI. B. Experimental details . . . 89
VI. C. Results and discussion . . . 90
VI. C. 1. Estimate of actual Yb concentration using Vegard's law . . . 92
VI. C. 2. EDS, WDS, and TXAS measurements of the actual Yb concentration 95
VI. C. 3. Wavelength dispersive x-ray spectroscopy (WDS) measurements . 98
VI. C. 4. Transmission X-ray absorption spectroscopy (TXAS) measurements 100
VI. C. 5. Correction of the T vs. Yb concentration phase diagram . . . 102
VI. D. Concluding remarks . . . 105
Bibliography . . . 107

LIST OF FIGURES

Figure I.1: Schematic of the "Kondo effect". The total resistance (R_{Total}) is the sum of the lattice contribution (R_{Lattice}) and the magnetic impurity contribution ($R_{\text{Magnetic impurity}}$). 2
Figure I.2: Doniach phase diagram, Temperature, T, vs. $JN(E_F)$. . . 9

Figure II.1: A single crystal of $Yb_2Ni_{12}P_7$ grown using a Sn flux method. with four electric contact for resistivity measurement. Inset shows zoom in picture of $Yb_2Ni_{12}P_7$ to describe hexagonal structure. . . 15

Figure III.1: Unit cell volume vs. Ln element for $Ln_2Ni_{12}P_7$ compounds; open circles are from Ref. [14] and filled circles are from this work. Inset: X-ray diffraction pattern of $Yb_2Ni_{12}P_7$ at room temperature (open squares) and fit from Rietveld refinement (red line). . 26
Figure III.2: a) Magnetic susceptibility, $\chi = M/H$, vs. temperature, T, for magnetic field of $H = 0.5$ T. (b) $\chi^{-1} = H/M$, vs. T for $H \parallel c$ and $H \perp c$. (c) M vs. H for $H \perp c$ at $T = 2$ K, 20 K, and 100 K. 30
Figure III.3: Electrical resistivity, ρ, vs. temperature, T, for $Yb_2Ni_{12}P_7$. The inset displays ρ vs. T^2 data for magnetic fields of $H = 0$ and 9 T applied parallel to the c axis. The solid lines are fits to the data using Eq. (3). 32
Figure III.4: (a) Specific heat, C, divided by temperature, for $Yb_2Ni_{12}P_7$, measured in applied magnetic fields $H = 0$ T and 9 T. (b) C/T vs. T^2 (c) Electronic contribution to specific heat, C_e/T (d) C_e/T plotted on a logarithmic temperature scale. 35
Figure III.5: (a) Thermoelectric power, $S(T)$, for $Yb_2Ni_{12}P_7$ plotted on a semilogarithmic scale. (b) $S(T)$ divided by temperature, $S(T)/T$ 38
Figure III.6: (a) The exponent, n is plotted vs. log T. Inset: ρ vs. T^2 data. (b) $\rho(T)$ data for $Yb_2Ni_{12}P_7$ and $La_2Ni_{12}P_7$. (c) The $4f$ electron contribution to $\rho(T)$ in $Yb_2Ni_{12}P_7$, ρ_{4f}, plotted vs. T. . . 40

Figure IV.1: (a) Magnetization M/H vs. temperature T. M/H data for T between 2 to 300 K are plotted in the inset. (b) Isothermal magnetization M vs. $\mu_0 H$. (c) M vs. $\mu_0 H$ for $\mu_0 H \|$ab-plane. (d) Hysteresis curve at $T = 2$ K in the range -1 $< \mu_0 H <$ 1 T. 51
Figure IV.2: (a) Electrical resistivity ρ vs.T. (b) ρ versus T^3.(c) An arrow highlights the onset of ferromagnetic order. A solid line represents a fit to the $\rho(T)$ data using Eq. (2). 55
Figure IV.3: Specific heat C divided by temperature T for $Sm_2Ni_{12}P_7$ and $Th_2Fe_{12}P_7$. The inset shows C/T data versus T^2 for $Sm_2Ni_{12}P_7$ and $Th_2Fe_{12}P_7$ (scaled). The dashed red lines are linear fits to these data. 58

Figure IV.4: (a) The specific heat $C'(T)/T$. The solid line represents the combined electronic and magnetic entropy, $S(T)$. (b) $C'(T)/T$ data plotted vs. ln$T$ along with best fits of Eq. (3) and Eq. (4) to the data for $T < T_C$. 60

Figure V.1: Powder x-ray diffraction data and Rietveld refinement fit. The space group is $P\overline{6}$ with lattice constants of $a = 9.023$ Å and $c = 3.580$ Å. The arrow indicates a peak that may be related to the presence of a small amount of an impurity phase. 71
Figure V.2: (a) Isothermal magnetization, M, plotted vs. magnetic field, H. (b) The filled squares indicate measured data, while the red solid line represents a fit to the data. 74
Figure V.3: (a) Magnetization, M/H as a function of temperature T. The inset shows the estimated intrinsic M/H. The solid line represents the estimated intrinsic contribution to M/H. (b) H/M as a function of temperature. 76
Figure V.4: (a) Specific heat C divided by temperature T measured in magnetic fields of $H = 0$ T and 9 T. (b) Electronic contribution to the specific heat, C_e/T vs. ln$T$ where the solid line represents a fit of $C_e(T)/T = a(\ln(T_0/T))$. (c) C/T data are plotted vs. T^2. 79
Figure V.5: Electrical resistivity ρ vs. temperature T. The inset shows low temperature ρ vs. $T^{1.2}$. The solid line emphasizes the temperature range over which the temperature dependence of ρ exhibits power law behavior with exponent 1.2. 81

Figure VI.1: (a) Inverse of the residual resistivity ratio (RRR) plotted vs.nominal Yb concentration x. (b) Superconducting critical temperature T_c plotted vs. RRR from the same measurements shown in panel (a). 91
Figure VI.2: Unit cell volume V vs. nominal Yb concentration x for the system $Ce_{1-x}Yb_xCoIn_5$ (filled circles) based on the data of Capan *et al.* [1]. The dashed straight line represents Vegard's law. 94
Figure VI.3: (a) Actual Yb concentration $x_{\rm act}$ vs. nominal Yb concentration x as obtained from reported EDS measurements. (b)$x_{\rm act}$ vs. x based on: (1) Vegard's law analysis (2) EDS measurements (3) WDS measurements (4) TXAS measurements. 96
Figure VI.4: Illustration of method for acquiring EDS data on the single crystals. The dashed lines represent the average value of the data and are denoted as $x_{\rm act}$ in Fig. 3 for each of the two concentrations. 97
Figure VI.5: Results of wavelength dispersive x-ray spectroscopy (WDS) for two representative samples with nominal Yb concentrations x = 0.4 and $x = 1$ and two compounds in which Yb is trivalent, YbF_3 and $YbRh_2Si_2$. 99

Figure VI.6: Plots of the Co K (a) and Yb L_{III} (b) edges after a linear pre-edge subtraction. A straight line fit above the edge shown as a black line, provides an estimate of the step height at the edge. . 101
Figure VI.7: Superconducting critical temperature T_c, determined from measurements of $\rho(T)$ vs. x for $Ce_{1-x}Yb_xCoIn_5$. Single crystals are plotted vs. x, where x represents the nominal concentration. The solid line indicates the evolution of T_c for thin film samples. . 103
Figure VI.8: Coherence temperature T^* and superconducting critical temperature T_c vs. actual Yb composition, x_{act}, for flux grown single crystals [2] and thin films. [6] 104

ACKNOWLEDGEMENTS

First of all, I would like to thank my thesis advisor, Professor M. Brian Maple, for providing me the opportunity to study materials based condensed matter physics and for his continuous support. He is always leading me in the right direction thoughout all the projects. I was honored to meet him and work for him, I shall never forget all of his help. I am also grateful to the other members of my Ph.D committee: Prof. Eric E. Fullerton, Prof. Oleg Shpyrko, Prof. Renkun Chen, and Prof. Sunil K. Sinha.

Additional thanks are extended to present and former Post Doctoral researchers in our group: Pei Chun Ho, Ryan Baumbach, James Hamlin, Marc Janoscheck, Lei Shu, Ben White, Duygu Yazici, and Sheng Ran for assistance and insightful discussions. Their attitude and approach toward research has inspired me to work with them in the lab. Also I would like to thank the other group members, graduate, undergraduate and high school research assistants who helped me during this project, Colin McElroy, Kevin Huang, Ivy Rum, Inho Jeon, Naveen Pouse, Yuankan Fang, Christian Wolowiec, Adrian Wong, Zak Kmak, and Young Kang. It was a great pleasure to work with them in the lab. I would also like to thank my research collaborators, Professor Frank Bridges at UC Santa Cruz, Dr. Steve Disseler at NIST, and Dr. Meigan Aronson at Stony Brook University/BNL for their important contributions to our research collaborations.

This work was made possible by the unconditional love of my parents, my brother's family, including Sunwoo, and my parents-in-law, whose support and encouragement were invaluable in helping me adjust to living in the US and pursuing my degree. I could not survive in the US without their support. Finally, I would like to thank my husband, Jinkyu, who will always be with me and who helped me overcome the challenges and hurdles associated with earning a Ph. D degree.

A portion of the text and data presented in Chapter 3 are reprints of material that appears in "Crossover between Fermi liquid and non-Fermi liquid

behavior in the non-centrosymmetric compound $Yb_2Ni_{12}P_7$," S. Jang, B. D. White, P.-C. Ho, N. Kanchanavatee, M. Janoscheck, and M. B. Maple, J. Phys.: Condens. Matter **26**, 425601 (2014). The dissertation author was the first author of the article.

A portion of the text and data presented in Chapter 4 are reprints of material that appears in "Resolution of the discrepancy between the variation of the physical properties of $Ce_{1-x}Yb_xCoIn_5$ single crystals and thin films with Yb composition", S. Jang, B. D. White, I. K. Lum, H. Kim, M. A. Tanatar, W. E. Staszheim, R. Prozorov, T. Keiber, F. Bridges, L. Shu, R. E. Baumbach, M. Janoscheck, and M. B. Maple, Philosophical Magazine **94**, 4219 (2014). The dissertation author was the first author of the article.

VITA

2008	B. S. in Materials Science and Engineering Korea University, Seoul, South Korea
2010	M. S in Materials Science and Engineering Korea University, Seoul, South Korea
2015	Ph. D in Materials Science and Engineering University of California, San Diego

PUBLICATIONS

Soo Young Jang, S. H. Lim, and S. R. Lee "Magnetic dead layer in amorphous CoFeB layers with various top and bottom structures", *J. Appl. Phys.* **107**, 09C707, 2010.

Soo Young Jang , Chun-Yoel You, S. H. Lim, and S. R. Lee "Annealing effects on the magnetic dead layer and saturation magnetization in unit structures relevant to a synthetic ferromagnetic free structure", *J. Appl. Phys.* **109**, 013902. 2011.

B. D. White, M. Janoschek, N. Kanchanavatee, K. Huang, L. Shu, S. Jang, D. Yazici, J. J. Hamlin, I. K. Lum, R. E. Baumbach, and M. B. Maple "Thermoelectric Properties of Correlated Electron Systems $Ln_3Pt_3Ge_6$ and $LnPt_4Ge_{12}$ (Ln = Ce, Pr) and Non Centrosymmetric $X_2T_{12}P_7$ (X= Yb, Hf and T = Fe, Co)", *New Materials for Thermoelectric Applications: Theory and Experiment, Conference Proceedings* , 2013.

S. Jang, B. D. White, P.-C. Ho, N. Kanchanavatee, M. Janoscheck, J. J. Hamlin, and M. B. Maple "Crossover between Fermi liquid and non-Fermi liquid behavior in the non centrosymmetric compound $Yb_2Ni_{12}P_7$", *J. Phys.: Condens. Matter* **26**, 425601 2014.

S. Jang, B. D. White, I. K. Lum, H. Kim, M. A. Tanatar, W. E. Straszheim, R. Prozorov, T. Keiber, F. Bridges, L. Shu, R. E. Baumbach, M. Janoscheck, M. B. Maple "Resolution of the discrepancy between the variation of the physical properties of $Ce_{1-x}Yb_xCoIn_5$ single crystals and thin films with Yb composition", *Philosophical Magazine DOI: 10.1080/14786435.2014.976287*, 2014.

D. Yazici, S. Jang, J. J. Hamlin, M. Janoscheck, and M. B. Maple "Effect of Co Substitution on the physics properties of $Hf_2Fe_{12}P_7$", (In preparation).

S. Jang, J. J. Hamlin, M. Janoscheck, B. D. White, D. Yazici, and M. B. Maple, "Synthesis and characterisation of the $Zr_2Fe_{12}P_7$-type compound $Hf_2Fe_{12}P_7$" (in preparation).

S. Jang, B. D. White, D. Yazici, C. A. McElory, Young H. Kang, and M. B. Maple, "Itinerant ferromagnetism in the noncentrosymmetric heavy-fermion compound of $Sm_2Ni_{12}P_7$" (In preparation).

S. Jang, B. D. White, P.-C. Ho, N. Kanchanavatee, M. Janoscheck, D. Yazaci, and M. B. Maple, "Field tuned phase diagram for the heavy fermion compound $Ce_2Ni_{12}As_7$' (In preparation).

S. Jang, B. D. White, D. Yazici, C. A. McElory, and M. B. Maple, "Interplay between superconductivity and antiferromagnetism in $Ce_{1-x}Sm_xCoIn_5$" (In preparation).

S. Jang, B. D. White, and M. B. Maple, "Field tuned magnetic structure and anomalous stability of the Kondo lattice in $Ce_{1-x}Yb_xRhIn_5$" (in preparation).

FIELDS OF STUDY

Major Field: Materials Science and Engineering

Studies in strongly correlated electon materials

M. Brian Maple, Bernd T. Matthias Professor of Physics,

University of California, San Diego

ABSTRACT OF THE DISSERTATION

Exploring Heavy Fermion Materials near a Quantum Critical Point

by

Sooyoung Jang
Doctor of Philosophy in Materials Science and Engineering
University of California, San Diego, 2015
Professor M. Brian Maple, Chair

Results for two categories of heavy fermion systems: (1) a new type of non-centrosymmetric heavy fermion system $R_2TM_{12}Pn_7$ (R = rare earth, TM = transition metal, Pn = P, As), and (2) Yb substitution in $CeCoIn_5$, which is a heavy fermion superconductor, $Ce_{1-x}Yb_xCoIn_5$, are described. The phenomena seen in the system $R_2TM_{12}Pn_7$ are discussed in terms of strong hybridization between the localized f-electron states and the conduction electron states, such as a crossover between Fermi liquid and non-Fermi liquid behavior in $Yb_2Ni_{12}P_7$, or the presence of a large value of the Sommerfeld coefficient, $\gamma \sim 650$ mJ/mol Sm K^2 in $Sm_2Ni_{12}P_7$. The extraordinary electronic phenomena found in the system $Ce_{1-x}Yb_xCoIn_5$ include Yb valence fluctuations, a change in the Fermi surface topology, and suppression of the quantum critical field occurring at a nominal concentration of $x \sim 0.2$. However, the suppression of the superconducting critical temperature with nominal Yb concentration x for bulk single crystals is much weaker than that observed in thin film samples. The actual Yb composition of bulk single crystals is found to be about 1/3 of the nominal concentration, resolving the discrepancy between the variation of the physical properties of $Ce_{1-x}Yb_xCoIn_5$ single crystals and thin films with Yb concertrations.

Chapter I

Introduction

I.A Strongly Correlated Electron Behavior

I.A.1 Kondo effect

In the 1930s, a resistivity minimum was observed at low temperatures for nonmagnetic metals (such as Au, Cu) which contained small amounts of magnetic impurities (such as Fe). [1, 2] This behavior is now known as the "Kondo effect" in which conduction electrons of a metallic host are scattered by magnetic impurity ions via the exchange interaction.

The schematic diagram of the resistance minimum is displayed in Figure I.1. The temperature dependence of the resistance, $R(T)$, shows a logarithmic increase upon cooling below a minimum temperature, $R_{\text{Total}} \sim$ -ln(T). Even though the lattice contribution to the resistance (R_{Lattice}) is decreased with decreasing temperature, the total resistance (R_{Total}) passes through a minimum at a certain temperature due to the increase in resistance with decreasing temperature caused by magnetic impurity scattering ($R_{\text{Magnetic impurity}}$) .

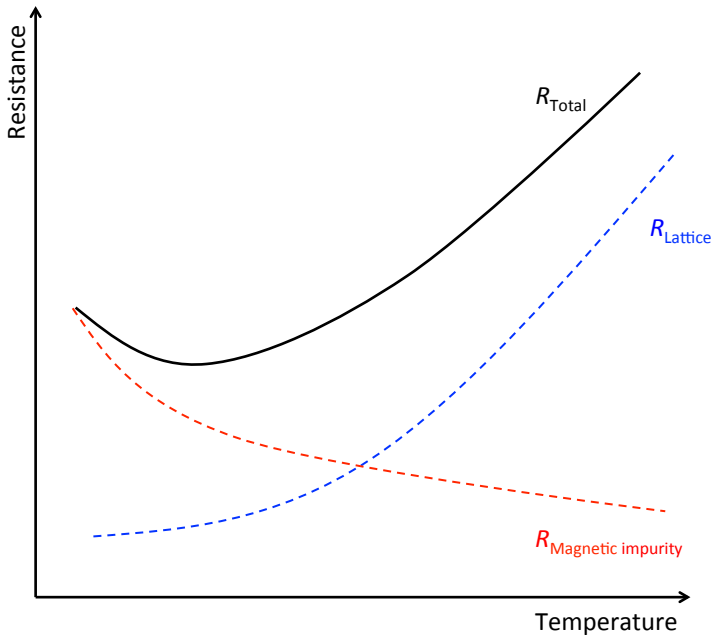

Figure I.1: Schematic of the "Kondo effect". The total resistance (R_{Total}) is the sum of the lattice contribution (R_{Lattice}) and the magnetic impurity contribution ($R_{\text{Magnetic impurity}}$).

There is a long history for explaining this observed minimum in resistivity in dilute alloys, the so-called Kondo problem. Although this phenomenon was reported in the 1930's, theoretical progress was not made until Jun Kondo explained the resistance minimum by using perturbation theory based on the s-d model. [3] An Anderson model was subsequently proposed, [4] by using scaling theory, [5] in which the thermodynamic functions are governed by the single energy scale, T_{Kondo}. In 1966, J. R. Schrieffer and P. A. Wolff [6] demonstrated that the s-d Hamiltonian is analogous to the Anderson model in the case of two spin states which are introduced by on site Coulomb repulsion that are well separated from the Fermi energy E_F. Lastly, the renormalisation group was advocated by K. G. Wilson. [7] Along these lines, the Kondo problem is consistently understood.

Since the s-d exchange Hamiltonian describes the single impurity model, it can be used for explaining Kondo behavior in the electrical resistivity, magnetic susceptibility, and specific heat for $T \gg T_K$ which are given by:

$$\rho_K(T) = AJ^2S(S+1)[1 - JN(E_F)log(D/k_BT)], \tag{I.1}$$

$$\chi_K(T) = \frac{(g\mu_B)^2S(S+1)}{3k_BT}[1 - \frac{2JN(E_F)}{1+2JN(E_F)ln(k_BT/D)} + ...], \tag{I.2}$$

$$C_K(T) = \frac{\pi^2k_BS(S+1)(2JN(E_F))^4}{[1+2JN(E_F)ln(k_BT/D)]^4} + ..., \tag{I.3}$$

where $N(E_F)$ is the electronic density of states for the conduction electron band at the Fermi energy, $N(E_F)$, and D is a cut-off that roughly corresponds to the conduction electron band width. Since it diverge at $T = T_K$, these perturbation calculations hold only for $T \gg T_K$. In a Kondo impurity system, the interactions between impurities are relatively small and the impurity ions that carry the magnetic moments act as independent scatterers at high temperatures. At

low temperatures ($T \ll T_K$), the electrical resistivity saturates to a constant value known as the unitarity limit. [8] As the temperature decreases through T_K, a many body singlet ground states gradually forms in which the magnetic moments of the impurity ion is completely screened away at $T = 0$ K; i.e., the net magnetic moment vanishes and the ground state is nonmagnetic. The ground state behaves as a Fermi liquid in which the $\rho(T)$, $C(T)$, and $\chi(T)$ have the following dependences,

$$\rho(T) = \rho(0)[1 - (T/T_K)^2], \tag{I.4}$$

$$C(T)/T \to \gamma_0 = \text{constant}, \tag{I.5}$$

$$\chi(T) \to \chi_0 = \text{constant}, \tag{I.6}$$

$$\chi_0/\gamma_0 \sim 2. \tag{I.7}$$

On the other hand, for a Kondo lattice, in which the ions that carry a magnetic moment occupy ordered sublattice in the compound, the ions become equivalent when the magnetic moments are compensated by the conduction electron spins as a results of the negative exchange interaction and the resistivity decreases precipitously with decreasing temperature, below a characterisitic "coherence temperature" which is often taken to be the temperature where $\rho(T)$ is a maximum. The terminology "coherence temperature" refers to the formation of the coherent Kondo lattice ground state which can has an enormous value of the γ that can be equal to several J/mol K^2. Such a large value of the γ corresponds to the effective mass of several hundred times of the free electron's mass. So these materials are often called heavy fermion compounds.

I.A.2 Fermi Liquid Theory

Fermi liquid theory was proposed by Landau to describe the low temperature properties of ^{3}He. [9, 10, 11] Landau explained Fermi liquid theory based on the concept of quasiparticles which describe the elementary excitations of an interacting fermion system. When the particles (electrons in this case) are interacted one another, they form a quasiparticle with an effective mass m^*. This situation can be explained by a free electron model and account for systems such as ^{3}He, [12] simple metals (e.g., Cu), and heavy fermion materials even with their strong electronic correlations. Taking account of a few additional parameters, such as the effective mass of an electron which is related to the residual quasiparticle interaction, a Fermi liquid can be considered as a free electron gas. For instance, the Sommerfeld coefficient of the electronic specific heat, Pauli-magnetic susceptibility, and the power laws for electrical resistivity have the specific conditions or values for temperatures well below the Fermi temperature:

$$\frac{C(T)}{T} = (\frac{m^*}{m_e})\gamma_0 = \gamma, \text{ where } \gamma_0 = (\frac{\pi^2 k_B^2}{3})N(E_F) \tag{I.8}$$

$$\chi(T) = (\frac{m^*}{m_e})\frac{\chi_0}{1+F_0^\alpha}, \text{ where } \chi_0 = \mu_B^2 N(E_F) \tag{I.9}$$

$$\rho(T) = \rho_0 + AT^2, \tag{I.10}$$

where k_B, $N(E_F)$, μ_B, F_0^α, and m_e refer to the Boltzmann constant, the electronic density of states at the Fermi energy, the Bohr magneton, an additional Landau parameter, and the free electron mass, respectively. Thus, at low temperatures, γ $(= C/T)$ and χ become constant and the electrical resistivity fits to the T^2 temperature dependence. For typical metals, $m^*/m_e \sim$ 1-10 and $\gamma_0 \sim$ 1-10 mJ/mol K^2.

The phonon contribution should be taken into account and subtracted

from the data when considering the electronic behavior. The lattice contribution is caused by phonon scattering (lattice vibration), which for most materials, becomes dominant as temperature is increased and enhances quantities for $C(T)/T$ and $\rho(T)$. In the case of the Debye model, it assumes that the vibrations are quantized in a solid and can be described by plane waves in a box; in this case, the specific heat is given by,

$$C_{\text{phonon}}(T) = \frac{12\pi^4 N_A k_B}{5\theta_D}(\frac{T}{\theta_D})^3 \tag{I.11}$$

for $T < \theta_D/10$, [13] where N_A is the Avogadro's number, k_B represents Boltzmann's constant, and θ_D is the Debye temperature. θ_D is usually a few hundred kelvin for typical metallic systems. Even though complicated situations are typical for most real materials, a wide range of systems can be well described by using this simple model.

I.A.3 Heavy Fermions

Heavy fermion compounds have received attention for nearly four decades since the discovery of the compound $CeAl_3$. [14] Heavy fermion compounds are usually comprised of actinides, like U, or rare earth elements with valence instability, particularly Ce and Yb and, sometimes, Pr, which have partially filled f-electron shells and hybridize strongly with the conduction electrons at low temperatures. Due to this strong hybridization between f- and d-electrons, the effective mass of electrons can be on the order of 1000 times of the free electron mass, hence, the name "heavy fermion". The Sommerfeld coefficient, γ, can be near 1 J/mol K^2 i.e., three orders of magnitude larger than that of typical metals, like Cu. The direct evidence for the existence of heavy fermion can be established from the observation of quantum oscillations in de Haas van Alphen (dHvA) measurements. [15] Various ground states have been observed in heavy fermion materials, such as long-range magnetic ordering for $CeIn_3$, [28, 17] $CeCu_2Ge_2$, [18] coexistence of magnetic order and superconductivity for UPd_2Al_3, unconventional superconductivity [19]

for UBe_{13}, $CeCoIn_5$, and so called hidden order in URu_2Si_2. One of the most interesting and unexpected phenomenon is unconventional superconductivity. The discovery of superconductivity in $CeCu_2Si_2$ [21] unlocked a new perspective of emergent phenomena which indicate the pairing of the heavy particles. [22]

The Wilson ratio (R_W) [7] and the Kadowaki-Woods ratio (R_{KW}) [23] are useful for characterizing Fermi liquid behaivor. Below the effective Fermi temperature, T_F^*, the behavior of the magnetic susceptibility and specific heat are dependent on the density of state at the Fermi energy. The ratio of magnetic susceptibility and the Sommerfeld coefficient of specific heat is a dimensionaless quantity, the Wilson ratio, R_W, and it can be defined as: [7]

$$R_W = (\frac{\pi^2 k_B^2}{\mu_{eff}^2})[\frac{\chi_0}{\gamma_0}]. \tag{I.12}$$

For a free electron gas, R_W is 1. Experimentally, R_W is typically between 1 and 2 for heavy fermion systems due to the electronic correlations.

The temperature dependence of electrical resistivity predicted by Fermi liquid theory is: $\rho(T) = \rho_0 + AT^2$. Here, the coefficient A can also be scaled with the Sommerfeld coefficient: [23]

$$\frac{A}{\gamma^2} = R_{KW}. \tag{I.13}$$

This expression is called the Kadowaki-Woods ratio. R_{KW} can take on values in the range from 10^{-5} $\mu\Omega$cm (mol K/mJ)^2 to 10^{-7} $\mu\Omega$cm (mol K/mJ)^2 depending on the degeneracy of the f-electron configuration, N. [24] Then, R_{KW} can be fixed to [23]:

$$R_{KW} = \frac{A}{\gamma^2} = \frac{1 \times 10^{-5}}{1/2N(N-1)}\ \mu\Omega cm(molK/mJ)^2. \tag{I.14}$$

I.B Quantum Criticality

I.B.1 Doniach Diagram

The overall behavior of a heavy fermion system can be well explained by a generalized Doniach phase diagram, which describes the competition between the Kondo effect and the RKKY interaction. The Kondo effect, which is responsible for the quenching of the local f-electron moments via the screening by the conduction electrons, [27] can be characterised by an energy scale;,$T_{Kondo} \propto exp(-1/JN(E_F))$. The RKKY interaction, which promotes either long- or short-range magnetic ordering, [25, 26, 27] can be described with energy scale, $T_{RKKY} \propto J^2 g(E_F)$. Here, $N(E_F)$ represents the density of states of the conduction electrons at the Fermi energy and J is the antiferromagnetic interaction between the impurity spins and the conduction electrons. The localized moments and the conduction electrons keep their properties and weakly interact with each other at high temperatures. In contrast, at low temperatures, there are two scenarios: (1) when the RKKY interaction is enhanced relative to the Kondo energy, magnetic ordering emerges, (2) when the Kondo energy is large relative to the RKKY interaction, heavy quasiparticles are formed in a Fermi liquid state which are composites of localzied impurity spins and conduction electrons.[34] The overall physics can be described by the well-known "Doniach phase diagram".[25] When both the RKKY and the Kondo interactions are of comparable magnitude a quantum critical point (QCP) has emerged in this region. The description of the low-temperature state is an intriguing question that remains poorly understood and is the subject of current active research. [27]

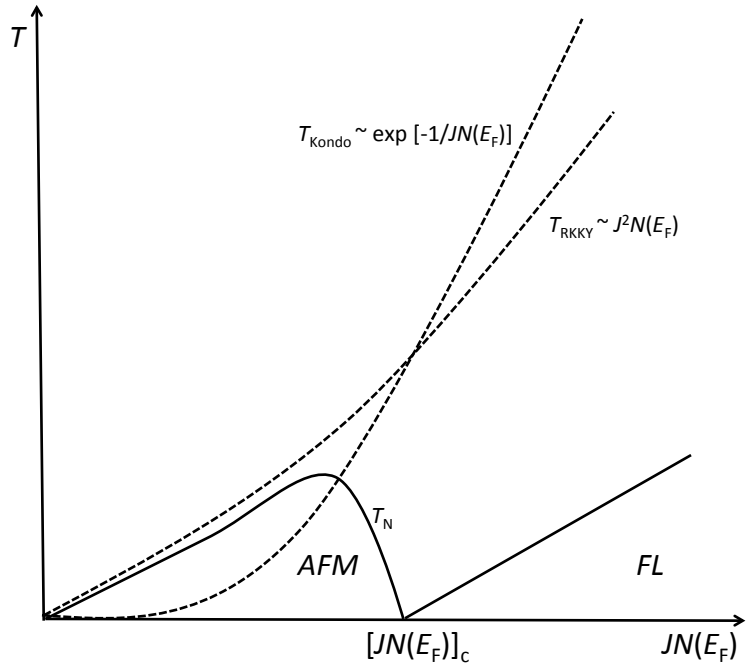

Figure I.2: Doniach phase diagram, Temperature, T, vs. $JN(E_F)$. AFM-antiferromagnetic ordering, FL-Fermi Liquid, T_N-Néel temperature, T_{Kondo}-Kondo temperature, T_{RKKY}-characteristic RKKY interactive temperature, J-intra-atomic exchange interaction, $N(E_F)$ density of state at the Fermi level.

Fermi liquid behavior was originally predicted by Doniach in the region above the suppression of magnetic order shown in the diagram. More recently, the Doniach diagram might include a non-Fermi liquid (NFL) region in the vicinity of a QCP which is related to the suppression of magnetic order to zero temperature as depicted in Figure I.2. A number of experiments on compounds, such as $CePd_2Si_2$, [28, 29] exhibit this non-Fermi liquid behavior near a QCP. Similar phase diagrams and physical properties are achieved in other systems through tuning the control parameters, such as composition, pressure, and magnetic field.

A QCP, which can be defined as a point where the temperature of a phase transition of a system is zero, is the result of the competition between the Kondo effect and the RKKY interaction. RKKY interaction is dominant for small $JN(E_F)$ and potentially induces magnetic ordering, whereas increasing $JN(E_F)$ leads to the screening of the magnetic moments as the result of the Kondo effect. [25] Due to the competition between the Kondo effect and the RKKY interaction, the transition temperature of a system will be zero at a certain $JN(E_F)$, $[JN(E_F)]_c$. When the transition temperature is close to zero, the thermal fluctuation will be diminished and the quantum fluctuation becomes dominant.

There are several ways in which the QCP can influence the finite temperature behavior. In the case of $CeIn_3$, the QCP is buried by the emergence of an unconventional superconducting state and can be introduced by applying pressure. It is also widely believed that the high temperature superconductivity observed in the cuprate superconductors is the result of a QCP. Instead of relying on the conventional phonon pairing mechanism to explain unconventional systems, an alternative scenario is that the superconductivity is mediated by excitations which are related to the QCP, such as spin fluctuations. In addition to superconductivity, non-Fermi liquid behavior is often observed in the vicinity of a QCP. [30, 31, 32, 33, 34, 35, 36]

I.B.2 Non-Fermi liquid behavior

In recent years, an intense research effort has been focused on the investigation of intermetallic compounds which violate Fermi liquid theory. These experiments revealed materials that exhibit the so-called NFL behavior and are usually Ce, U, or Yb-based heavy fermion compounds in which the magnetic susceptibility, specific heat, and electrical resistivity are characterised by weak power law or logarithmic divergences at low temperatures. For example, $Y_{1-x}U_xPd_3$ system has been studied by Seaman et. al. [36] in 1991, who reported measurements of electrical resistivity, magnetic susceptibility, and specific heat and found that their electron-electron interactions are too strong to act as the Fermi liquid ground state at low temperature. The results of these measurements contradict Landau's Fermi liquid model and initiated an intense theoretical and experimental effort to understand NFL behaviour in d- and f-electron inter-metallic compounds. NFL behavior in f-electron systems can be characterized by weak power-law or logarithmic temperature dependences of the physical properties at low temperatures $T < T_0$ and can be summarised as follows:

$$\rho(T) \propto [1 - a(\frac{T}{T_0})^n] \ (n \sim 1 - 1.5), \tag{I.15}$$

$$\frac{C(T)}{T} \propto -\frac{1}{T_0} ln(\frac{T}{T_0}) or T^{-1+\lambda} \ (\lambda \sim 0.7 - 0.8), \tag{I.16}$$

$$\chi \propto [1 - \frac{T}{T_0}^{1/2}], -ln(\frac{T}{T_0}) or T^{-1+\lambda} \ (\lambda \sim 0.7 - 0.8). \tag{I.17}$$

In several of those systems, the scaling temperature T_0 can be identified with the Kondo temperature T_K. [1, 37] NFL behavior is often observed for a wide variety of f-electron compound, including $CeRhIn_5$, $CeIn_3$ and $CePd_2Si_2$ which exhibit the suppression of antiferromagnetic ordering by pressure. Another example of NFL behavior occurring near a QCP are the high-T_c cuprate superconductors

in which both an antiferromagnetic transition and a pseudogap are suppressed by electron or hole doping. [33] Although a number of models [33] have been proposed to explain the origin of NFL behavior, the underlying basis for these models revolve around one or some combination of three principal themes: a) single ion Kondo effects, b) disorder, and c) vicinity of a $T = 0$ K phase transition, quantum critical point.

Bibliography

[1] W. J. de Hass, J. H. de Boer, and G. J. van den Berg, Physica B **1**, 1115 (1934)

[2] G. J. V. den Berg and C. J. Gorter, Helvetica Physica Acta **41**, 1230 (1968)

[3] J. Kondo, Progress of Theoretical Physics **32**, 37 (1964)

[4] P. W. Anderson, Phys. Rev. **124**, 41 (1961)

[5] P. W. Anderson, J. Phys. C **3**, 2439 (1970)

[6] J. R. Schrieffer and P. A. Wolff, Phys. Rev. **149**, 491 (1966)

[7] K. G. Wilson, Rev. Mod. Phys. **47**, 773 (1975)

[8] G. R. Stewart, Rev. Mod. Phys. **56**, 755 (1984)

[9] L. D. Landau, Sov. Phys. JETP **3**, 920 (1957)

[10] L. D. Landau, Sov. Phys. JETP **5**, 101 (1957)

[11] L. D. Landau, Sov. Phys. JETP **8**, 70 (1957)

[12] A. J. Leggett, Rev. Mod. Phys. **47**, 331 (1975)

[13] E. S. R. Gopal, "Specific Heats at Low Temperatures," Plenum Press, New York (1966)

[14] K. Andres, J. E. Graebner, and H. R. Ott, Phys. Rev. Lett. **27**, 1779 (1975)

[15] L. Tailerfer and G. G. Lonzarich, Phys. Rev. Lett. **60**, 1570 (1988)

[16] N. D. Mathur, F. M. Grosche, S. R. Julian, I. R. Walker, D. M. Freye, R. K. W. Haselwimmer, and G. G. Lazarich, Nature (London) **394**, 39 (1998)

[17] I. R. Walker, F. M. Grosche, D. M. Freye, and G. G. Lonzarich, Physica C **282-287**, 303 (1997)

[18] D. Jaccard, K. Behnia, and J. Sierro, Phys. Lett. A **163**, 475 (1992)

[19] G. Bednorz and K. A. Müller, Rev. Mod. Phys. **60**, 585 (1988)

[20] K. Ishida, Y. Nakai, and H. Hosono, J. Phys. Soc. Jpn. **78**, 062001 (2009)

[21] F. Steglich, J. Aarts, C. D. Bredl, W. Lieke, D. Meschede, W. Franz, and H. Schâfer, Phys. Rev. Lett. **43**, 1892 (1979)

[22] Y. Onuki and Y. Kitaoka, J. Phys. Soc. Jpn. **76**, 051001 (2007)

[23] K. Kadowaki and S. B. Woods, Solid State Commum. **58**, 307 (1986)

[24] N. Tsujii, H. Kontani, and K. Yoshimura, Phys. Rev. Lett. **94**, 057201 (2005)

[25] S. Doniach, Physica B **91**, 231 (1977)

[26] C. M. Varma, Rev. Mod. Phys. **48**, 219 (1976)

[27] A. C. Hewson, *The Kondo Problem to Heavy Fermions*, Cambridge University Press, Cambridge, England (1993)

[28] N. D. Mathur, F. M. Grosche, S. R. Julian, I. R. Walker, D. M. Freye, R. K. W. Haselwimmer, and G. G. Lonzarich, Nature **394**, 39 (1998)

[29] F. M. Grosche, S. J. S. Lister, F. V. Carter, S. S. Saxena, R. K. W. Haselwimmer, N. D Mathur, S. R. Julian, and G. G. Lonzarich, Physica B, **239**, 62 (1997)

[30] M. B. Maple, M. C. deAndrade, J. Hermann, Y. Dalichaouch, D. A. Gajewski, C. L. Seaman, R. Chau, R. Movshovich, M. C. Aronson, and R. Osborn , J. Low Temp. Phys, **99**, 223 (1995)

[31] J. A. Hertz, Phys. Rev. B **14**, 1165 (1973)

[32] A. J. Millis, Phys. Rev. B **48**, 7183 (1993)

[33] G. R. Stewart, Rev. Mod. Phys. **73**, 797 (2001)

[34] J. L. Smith and Q. Si, Phys. Rev. B **61**, 5184 (2000)

[35] M. B. Maple, C. L. Seaman, D. A. Gajewski, Y. Dalichaouch, V. B. Barbetta, M. C. deAndrade, H. A. Mook, H. G. Lukefahr, O. O. Bernal, and D. E. MacLaughlin, J. Low Temp. Phys, **95**, 225 (1994)

[36] C. L. Seaman, M. B. Maple, B. W. Lee, S. Ghamaty, M. S. Torikachvili, J.-S. Kang, L. Z. Liu, J. W. Allen, and D. L. Cox, Phys. Rev. Lett. **67**, 2882 (1991)

[37] M. B. Maple and J. Wosnitza, *The physics of Conventional and Unconventional Superconductors*, Springer Verlag, Berlin (2003)

Chapter II

Experimental Details

II.A Sample Synthesis

II.A.1 Flux Growth

The flux method [1] is a useful tool for making single crystals. Since the metallic flux can induce a lower melting point, the flux method is well suited for some elements with high melting points. The quality of single crystals are better than polycrystals due to the fact that single crystals have less impurities and thermal strain. Single crystals are preferred also because single crystals are able to provide information of anisotropy. In addition, crystals can be grown in a clean environment since the metallic molten flux collects potential impurities and excluding them from the single crystals. Despite of the many advantages in using the flux growth method, it is not always a suitable method for single crystal synthesis. Some flux type can also participate in crystal growth and forming second phases or impurities. However, this problem can be alleviated by adjusting the ratio of starting materials as well as cooling curves while cooling the melted material though this procedure can be complicated. Furthermore, crystals are sometimes grown around a pocket of flux. This effect can be minimized by choosing the proper etching liquid to get a clean single crystal.

Single crystals of $R_2T_{12}Pn_7$ (R = rare earth, T = transition metal, Pn =

P, As) were grown in a molten Sn flux with the ratio R:T:Pn:Sn = 1:4:2:30 using elements with purities of 99.9% or better. The starting materials were sealed under an Ar-atmosphere of $\sim$ 250 Torr in a quartz tube, heated to 1150°C, dwelled for 24 hours, and were allowed to cool slowly to 600°C over 168 hours. Excess Sn flux was spun off using a centrifuge and residual Sn on the surface of the crystals was etched away with dilute HCl. In this way, needle-shaped single crystals were obtained with typical dimensions of $4 \times 0.1 \times 0.1$ mm^3 as shown in Fig. II.1.

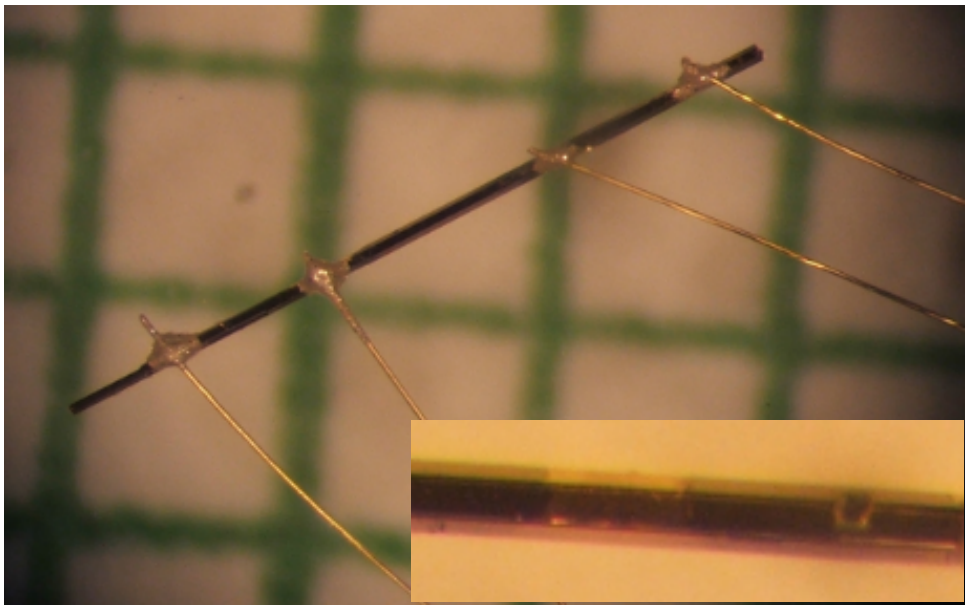

Figure II.1: A single crystal of $Yb_2Ni_{12}P_7$ grown using a Sn flux method. with four electric contact for resistivity measurement. Inset shows zoom in picture of $Yb_2Ni_{12}P_7$ to describe hexagonal structure.

The $Ce_{1-x}Yb_xRhIn_5$ alloys and $Ce_{1-x}Sm_xCoIn_5$ alloys can be grown by the In- self flux method using an appropriated temperature profile. The general procedure of making single crystals using the flux method is the following: stoichiometric amounts of elements with flux are put in a crucible made of Al_2O_3; then the crucible is put into a quartz tube with some quartz wool and sealed off under vacuum. It is known that Al_2O_3 has a larger thermal expansion coefficient than quartz.

II.B Characterization

II.B.1 Energy Dispersive X-ray spectroscopy (EDS)

Exact chemical concentration for the sample is essential for sample synthesis. Energy Dispersive X-ray (EDS) is a useful tool for investigating each element concentration in the grown material. It provides qualitative and quantitative identification of elements in samples without damage to the sample. When multiple elements are included in the samples, the minor element signal is too weak to determine the exact amount of the ratio yielding less than reliable results. Nevertheless, it is still one of the most effective way to understand chemical concentration.

II.B.2 Powder X-ray Diffraction

X-ray diffraction is a tool used for identifying the atomic and molecular structure of a crystal. An X-rays beam is incident to the sample and the lattice of atoms causes the beam to diffract into many specific directions. It provides some useful information about the crystal structure, such as a three dimensional picture of the density of electrons, chemical bonding length, and their disorder, by measuring the angle and intensities of these diffracted beams. Powder X-ray Diffraction measurements require proper preparations of the X-ray slide. An X-ray side is made by mixing a few milligrams of powderzied sample with petrolatum jelly to form an opaque paste and then spread out broadly over the slide with even

thickness. Alternatively, it is possible to double-side affix tape to the glass slide, and then cover the tape with powderized crystal. The X-ray powder diffraction data, in this thesis, were made at room temperature using a Bruker D8 Discover diffractometer. Monochromatic X-ray were generated by a rotating copper anode which produces Cu-K_α X-ray radiation; this X-ray radiation passes through all the possible orientations of the powdered single crystals during which the detector and sample mount span a part of the Ewald sphere. When the diffraction pattern satisfies Bragg's law, $n\lambda = 2dsin\theta$, for any electron plane, one can extract a value of 2-θ and the intensity as a result. These results were analysed by the Rietvelt method and the program suite GSAS was useful in order to calculate the lattice constants.[2]

II.B.3 Electrical Resistivity

Electrical resistivity, ρ, was measured as a function of temperature T between 300 K and 1.2 K in a ^{4}He cryostat upon applying current, typically 0.1 mA. The data below 1.2 K, down to 0.05 K, were made of using a ^{3}He-^{4}He dilution refrigerator. In order to make electrical contact to the samples, gold or platinum wire was attached to the samples with silver epoxy or silver paste for a traditional four-wire measurement. The resistance was measured with an AC resistance bridge. The resistance data are converted to resistivity, ρ, using the geometrical factor ($\rho = RA/L$, where A is the cross-sectional area and L is the distance between the voltage leads).

II.B.4 Magnetization

The magnetization measurements were made with a Quantum Design SQUID magnetometer. Magnetic susceptibility as a function of temperature was performed from 400 K to 1.8 K and magnetization as a function of field was obtained up to 7 T. A straw was used for holing each sample in the sample space. The straw is a diamagnetic material which gives a diamagnetic signal but usually

negligibly small compared with the sample's signal. In the case of poly-crystalline samples, a gel capsule with a hole is put into the straw; the sample is included in the gel capsule. Tape was used for making single crystal samples; one or sometimes a mosaic of single crystals were put on the tape and inserted into the straw. In the case of the $Ce_{1-x}Yb_xRhIn_5$ and $Ce_{1-x}Sm_xCoIn_5$ systems, which have a tetragonal structure, and the $R_2T_{12}Pn_7$ system which has a hexagonal structure, there are a differences between the in-plane measurement (ab-plane $\parallel \mu_0 H$) and the out of plane measurement (c-plane $\parallel \mu_0 H$).

II.B.5 Specific Heat

The specific heat data were obtained with a PPMS from Quantum Design which can apply magnetic field up to 9T. The heat capacity is measured by using a thermal relaxation technique at constant pressure. A known amount of heat is applied to a sample and then temperature change is measured when the heat is released from the sample. The heat capacity puck consists of several parts, including a thermometer, a heater, a platform and small wires which connect the puck frame to the platform. A vacuum ensures that the thermal conductance between the sample platform and thermal bath (puck frame) is dominated by the conductance of the wires. This allows both the platform and sample to achieve sufficient thermal equilibrium during the measurement.

Bibliography

[1] Z. Fisk and J. P. Remeika, "Handbook on the Physics and Chemistry of Rare Earths," Vol 12, edited by K. A. Gschneidner, Jr. and L. Eyring (Elsevier Science Publishing Company, Inc., New York, New York, (1989) pp. 53-70.

[2] A. C. Larson, and R. B. Von Dreele, "General Structure Analysis System (GSAS)," Los Alamos National Laboratory Report LAUR 86-748 (2000).

[3] Lake Shore Cryotronics, Inc. Not dated. LakeShore 7500/9500 Series Hall Series Hall System User's Manual. Westerville, OH. www.lakeshore.com

[4] J. S. Hwang, K. J. Lin, and C. Tien, Rev. Sci. Instrum. **68** 1 (1997)

[5] R. Bachmann, F. J. DiSalvo, T. H. Geballe, R. L. Greene, R. E. Howard, C. N. King, H. C. Kirsch, K. N. Lee, R. E. Schwall, H. U. Thomas, and R. B. Zubeck, Rev. Sci. Instrum. **43** 2 (1972)

Chapter III

Crossover between Fermi liquid and non-Fermi liquid behavior in the non-centrosymmetric compound $Yb_2Ni_{12}P_7$

III.A Introduction

For more than four decades, rare-earth intermetallic compounds containing Ce, Pr, Sm, Eu, Tm, Yb, and U have received considerable attention due to their unusual properties, which are generally related to, or consequences of, an f-electron valence instability. The low-temperature properties are associated with hybridization of the localized f-electron and conduction electron states [1] as described by the Friedel-Anderson model. [2] There are many models for this subtle electronic state that are neither localized nor truly itinerant, but a common feature is the existence of a characteristic energy scale k_BT^* that delineates high-temperature magnetic (Curie-Weiss law) behavior from low-temperature nonmagnetic (Pauli-like) behavior of the f-electrons. When the strength of the hybridization is especially large, the f-electron shell may fluctuate between two $4f$ electron

configurations $4f^n$ and $4f^{n-1}$, where n is an integer. The unit-cell volume of a system with rare-earth ions in such a valence-fluctuating state [3] is intermediate between those of the integral-valence states. This results in a deviation of the unit cell volume from the corresponding volumes of trivalent lanthanide ions associated with the lanthanide contraction. Furthermore, the electrical resistivity, $\rho(T)$, of valence fluctuating systems typically shows a quadratic temperature dependence at low temperature and a shoulder in $\rho(T)$ at high temperatures. [3, 4, 5, 6]

Yb has an ambivalent character in several metallic compounds, (*i.e.*, the state of Yb cannot be described as purely Yb^{3+} ($4f^{13}$) nor Yb^{2+}($4f^{14}$)). [7] In particular, Yb compounds attract a great deal of interest because the trivalent Yb ion can be thought of as the $4f$ hole counterpart of the Ce^{3+} ion, which has one electron in its $4f$ shell. As in the case of Ce compounds, [8] the Yb-based intermetallics exhibit a rich diversity of physical properties that are not completely understood. [9]

The low-temperature ground states, and the quantum phase transitions between them, of f-electron compounds are frequently quiet interesting. Quantum phase transitions, or quantum critical points (QCPs), and their effect on the physical properties at finite temperatures have attracted considerable attention since the 1990's. [10] In metallic systems, strong deviations from Fermi-liquid (FL) behavior in the neighborhood of a QCP have been observed and are manifested by pronounced non-Fermi-liquid (NFL) behavior. For example, C_e/T, the electronic contribution to specific heat, C, divided by temperature, T, shows characteristic -ln$T$ behavior at low temperatures instead of being temperature independent. In such systems, the electrical resistivity, ρ, is proportional to T^n with an exponent of $n = 1$ - 1.5 instead of the FL result where $n = 2$. [11] While a large number of Ce- and U-based heavy fermion (HF) systems have been discovered and thoroughly investigated [10] there are few Yb-based HF systems in which the low-temperature ground states have been studied. Only a few of them order magnetically and are located near a magnetic QCP, and there seem to be no examples of an Yb-based

system that is close to a QCP but does not order magnetically. These factors motivated us to look for Yb-based systems situated close to the boundary of NFL and FL regions.

Compounds with the non-centrosymmetric $Zr_2Fe_{12}P_7$ - type hexagonal crystal structure (space group $P\overline{6}$) with the general formula $Ln_2T_{12}Pn_7$ (where Ln = lanthanide, T = transition metal, and Pn = P or As) have been studied for the past 50 years. [12, 13, 14, 15] Most of these studies have involved efforts to synthesize the materials and study their crystal structure, so that their physical properties are still mostly unreported. Recently, some interesting correlated electron behavior has been reported for several compounds in this structure, such as heavy fermion behaviour and ferromagnetism in $Sm_2Fe_{12}P_7$, [16] and local moment antiferromagnetism in $U_2Fe_{12}P_7$. [17] The temperature-magnetic field phase diagram in $Yb_2Fe_{12}P_7$, which exhibits a crossover from one non-Fermi liquid (NFL) regime at low magnetic field to a distinct NFL regime at higher field, is particularly notable. [18] This unconventional behavior in the $Yb_2Fe_{12}P_7$ compound may stem from spin-chain physics.

The physical properties of $Yb_2Ni_{12}P_7$ were first studied by Cho *et al.* using a polycrystalline sample which included about 8% of Yb_2O_3 impurities. [19] The main result of that study was to identify an intermediate valence (IV) state for Yb in $Yb_2Ni_{12}P_7$, where the valence of Yb was estimated to be about 2.79 based on analysis of magnetic susceptibility data. [19] Recently, electrical resistivity, ρ, specific heat, C, and magnetic susceptibility, χ, measurements were reported for single crystals of $Yb_2Ni_{12}P_7$. [20] These results were largely consistent with those from the polycrystalline sample, and further suggested that $Yb_2Ni_{12}P_7$ exhibits correlated electron behavior with a probable IV Yb state. [20] A study of $Yb_2Ni_{12}P_7$ under applied pressure was also recently conducted by Nakano *et al.*; their results suggest the existence of a QCP and demonstrate that T_{FL} decreases and ρ_0 and the coefficient A increase with increasing applied pressure.

Though there are studies that suggest $Yb_2Ni_{12}P_7$ may be near a QCP,

there are no comprehensive studies of this compound that have been made to very low temperature; such a study is necessary to elucidate details of the possible QCP. Motivated by these previous studies, and in order to study the low-temperature behavior of $Yb_2Ni_{12}P_7$ further, we performed measurements of ρ, χ, and C on high-quality single crystalline samples at temperatures down to 100 mK for $\rho(T)$, and 2 K for $\chi(T)$ and $C(T)$. We also performed measurements of the thermoelectric power, $S(T)$. In agreement with previous reports, an IV Yb state is clearly observed in the physical properties and the valence is estimated to be $\sim$ 2.76 based on analysis of the $\chi(T)$ data. A robust quadratic temperature dependence for ρ (*i.e.*, $\rho \sim T^n$ where $n = 2$) is observed below $\sim$4 K, which indicates that $Yb_2Ni_{12}P_7$ has a FL ground state. The electronic contribution to the specific heat exhibits $C_e(T)/T \sim -\ln(T)$ behavior for 5 K $< T <$ 15 K, which is consistent with NFL behavior. Below $\sim$5 K, the upturn in $C_e(T)/T$ begins to saturate, suggesting that the system crosses over into a FL ground state. The possibility of a crossover between FL and NFL states near $\sim$5 K is strengthened by analysis of the temperature dependence of the power-law exponent, $n(T)$, of the electrical resistivity, which becomes sub-quadratic at temperatures above 4 K. A crossover between FL and NFL behavior is consistent with $Yb_2Ni_{12}P_7$ being in proximity to an unidentified QCP.

III.B Experimental details

Single-crystalline samples of $Yb_2Ni_{12}P_7$ and $La_2Ni_{12}P_7$ were prepared from elemental Yb (small dendritic pieces) or La (small chunks), Ni (small dendritic pieces), and P (small lumps). The crystals were grown by reacting elements with purities of 99.9% (or better) with the initial atomic ratios Yb:Ni:P:Sn = 1:4:2:30 in a molten Sn flux. The starting materials were sealed under vacuum in a quartz tube, heated to 1150 °C, dwelled for 24 hours, and cooled slowly to 600 °C over a span of 168 hours. The Sn flux was spun off using a centrifuge. Any residual Sn

on the surface of the crystals was etched away in dilute HCl. Needle-shaped single crystals were obtained with typical dimensions of $4 \times 0.5 \times 0.5$ mm^3.

Polycrystalline samples of $Yb_2Ni_{12}P_7$ for thermoelectric power measurements were prepared from elemental Yb (small dendrite pieces), Co (powder), and P (small lumps). The starting materials were sealed under vacuum in quartz tubes, slowly heated to 1000 °C, and held at this temperature for 3 days. After the initial reaction, the sample was ground into a powder, pressed into a pellet, and fired at 1135 °C for 3 days. Finally, the sample was re-ground again and fired at 1135°C for 3 days.

X-ray diffraction measurements were performed on powdered single crystals using a Bruker D8 Discoverer x-ray diffractometer. The resulting powder diffraction patterns were refined by means of Rietveld analysis [21] implemented in the program suite GSAS. [22] The stoichiometry was further verified using energy dispersive x-ray spectroscopy (EDX) measurements with a FEI Quanta 600 and an INCA EDX detector from Oxford instruments. Isothermal magnetization $M(H)$ and magnetic susceptibility $\chi(T) = M(T)/H$ were measured for T = 2-300 K in magnetic fields H up to 7 T using a Quantum Design (QD) Magnetic Property Measurement System. The magnetic field, H, was applied both parallel and perpendicular to the crystallographic c axis. We measured specific heat between 2 and 50 K in a QD Physical Property Measurement System DynaCool using a standard thermal relaxation technique. Electrical resistivity measurements were carried out in a four-wire configuration in a pumped ^{4}He dewar to 1.1 K and in an Oxford Kelvinox dilution refrigerator between T = 100 mK and 20 K and in magnetic fields of $H = 0$ and 9 T.

Measurements of the thermoelectric power were performed by applying a static temperature gradient of $\Delta T/T = 2\%$, where ΔT was measured using two Cernox 1050 thermometers and a Lakeshore 340 Temperature Controller. Copper leads were attached to the sample using silver epoxy in a two-wire configuration. The thermoelectric voltage generated by the sample was measured using a Keithley

2182 Nanovoltmeter and was corrected for a background contribution arising from a slight compositional asymmetry of the alloys used in the twisted pairs of wires running from the sample to the external electronics at room temperature.

III.C Result

III.C.1 Crystal structure

The unit cell volume of $Yb_2Ni_{12}P_7$ was determined from powder x-ray diffraction measurements at room temperature to be 259.4 Å^3. In Figure 1, the unit cell volume of $Ln_2Ni_{12}P_7$ is plotted vs. lanthanide ion Ln where open circles are taken from Ref. [14]. Starting with La, one observes the typical reduction of the volume due to the contraction of the ionic radii of the lanthanides with increasing atomic number. However, the cases of Ln = Ce and Eu exhibit behavior which reflects their tendency toward assuming tetravalent and divalent states, respectively. Our result for $Yb_2Ni_{12}P_7$ is in good agreement with other reported values within experimental uncertainty. [19, 23] According to the trend of the unit cell volumes, the Yb ion in $Yb_2Ni_{12}P_7$ appears to be nearly trivalent at room temperature.

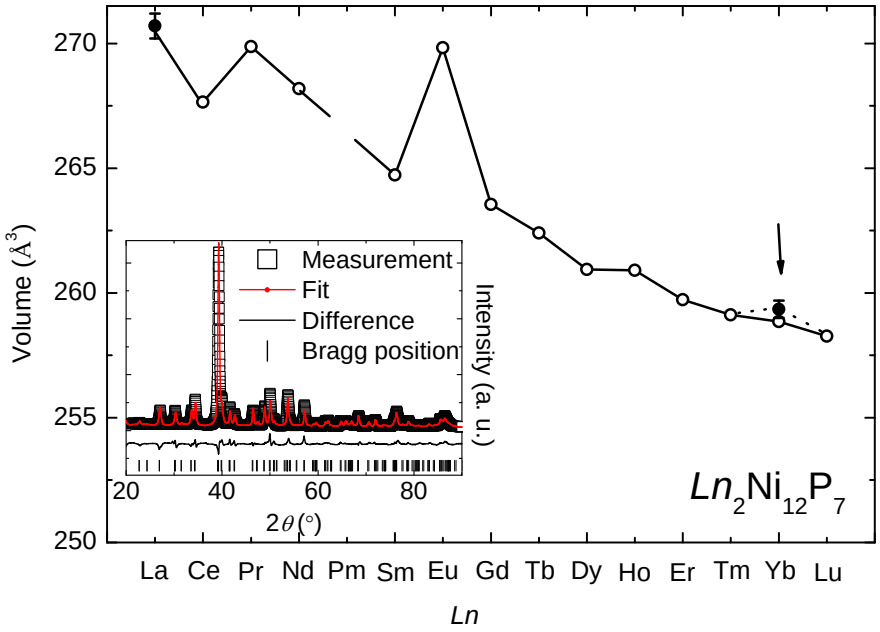

Figure III.1: Unit cell volume vs. *Ln* element for $Ln_2Ni_{12}P_7$ compounds; open circles are from Ref. [14] and filled circles are from this work. Inset: X-ray diffraction pattern of $Yb_2Ni_{12}P_7$ at room temperature (open squares) and fit from Rietveld refinement (red line).

III.C.2 Magnetic susceptibility

Magnetic susceptibility, $\chi(T)$, measurements were performed for $Yb_2Ni_{12}P_7$ in a magnetic field of $H = 0.5$ T with the field applied parallel and perpendicular to the c axis. The data are shown in Figure 2. Curie-Weiss (CW) behavior was observed at temperatures between 200 and 300 K with CW temperatures θ_{CW} = -34 K and -52 K for $H \perp c$ and $H \parallel c$, respectively (see lines in Figure 2(b)). Effective magnetic moments, $\mu_{eff} = 4.1\ \mu_B$ and 3.4 μ_B, for $H \perp c$ and $H \parallel c$, respectively, were also obtained from our analysis. These two values are lower than the previously reported value of $\mu_{eff} = 5.1\mu_B$, which was obtained from a fit over the temperature range 50 K to 300 K; however, we note that the orientation of H with respect to the c axis was not specified in that report. [20] These effective magnetic moments are intermediate between the Hund's rule values for Yb^{3+} ($\mu = 4.5\mu_B$ for the free ion) and nonmagnetic Yb^{2+} ($\mu = 0$) configurations. This result suggests that the Yb ions in this compound assume an intermediate valence.

Below 100 K, $\chi(T)$ saturates and exhibits temperature-independent Pauli paramagnetic behavior with $\chi_0 = 0.014$ and 0.009 cm^3/mol-Yb for $H \perp c$ and $H \parallel c$, respectively. These values are comparable to a previously reported value of χ_0 = 0.012 cm^3/mol-Yb and suggest a moderately-enhanced effective mass for the conduction electrons. [20] Measurements of M vs. H are displayed in Fig. 2(c), which were performed at 2 K, 20 K, and 100 K. These temperatures are at or lower than the crossover from Curie-Weiss to Pauli paramagnetic behavior, and the M vs. H data are consistent with that interpretation. This type of behavior is common for mixed-valent Ce- and Yb-based compounds as seen, for instance, in CeRhIn and YbCuAl. [24, 25] The sharp rise of $\chi(T)$ below 20 K is probably due to the presence of Yb_2O_3 as a secondary impurity phase in the samples; though it could also be consistant with NFL behaviour. [19, 26, 27, 28]

The behavior of $\chi(T)$ can be interpreted within the framework of the inter-configuration fluctuation (ICF) model. [29] In the ICF model, which was applied to $Yb_2Ni_{12}P_7$ in Ref. [19], expected values for measured physical quantities

(*e.g.*, Yb valence, Mössbauer isomer shift, magnetic susceptibility, etc.) are calculated by averaging over the occupied $4f^n$ and $4f^{n-1}$ multiplet states. The energy difference between the ground state and excited-state configurations is defined as E_{exc}. The $\chi(T)$ data, and the fit to $\chi(T)$ using the ICF model, are plotted as a function of temperature for both orientations ($H \parallel c$ and $H \perp c$) in Fig. 2(a). The ground state of Yb (Yb^{2+}, $4f^{14}$) has total angular momentum $J = 0$ and effective magnetic moment $\mu_{eff}^{2+} = 0$, while the excited state (Yb^{3+}, $4f^{13}$) has $J = 7/2$ and $\mu_{eff}^{3+} = 4.54\ \mu_B$. The temperature dependence of the susceptibility of the mixed-valence Yb ions in the ICF model is given by [30]

$$\chi_{ICF}(T) = (1 - n_{imp})\frac{N(\mu_{\rm eff}^{3+})^2 P(T)}{3k_B(T + T_{vf})} + n_{imp}\frac{C}{T} + \chi_0, \qquad \text{(III.1)}$$

where

$$P(T) = \frac{8}{8 + \exp[E_{exc}/k_B(T + T_{vf})]}. \qquad \text{(III.2)}$$

$P(T)$ is the fractional occupation probability for the $4f^{13}$ contribution, T_{vf} is the valence-fluctuation temperature, χ_0 is a temperature-independent contribution to the magnetic susceptibility (but is not the enhanced Pauli susceptibility), and N is the number of Yb ions. The Curie term in Eq. (1), weighted by a scale factor n_{imp}, is introduced to account for the upturn in $\chi(T)$ at low temperatures that is likely caused by paramagnetic impurities containing Yb^{3+} ions. A least squares-fitting procedure was used to fit Eq. (1) to the experimentally observed $\chi(T)$ data plotted in Figure 2(a). The best fits are shown as solid lines in Fig. 2(a) with the following parameters: $E_{exc} = 325$ K, $T_{vf} = 140$ K, $n_{imp} = 0.016$, and $\chi_0 = 5.46\times\ 10^{-3}$ cm^3/mol for $H \perp c$, and $E_{exc} = 453$ K, $T_{vf} = 198$ K, $n_{imp} = 0.013$, and $\chi_0 = 5.27\times\ 10^{-3}$cm^3/mol for $H \parallel c$. The valence of the Yb ion in $Yb_2Ni_{12}P_7$ is calculated at room temperature using Eq. (2) to be 2.79 and 2.76 for $H \perp c$ and $H \parallel c$, respectively. These parameters agree reasonably well with values of $E_{exc} = 278$ K, $T_{vf} = 68$ K, and a valence of 2.79 which were obtained in a previous ICF model analysis of $\chi(T)$ data for a polycrystalline sample of $Yb_2Ni_{12}P_7$. [19] The

values of T_{vf} are also comparable to values reported for other Yb-based mixed-valence compounds, such as $YbAl_3$. [31] The best-fit E_{exc} values are comparable to those of certain Yb compounds, such as YbB_4, [30] but are about a factor of two larger than the value for the compound $YbAl_3$. [31]

From the analysis of $\chi(T)$ data using the ICF model, we estimate an impurity ratio of $\sim 1\%$. This value is comparable to the impurity concentration that is estimated from the entropy associated with AFM order in Yb_2O_3 in $C(T)/T$ as discussed below. Since the contribution to $\chi(T)$ from the impurity phase can be large at low temperature, even though the impurity concentration is low, the upturn probably originates from the presence of Yb_2O_3 in the sample. Another possible explanation for the upturn in $\chi(T)$ between 2-10 K is that it could be a manifestation of NFL behavior; this explanation would suggest that the upturn is an intrinsic property of $Yb_2Ni_{12}P_7$ rather than being extrinsic (i.e., from impurities). We find that $\chi_{ab}(T)$ can be described by a weak power law or with a logarithmic temperature dependence of the form $\chi_{ab}(T) = a - b\ln(T - c)$ where best fit values were found to be $a = 0.016$ cm^3/mol, $b = 7.82\times\ 10^{-4}$ cm^3/mol, and $c = 1.94$ K. Such a temperature dependence for the magnetic susceptibility is a significant departure from FL behaviour; however, we cannot ignore the compelling evidence for a small amount of magnetic impurities in our samples. While these impurities likely play a significant role in producing the low-temperature upturn, we cannot rule out the possibility that it arises from a combination of NFL behaviour (intrinsic) and Curie-law behaviour (extrinsic).

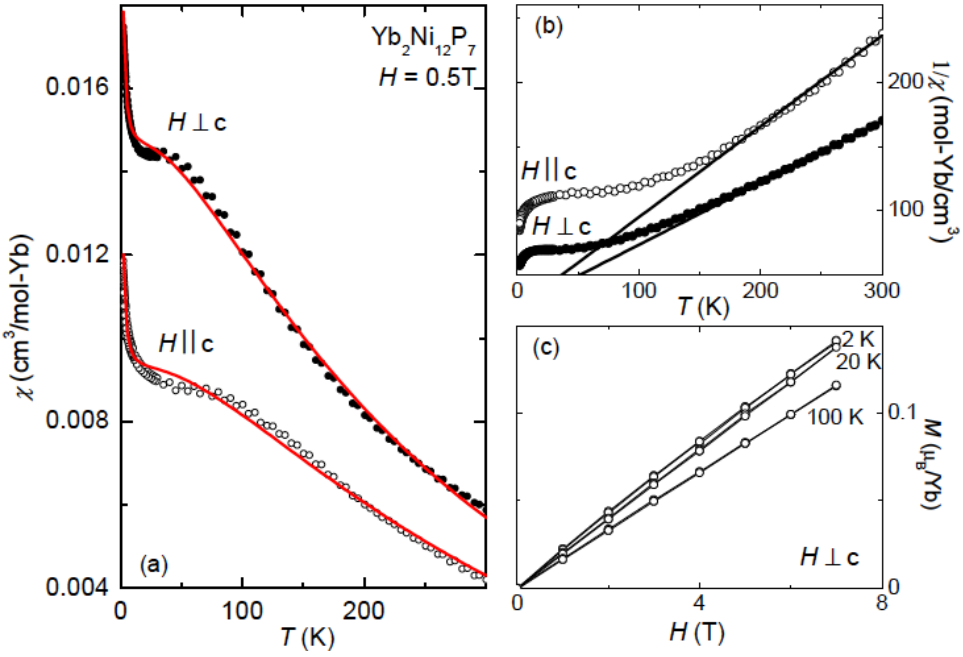

Figure III.2: (a) Magnetic susceptibility, $\chi = M/H$, vs. temperature, T, for magnetic field of $H = 0.5$ T applied parallel ($\|$) and perpendicular ($\perp$) to the c axis. The $\chi(T)$ data were fitted with Eq. (1) and the best-fit results are represented by the solid lines. (b) $\chi^{-1} = H/M$, vs. T for $H \parallel c$ and $H \perp c$. The solid lines represent Curie-Weiss fits to the data. (c) M vs. H for $H \perp c$ at $T = 2$ K, 20 K, and 100 K.

III.C.3 Electrical resistivity

The electrical resistivity, $\rho(T)$, of $Yb_2Ni_{12}P_7$, measured in magnetic fields $H = 0$ T and 9 T, is shown in Figure 3 between 100 mK and 300 K. $\rho(T)$ decreases linearly between 180 K and 300 K with decreasing temperature. At lower temperatures, there is a gentle roll off with decreasing temperature, which could be related to splitting of the $J = 7/2$ multiplet of Yb by the crystalline electric field. The curvature in $\rho(T)$ has also been previously attributed to typical behavior for IV Yb-based compounds with low values of E_{exc} and T_{vf}. [19] To characterize $\rho(T, H)$ at low temperature, the data were fitted with a power law,

$$\rho(T) = \rho_0 + AT^n, \tag{III.3}$$

where the best fit was determined from a plot of $\ln(\rho - \rho_0)$ versus $\ln(T)$. We note that A is an important quantity in FL systems (*i.e.*, for $n = 2$), but in other cases where $n \neq 2$, A would just be interpreted as a coefficient. The value of ρ_0 was selected to maximize the linear region of the fit extending from low T. Such fits always resulted in $n = 2$ as is emphasized in the plot of ρ vs. T^2 shown in the inset of Fig. 3, where it is apparent that the electrical resistivity follows a FL-like T^2 temperature dependence at low T. [4, 32] A quadratic temperature dependence for ρ at low T is observed in many other Yb- and Ce-based mixed-valence and heavy-fermion compounds (*e.g.*, $CeInPt_4$ and $YbAgCu_4$). [33, 34] From these fits, we find that $\rho_0 \sim 15.8$ $\mu\Omega$ cm and 16.3 $\mu\Omega$ cm and that $A = 0.0458$ $\mu\Omega$ cm/K^2 and 0.0462 $\mu\Omega$ cm/K^2 for $H = 0$ T and 9 T, respectively. These results suggest that applied magnetic fields less than $H = 9$ T have a negligible effect on the FL ground state.

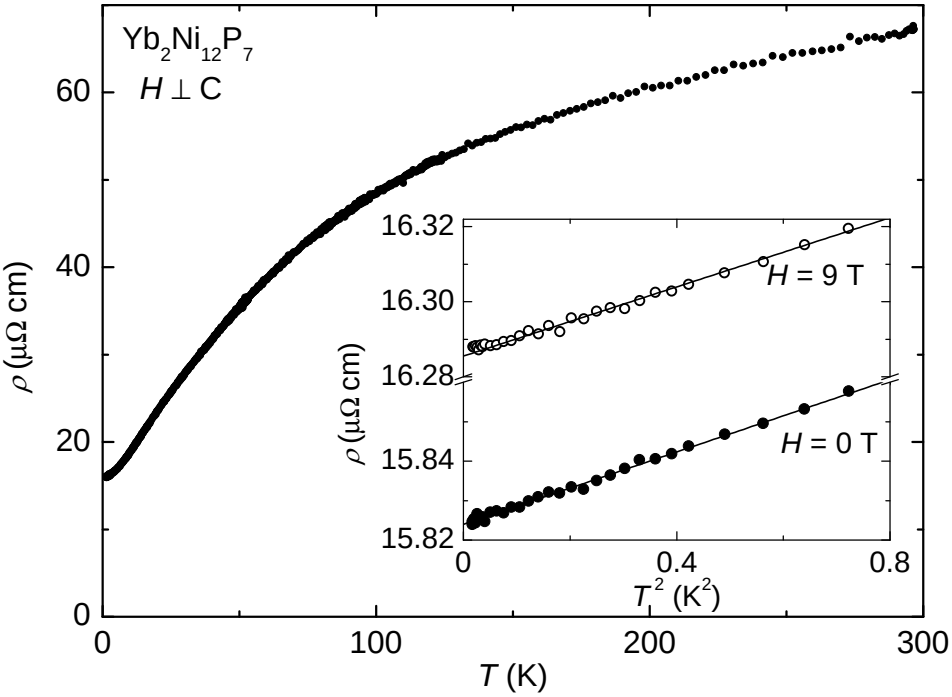

Figure III.3: Electrical resistivity, ρ, vs. temperature, T, for $Yb_2Ni_{12}P_7$. The inset displays ρ vs. T^2 data for magnetic fields of $H = 0$ and 9 T applied parallel to the c axis. The solid lines are fits to the data using Eq. (3).

III.C.4 Specific heat

The specific heat of $Yb_2Ni_{12}P_7$ is plotted in Figure 4(a) as C/T vs. T as measured in $H = 0$ and 9 T applied magnetic fields. There appears to be very little difference between the data measured in $H = 0$ T and 9 T magnetic fields. Figure 4(b) reveals moderately-large electronic specific heat coefficients $\gamma \sim 137$ mJ/mol-K^2 and 143 mJ/mol-K^2 for $H = 0$ T and 9 T, respectively. These values were obtained from a fit to the data in the temperature range $15 \leq T \leq 25$ K of the expression $C(T) = \gamma T + \beta T^3$ (see lines in Figure 4(b)). The cubic term characterizes the phonon contribution from the Debye model. We estimate the Debye temperature $\Theta_D = (12\pi 4 N_i R/5\beta)^{1/3}$ to be 329 K and 335 K for $H = 0$ T and 9 T, respectively; here, $N_i = 21$ is the number of ions per formula unit and R is the universal gas constant. If we estimate γ by extrapolating C/T to zero temperature, denoted herein as γ_0, we obtain $\gamma_0 \sim 192$ mJ/Yb mol-K^2 and 196 mJ/Yb mol-K^2 for $H = 0$ T and 9 T, respectively. These values for γ_0 are comparable to other values which were reported previously. [19, 20] A small peak near $T_N = 2.3$ K is observed in Figure 4(a) (data measured in $H = 0$ T) which is due to antiferromagnetic (AFM) ordering of Yb_2O_3 impurities. These impurities are probably present on the surface of the single crystals. The presence of Yb_2O_3 impurities was also reported in other studies of $Yb_2Ni_{12}P_7$. [19] The entropy associated with this anomaly, presumably proportional to the concentration of the impurity phase that produces it, is about 1.2% of $R\ln 2$. Figure 4(c) shows the electronic contribution to specific heat, C_e/T, obtained by subtracting the lattice contribution from C/T. In the temperature range from $T = 2$ K to 17 K, C_e/T appears to increase with decreasing temperature. This same behavior was reported in Ref. [15] despite the presence of a larger Yb_2O_3 contribution (characterized by feature at $T_N \sim 2.3$ K) than we observed in our single crystal samples. In Figure 4(d), C_e/T is plotted on a semi-log scale to emphasize the logarithmic character of $C_e/T \sim -\ln T$ down to $\sim$5 K. This behavior is consistent with typical NFL behavior observed in many other systems. [35, 36, 37, 39, 38] Below 5 K, the logarithmic divergence in C_e/T begins

to saturate which might indicate a crossover into a FL state at low temperature. A similar situation is observed in the compound $YbCo_2Zn_{20}$ at $T \sim 0.2$ K. [40]

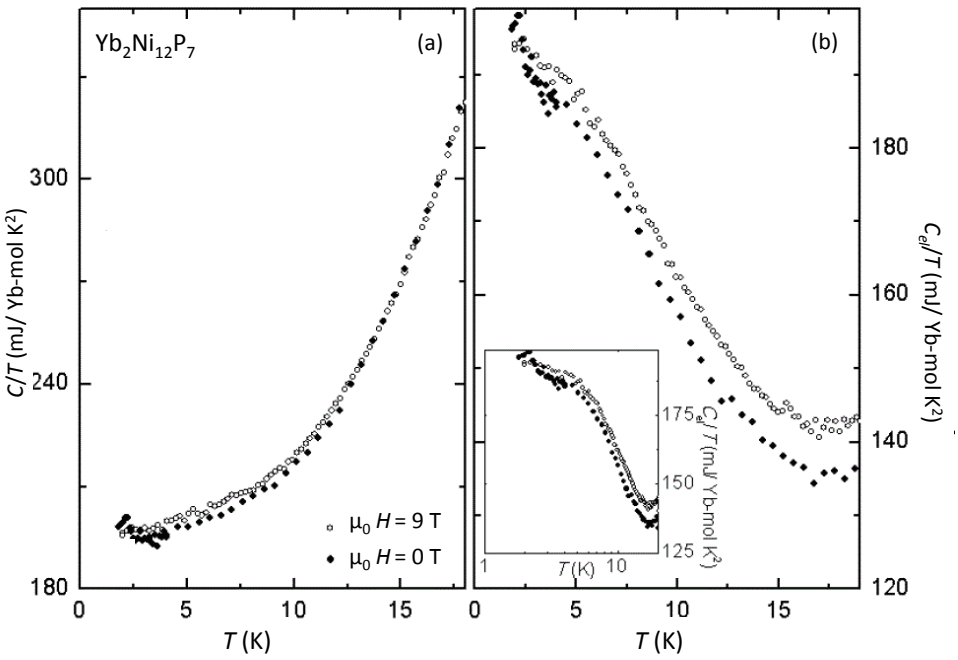

Figure III.4: (a) Specific heat, C, divided by temperature, for $Yb_2Ni_{12}P_7$, measured in applied magnetic fields $H = 0$ T and 9 T. Filled and open circles represent $H = 0$ T and $H = 9$ T data, respectively. (b) C/T vs. T^2 for $Yb_2Ni_{12}P_7$. Solid lines represent fits of $C/T = \gamma + \beta T^2$ to a linear region of data to extract the Sommerfeld coefficient, γ, and coefficient, β, of the lattice contribution. (c) Electronic contribution to specific heat, C_e/T, obtained by subtracting the phonon contribution. (d) C_e/T plotted on a logarithmic temperature scale. The upturn in C_e/T has a logarithmic character down to ~ 4 K, below which, it tends to saturate with decreasing T.

III.C.5 Thermoelectric power

Figure 5(a) displays the thermoelectric power, $S(T)$, for $Yb_2Ni_{12}P_7$ between 2 K and 300 K. The sign of $S(T)$ is negative over the entire measured temperature range. Large, negative values for $S(T)$ are commonly observed in other Yb-based Kondo lattice systems. [41, 42] The deep minimum near ∼40 K could be related to spin fluctuations [41, 43] like in $YbCu_2Si_2$. However, a single minimum is also predicted for a generic Yb-based Kondo lattice system in which hybridization between localized and itinerant electron states is strong enough to facilitate an intermediate Yb valence. [44] This latter scenario is consistent with the evidence for an intermediate Yb valence in $Yb_2Ni_{12}P_7$ from our magnetic susceptibility data.

Figure 5(b) displays $S(T)$ data divided by T, -$S(T)/T$, plotted on a logarithmic T scale. The -$S(T)/T$ data increase upon cooling for $T \geq 13$ K, reaching a maximum value of 1.34 μV/K^2 at $T_{max} \sim 13$ K. The maximum value of $S(T)/T$ is almost 2 orders of magnitude larger than the maximum values for simple metals such as Cu where $S/T \sim$ -30 nV/K^2. [45] Enhanced values of $S(T)/T$ have been reported for many HF compounds [46, 47, 45] and are considered to be closely related to the strongly-enhanced values of $C(T)/T$. As can be seen in Fig. 5(b), -$S(T)/T$ exhibits a break in slope at a temperature T_{FL}. These observations are qualitatively consistent with the formation of a FL phase as previously inferred from the electronic contribution to specific heat, C_e/T, in which a crossover between NFL and FL phases is observed at T_{FL}. If we extrapolate $S(T)/T$ to zero temperature, we obtain a value of $-S_0/T \sim 1.1(2)$ μV/K^2.

A FL state can be characterized by the ratio of $S_0(T)/T$ to γ. [45, 48, 49] A "quasi-universal" ratio, $q = (N_A e/\gamma)(S/T) \approx \pm 1$, is expected to be obeyed for FL systems where N_A is Avogadro's number and e is the charge of an electron. The sign of q depends on the dominant type of charge carriers. Although a single band and scattering process is generally insufficient to explain the strong correlation effects in materials like HF systems, given that $C(T)/T$ and $S(T)/T$ are most

sensitive to the position of the heavy band, a quasi-universal ratio is expected to hold at low temperature. [50, 51] Using our value of $S_0(T)/T \sim$ -1.1(2) μV/K^2 and $\gamma \sim$ 137 mJ/Yb mol-K^2, we calculate $q \sim$ -0.8(2). Alternatively, if we use $\gamma_0 \sim$ 192 mJ/Yb mol-K^2, we obtain $q \sim$ -0.6(1). The value of q calculated with γ is very close to the expected value for an Yb-based FL system; a value of $q =$ -1 is within the uncertainty, which is dominated by experimental uncertainty in $S_0(T)/T$ (see error bars in Fig. 5(b) at low temperature). This result supports the evidence from specific heat for a FL ground state in $Yb_2Ni_{12}P_7$.

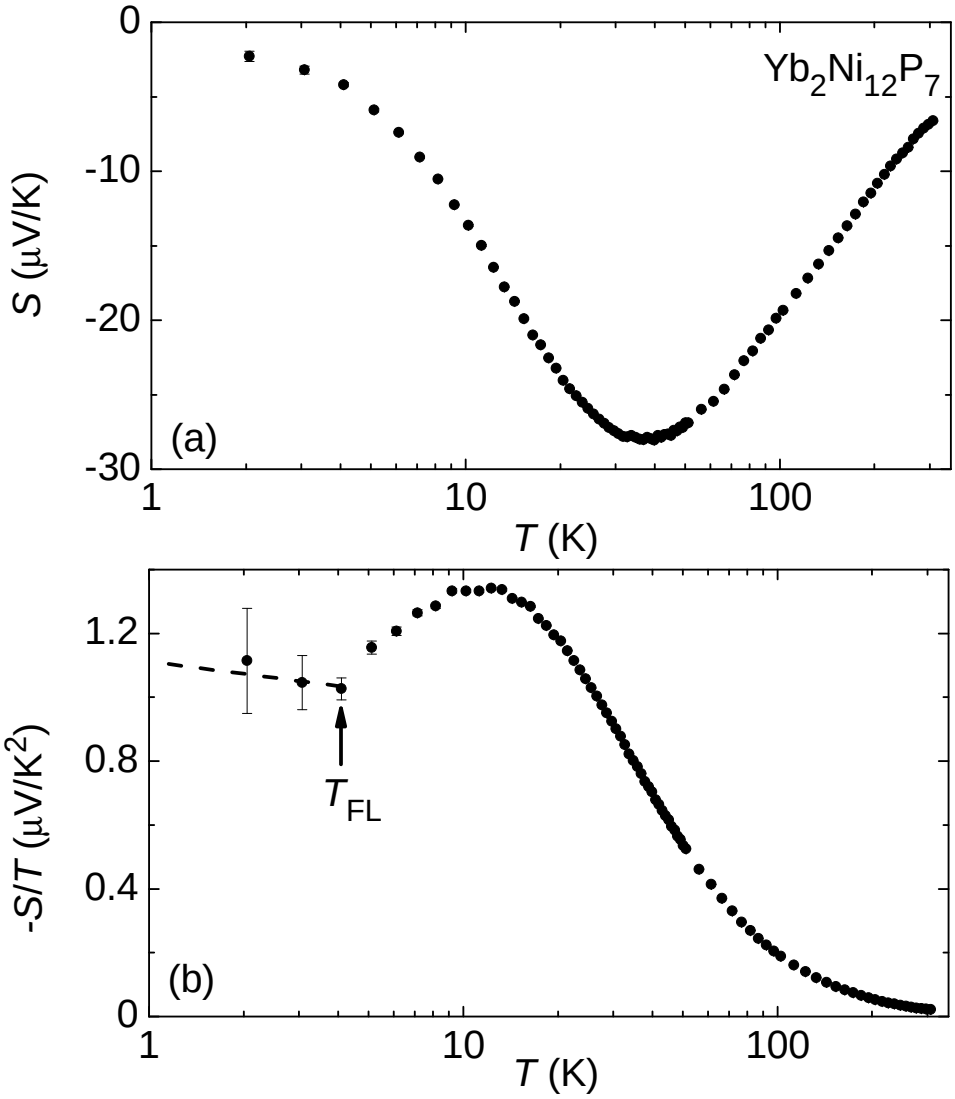

Figure III.5: (a) Thermoelectric power, $S(T)$, for $Yb_2Ni_{12}P_7$ plotted on a semilogarithmic scale. A large negative peak is observed in $S(T)$ near 40 K. (b) $S(T)$ divided by temperature, $S(T)/T$, plotted on a semilogarithmic scale. An arrow explicity designates a temperature, T_{FL}, associated with a cross over from non-Fermi liquid behavior to Fermi liquid behavior for $T \leq T_{FL}$.

III.D Discussion

In order to evaluate potential HF behavior, we calculated the Kadowaki-Woods ratio, $R_{KW} = A/\gamma^2$ where γ, is the coefficient of electronic specific heat and A is the coefficient of the T^2 contribution to ρ. In the original treatment, Kadowaki and Woods reported a universal value $R_{KW} \sim 10^{-5}$ $\mu\Omega$ cm (mol K^2 mJ^{-1})^2 for all HF compounds. [52] More recently, it has been found that many (but not all) Yb-based HF systems are characterised by R_{KW} values that can be two orders of magnitude smaller than the conventional Kadowaki-Woods ratio value. This result is related to the fact that the ground-state degeneracy of $N = 8$ for Yb modifies the conventional Kadowaki-Woods relationship so that it becomes $R^*_{KW} \approx 1 \times 10^{-5}/(\frac{1}{2}N(N-1))$ $\mu\Omega$ cm (mol K^2 mJ^{-1})^2 = 0.36 $\times 10^{-6}$ $\mu\Omega$ cm (mol K^2 mJ^{-1})^2. [53] To calculate the Kadowaki-Woods ratio for $Yb_2Ni_{12}P_7$, it is more reasonable to use γ_0 rather than γ for the electronic contribution. Using our values of $\gamma_0 \sim 192$ mJ/Yb mol-K^2 and $A \sim 0.0458$ $\mu\Omega$ cm/K^2, both obtained for $H = 0$ T, we calculate $R_{KW} \sim 1.24 \times 10^{-6}$ $\mu\Omega$ cm (mol K^2(mJ)$^{-1}$)^2. This value of R_{KW} suggests that $Yb_2Ni_{12}P_7$ has a heavy FL ground state. Similar results are obtained in the case of $H = 9$ T where $R_{KW} \sim 1.20 \times 10^{-6}$ $\mu\Omega$ cm (mol K^2(mJ)$^{-1}$)^2 (calculated using $\gamma_0 \sim 196$ mJ/Yb mol-K^2 and $A \sim 0.0462$ $\mu\Omega$ cm/K^2). Identifying the ground state of $Yb_2Ni_{12}P_7$ as being a heavy FL seems to be at odds with the logarithmic divergence with decreasing T in C_e/T as plotted in Fig. 4(d). The $C_e/T \sim -\ln T$ behavior for $5 \leq T \leq 15$ is a typical characteristic of NFL behavior. [**?**] However, below $T \sim 5$ K, C_e/T tends to saturate with decreasing T, which is indicative of a crossover between FL and NFL behavior in the vicinity of $T \sim 5$ K.

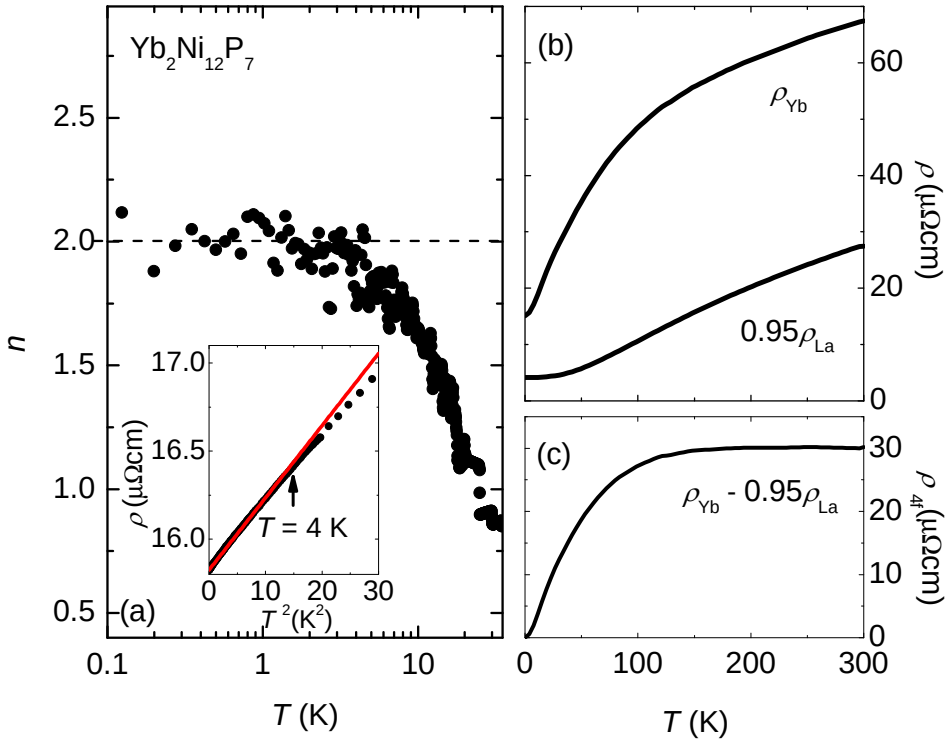

Figure III.6: (a) The exponent, n, defined in the expression, $\rho = \rho_0 + AT^n$, and calculated as described in the text is plotted vs. log T. Inset: ρ vs. T^2 data; the red line emphasizes the temperature range over which ρ exhibits a quadratic temperature dependence. (b) $\rho(T)$ data for $Yb_2Ni_{12}P_7$ and $La_2Ni_{12}P_7$. The $\rho(T)$ data for $La_2Ni_{12}P_7$ have been scaled by a factor of 0.95 so that the slope ($d\rho/dT$) at high temperature is equal to the slope of the $\rho(T)$ data for $Yb_2Ni_{12}P_7$. (c) The $4f$ electron contribution to $\rho(T)$ in $Yb_2Ni_{12}P_7$, ρ_{4f}, plotted vs. T. The ρ_{4f} contribution was obtained by subtracting the scaled $\rho(T)$ data for $La_2Ni_{12}P_7$ from the $\rho(T)$ data for $Yb_2Ni_{12}P_7$.

To further investigate the possibility that there is a crossover between FL and NFL behavior in $Yb_2Ni_{12}P_7$, an analysis of the evolution of the exponent, n, (as defined in Eq. (3)) with temperature was conducted and is plotted in Figure 6(a). It is important to note that Eq. (3) is only valid in temperature regions where electron-phonon scattering and other contributions are negligible (*i.e.*, at low temperature). Since electron-phonon scattering contributes an additive term to $\rho(T)$ that is a power law in temperature according to the Bloch-Grüneisen theory, it is important to subtract this contribution so that $n(T)$ can be meaningfully calculated. Measurements of $\rho(T)$ for $Yb_2Ni_{12}P_7$ and a non-magnetic reference compound, $La_2Ni_{12}P_7$, are shown in Fig. 5(b). The $\rho(T)$ data for $La_2Ni_{12}P_7$ have been scaled by a factor of 0.95, so that their slope matches the slope of $\rho(T)$ data for $Yb_2Ni_{12}P_7$ at high temperatures. The result of subtracting the scaled $\rho(T)$ data of $La_2Ni_{12}P_7$ from data for $Yb_2Ni_{12}P_7$ is plotted in Figure 6(c). The data plotted in Fig. 6(c) are expected to obey a $\rho_{4f} \sim T^n$ temperature dependence at moderately-low temperatures. The exponent, $n(T)$, is calculated by differentiating $\ln \rho(T)$ data with respect to $\ln T$ (*i.e.*, $n = d\ln(\rho - \rho_0)/d\ln T$). As was already shown in the inset of Fig. 3, $n = 2$ at low temperature, indicating a FL ground state; however, above $T \sim 4$ K, n continuously deviates from $n = 2$, rapidly becoming sub-quadratic. This is consistent with ρ vs. T^2 data in the inset of Fig. 6(a) in which a red line emphasises the deviation from a quadratic temperature dependence above $T \sim 4$ K. In analogy with the behavior of C_e/T, this behavior is consistent with a crossover between a FL ground state and NFL behavior in the vicinity of $T \sim 4$ K.

Evidence for a crossover between a FL ground state and NFL behavior is observed in both $C_e(T)/T$ and $\rho(T)$ data. These mutually-reinforcing results strongly suggest the possibility that $Yb_2Ni_{12}P_7$ is in close proximity to a QCP. There are several types of QCP phase diagrams that have been observed in other systems; [11] one commonly observed scenario involves the suppression of an ordered FL state to zero temperature using a non-thermal control parameter δ (*i.e.*,

pressure, magnetic field, chemical composition, etc.) such that a QCP is observed at δ_c. This QCP may or may not be protected by a superconducting phase, but in either case, increasing δ further leads to a region where there is a crossover between a FL state at low temperature and NFL behavior at higher temperature. [11] It is possible that $Yb_2Ni_{12}P_7$ is in such a region where $\delta > \delta_c$. Further work tuning $Yb_2Ni_{12}P_7$ with applied pressure, chemical substitution, and magnetic field will be necessary to observe and identify any QCP that may be present in this system.

III.E Concluding remarks

From measurements of $\rho(T, H)$, $\chi(T, H)$, $C(T, H)$, and $S(T)$ on high-quality single-crystalline samples, we are able to conclude that $Yb_2Ni_{12}P_7$ exhibits a moderately-heavy FL ground state with an enhanced value for $\gamma_0 \sim 192$ mJ/Yb mol-K^2 and a large coefficient A of the T^2 term in the electrical resistivity. These results lead to a Kadowaki-Woods ratio value of $R_{KW} \sim 1.24 \times 10^{-6}$ $\mu\Omega$ cm (mol K^2(mJ)$^{-1}$)^2. An IV Yb state in $Yb_2Ni_{12}P_7$ is inferred from an analysis of $\chi(T)$ data within the context of the ICF model, where an Yb valence of 2.76 is obtained. An intermediate Yb valence is also suggested by the character of $S(T)$. A logarithmic divergence of the electronic contribution to specific heat (*i.e.*, $C_e/T \sim -\ln T$) above $\sim$5 K is strong coincidence for NFL behaviour; however, C_e/T saturates below 5 K, becoming less temperature-dependent indicating there is a FL ground state. An analysis of the power-law exponent, $n(T)$, characterizing the electron-electron scattering contribution to the electrical resistivity yields $n = 2$ at low temperature, which also indicates a FL ground state; however, above $T \sim 4$ K, n continuously decreases and reaches $n = 1$ at ~ 20 K. This behavior is consistent with a crossover in the vicinity of ~ 5 K from a NFL to a FL ground state, strongly suggesting the possibility that $Yb_2Ni_{12}P_7$ is in close proximity to a QCP. Further efforts to tune $Yb_2Ni_{12}P_7$ with applied pressure, chemical substitution, and/or magnetic field will be necessary to observe and then study the potential QCP.

Acknowledgements

A portion of the text and data presented in Chapter 3 are reprints of material that appears in "Crossover between Fermi liquid and non-Fermi liquid behavior in the non-centrosymmetric compound $Yb_2Ni_{12}P_7$," S. Jang, B. D. White, P.-C. Ho, N. Kanchanavatee, M. Janoscheck, and M. B. Maple, J. Phys.: Condens. Matter **26**, 425601 (2014). The dissertation author was the first author of the article.

Bibliography

[1] Z. Fisk, D. W. Hess, C. J. Pethick, D. Pines, J. L. Smith, J. D. Thompson, and J. O. Willis, Science **239**, 33 (1988).

[2] P. W. Anderson, Phys. Rev. **124**, 41 (1961).

[3] W. H. Lee, H. C. Hu, and R. N. Shelton, Phys. Rev. B. **36**, 5739 (1987).

[4] B. Buffat, B. Chevalier, M. H. Tuilier, B. Lloret, and J. Etourneau, Solid State Commun. **59**, 17 (1986).

[5] H. Fujii, T. Inoue, Y. Andoh, T. Takabatake, K. Satoh, Y. Maeno, T. Fujita, J. Sakurai, and Y. Yamaguchi, Phys. Rev. B **39**, 6840 (1989).

[6] T. Takabatake, F. Teshima, H. Fujii, S. Nishigori, T. Suzuki, T. Fujita, Y. Yamaguchi, J. Sakurai, and D. Jaccard, Phys. Rev. B **41**, 9607 (1990).

[7] K. A. Gsheidner, J. Less. Common Metals **17**, 13 (1969).

[8] J. C. P. Klasse, F. R. de Boer, and P. F. de Chatel, Physica B C **106**, 178 (1981).

[9] J. L. Sarrao, C. D. Immer, Z. Fisk, C. H. Booth, E. Figueraoa, J. M. Lawrence, R. Modler, A. L. Cornelius, M. F. Hundley, G. H. Kwei, J. D. Thompson, and F. Bridges, Phys. Rev. B **59**, 6855 (1999).

[10] G. R. Stewart, Rev. Mod. Phys. **73**, 797 (2001).

[11] M. B. Maple M B, R. E. Baumbach, N. P. Butch, J. J. Hamlin, and M. Janoscheck, J. Low. Temp. Phys. **161**, 4 (2010).

[12] E. Ganglberger, Monatsh. Chem. **99**, 557 (1968).

[13] W. Jeitschko, D. J. Braun, R. H. Ashcraft, and R. Marchand, J. Solid State Chem. **25**, 309 (1978)

[14] W. Jeitschko, P. G. Pollmeier, and U Meisen, J. Alloy Compd. **196**, 105 (1993).

[15] A. Hellmann and A. Mewis, Z. Anorg. Allg. Chem. **627**, 1357 (2001).

[16] M. Janoscheck, R. E. Baumbach, J. J. Hamlin, I. K. Lum, and M. B. Maple, J. Phys.: Condens. Mat. **23**, 094221 (2011).

[17] R. E. Baumbach, J. J. Hamlin, M. Janoscheck, I. K. Lum, and M. B. Maple, J. Phys.: Condens. Mat. **23**, 094222 (2011).

[18] R. E. Baumbach, J. J. Hamlin, L. Shu, D. A. Zocco, J. R. O'Brien, P. C. Ho, and M. B. Maple, Phys. Rev. Lett. **105**, 106403 (2010).

[19] B. K. Cho, F. J.DiSalvo, J. S. Kim, G. R. Stewart, and S. Bud'ko, Phys. Rev. Lett. **253**, 40 (1998).

[20] T. Nakano, R. Satoh, K. Tsuchiya, N. Takeda, K. Matsubyashi, and Y. Uwatoko, J. Phys.: Conf. Ser. **391**, 012052 (2012).

[21] H. M. Rietveld, J. Appl. Cryst. **2**, 65 (1969).

[22] A. Larson and R. V. Dreele, Los Alamos National Laboratory Report, 86-748 (2000).

[23] W. Jeitchko and B. Jaberg, J. Less-Common Mat. **79**, 311 (1981).

[24] D. T. Adroja, S. K. Malik, B. D. Padalia, and R. Vijayaraghavan, Phys. Rev. B **39**, 4831 (1989).

[25] W. C. M. Mattens, R. A. Elenbaas, and F. R. de Boer, Commum. Phys. **2**, 147 (1977).

[26] E. E. Havinga, K. H. J. Buschow, and H. J. van Daal, Solid State Comm. **13**, 621 (1973).

[27] D. T. Adroja, S. K. Malik, B. D. Padalia, S. N. Bhatia, R. Walia, and R. Vijayaraghavan, Phys. Rev. B **42**, 2700 (1990).

[28] I. R. Fisher, S. L. Bud'ko, C. Song, P. C. Canfield, T. C. Ozawa, and S. M. Kauzlarich, Phys. Rev. Lett. **85**, 1120 (2000).

[29] M. B. Maple and D. K. Wohlleben, AIP Conf. Proc. **18**, 447 (1974).

[30] B. C. Sales and D. K. Wohlleben, Phys. Rev. Lett. **35**, 1240 (1975).

[31] M. T. Bealmonod and J. M. Lawrence, Phys. Rev. B **21**, 5400 (1980).

[32] K. Andres, J. E. Graebner, and H. R.Ott, Phys. Rev. Lett. **35**, 1779 (1975).

[33] S. K. Malik, D. T. Adroja, M. Slaski, B. D. Dunlap, and A. Umezawa, Phys. Rev. B **40**, 9378 (1989).

[34] C. Rossel, K. N. Yang, M. B. Maple, Z. Fisk, E. Zirngiebl, and J. D. Thompson, Phys. Rev. B **35**, 1914 (1987).

[35] C. L. Seaman, M. B. Maple, B. W. Lee, S. Ghamaty, M. S. Torikachvili, J. S. Kang, L. Z. Liu, J. W. Allen, and D. L. Cox, Phys. Rev. Lett. **67**, 2882 (1991).

[36] B. Andraka and A. M. Tsvelic, Phys. Rev. Lett. **67**, 2886 (1991).

[37] D. A. Gajewski, P. Allenspach, C. L. Seaman, and M. B. Maple, Physica B **419**, 199 (1994).

[38] H. Amitsuka, T. Hidano, T. Honma, H. Mitamura, and T. Sakakibara, Physica B **337**, 186 (1996).

[39] B. Andraka and G. R. Stewart, Phys. Rev. B **47**, 3208 (1993).

[40] R. Yamanaka, K. Matsubayashi, Y. Saiga, T. Kawae, and Y. Uwatoko, J. Phys.: Conf. Ser. **391**, 012078 (2012).

[41] D. Andreica, K. Alami-Yadri, D. Jaccard, A. Amato, and D. Schenck, Physica B **259**, 144 (1999).

[42] M. Deppe, S. Hartmann, M. E. Macovei, N. Oeschler, M. Nicklas, and C. Geibel, New J. Phys. **10**, 093017 (2008).

[43] S. Friedemann, Physica (Amsterdam) **403**, 1254 (2008).

[44] V. Zlatic and R. Monnier, Phys. Rev. B **71**, 165109 (2005).

[45] K. Behnia, D. Jaccard, and J. Flouquet, J. Phys. Condens. Matter **16**, 5187 (2004).

[46] K. Izawa, K. Behnia, Y. Matsuda, H. Shishido, R. Settai, Y. Onuki, and J. Flouquet, Phys. Rev. Lett. **99**, 147005 (2007).

[47] S. Hartmann, N. Oeschler, C. Krellner, C. Geibel, S. Paschen, and F. Steglich, Phys. Rev. Lett. **104**, 096401 (2010).

[48] C. Grenzebach, F. B. Anders, G. Czycholl, and T. Pruschke, Phys. Rev. B **74**, 195119 (2006).

[49] V. Zlatic, R. Monnier, J. K. Freericks, and K. W. Becker, Phys. Rev. B **76**, 085122 (2007).

[50] K. Miyake and H. Kohno, J. Phys. Soc. Jpn. **74**, 254 (2005).

[51] H. Kontani, Phys. Rev. B **67**, 014408 (2003).

[52] K. Kadowaki and S. B. Woods, Solid State Commum. **58**, 507 (1986).

[53] N. Tsujii, H. Kontani, and K. Yoshimura, Phys. Rev. Lett. **94**, 057201 (2005).

Chapter IV

Itinerant ferromagnetism in the noncentrosymmetric heavy-fermion compound $Sm_2Ni_{12}P_7$

IV.A Introduction

Heavy-fermion (HF) ground states are found in intermetallic compounds containing lanthanide and actinide ions with unfilled $4f$ or $5f$ electron shells including Ce, Pr, Sm, Yb, and U. Particularly, an intense research effort has focused on investigation Sm-based intermetallic compounds which often shows interesting phenomenon due to: (1) the potential for spin fluctuations of the Sm ion between $4f^6$ (Sm^{2+}) and $4f^5$ (Sm^{3+}) electronic configurations and (2) the excited $J = 7/2$ total angular momentum state is generally not separated from the $J = 5/2$ Hund's rule ground state by a large energy; this second point allows for the possibility of J-mixing at modest temperatures and leads to a considerable Van Vleck paramagnetic contribution in measurements of the magnetization. For example, the compounds SmX (X = Te, Se, or S) exhibit semiconductor-metal transitions un-

der applied pressure which are associated with a sudden change in the Sm valence driven by an enhancement of the hybridization strength between the localized $4f$ and itinerant electron states. [1, 2] In more modern parlance, f-electron materials such as SmB_6 [3] that display such behaviors are referred to as "Kondo insulators". Observations of topologically-protected surface states have made SmB_6 the subject of considerable attention recently; [4] this property would make SmB_6 the first "topological Kondo insulator". Although quite rare in Sm-based systems, the single-ion Kondo effect is observed in the system $La_{1-x}Sm_xSn_3$ as inferred from the $-\ln T$ temperature dependence of the electrical resistivity at low temperature. [5, 6] Recent experiments on Sm-based filled skutterudite compounds [7, 8] shows some interesting phenomenon, such as a metal-insulator transition has been observed for $SmRu_4P_{12}$ compound at $T_{MI} = 16.5$ K, and octupolar order below T_{MI} that has been proposed to explain the sharp drop in the elastic constant [9, 10]. Also, $SmOs_4Sb_{12}$ compound have displayed unusual field-insensitive HF behavior [11, 12].

The family of compounds with chemical formula $Ln_2T_{12}M_7$ are the $n = 2$ members of a broader class of pnictogen-based systems with chemical formula $Ln_{n(n-1)}T_{(n+1)(n+2)}M_{n(n+1)+1}$, where Ln is a lanthanide (or actinide), T is a transition metal, and M is a pnictogen (*i.e.*, phosphorus, arsenic). [14, 13, 15] We have recently investigated the correlated electron properties in many members of this family of compounds. For example, $Yb_2Fe_{12}P_7$ exhibits a crossover from a magnetically-ordered to a paramagnetic non-Fermi liquid (NFL) state at low temperature in a magnetic field near $H = 1$ T. [16] Complicated magnetic behavior is observed in the compound $U_2Fe_{12}P_7$, which is manifested by hysteretic temperature and magnetic field dependencies in magnetization measurements, metamagnetic behavior, and large spin-disorder scattering of conduction electrons for $T > T_N$. [17] The Yb ions in the HF compound $Yb_2Ni_{12}P_7$ exhibit an intermediate valence [21]. A crossover between FL and NFL states is also observed at zero field near 5 K, suggesting the possibility of a nearby quantum critical point (QCP) in

$Yb_2Ni_{12}P_7$. [21] Finally, the compound $Sm_2Fe_{12}P_7$ was found to be an itinerant ferromagnet with evidence for a heavy FL ground state; furthermore, it may also be in close proximity to a QCP. [19] In general, the "2-12-7" family of compounds is interesting because they provide an opportunity to study strong electronic correlations and magnetism within a noncentrosymmetric crystal structure.

Recently, measurements of electrical resistivity, magnetization, and specific heat on single crystals of $Sm_2Ni_{12}P_7$ were reported by Nakano *et al.* as part of a study on the compounds $Ln_2Ni_{12}P_7$ (Ln = Sm, Gd-Lu); [20] they reported evidence for magnetic order in $Sm_2Ni_{12}P_7$ near 5 K and preliminarily identified it as being either ferrimagnetic or some other form of complex magnetic order such as canted ferromagnetism [20]. However, no analysis to obtain the Sommerfeld coefficient γ, or to assess the low-temperature physical properties was presented as part of the study. In light of the recent study on $Sm_2Fe_{12}P_7$ by Janoschek *et al.* [19], we were motivated to determine whether $Sm_2Ni_{12}P_7$ might be another example of a Sm-based HF ferromagnet; such compounds are quite rare and include, to our knowledge, only $SmFe_4P_{12}$, [22] $SmOs_4Sb_{12}$, [12] SmPtSi, [23] and the aforementioned $Sm_2Fe_{12}P_7$. [19] In this paper, we present a comprehensive study on single crystals of the noncentrosymmetric compound $Sm_2Ni_{12}P_7$ from measurements and analysis of electrical resistivity, magnetization, and specific heat data. Our results indicate that $Sm_2Ni_{12}P_7$ is an itinerant ferromagnet that appears to exhibit a heavy FL ground state.

IV.B Experimental details

Single crystals of $Sm_2Ni_{12}P_7$ were grown in a molten Sn flux with a ratio of Sm:Ni:P:Sn = 1:4:2:30 using Sm (small dendrite pieces), Ni (chunks), and P (small lump) with purities of 99.9% or better. The starting materials were sealed under an Ar-atmosphere of ∼250 torr at room temperature in a quartz tube, heated to 1150 °C, dwelled for 24 hours, and were allowed to cool slowly to 600 °C over

168 hours. Excess Sn flux was spun off using a centrifuge and residual Sn on the surface of the crystals was etched away with dilute HCl. In this way, needle-shaped single crystals were obtained with typical dimensions of $4 \times 0.1 \times 0.1$ mm^3.

X-ray diffraction measurements were performed on powdered single crystals using a Bruker D8 Discoverer x-ray diffractometer. The resulting data were refined by means of Rietveld analysis [24] as implemented in the program suite GSAS. [25] Isothermal magnetization $M(H)$ and magnetization $M(T)/H$ measurements were performed in magnetic fields $\mu_0 H$ up to 7 T and from 2 to 300 K, respectively, with field applied both parallel and perpendicular to the crystallographic ab-plane, using a Quantum Design (QD) Magnetic Property Measurement System (MPMS). Specific heat was measured from 2 to 50 K in a QD Physical Property Measurement System (PPMS) DynaCool using a standard thermal relaxation technique. Electrical resistivity measurements were carried out in a four-wire configuration between $T = 1.2$ and 300 K in a ^{4}He dewar.

IV.C Results

Rietveld refinement analysis of the x-ray diffraction data shows that the single crystals of $Sm_2Ni_{12}P_7$ crystallize in the hexagonal noncentrosymmetric space group $P\bar{6}$ with lattice parameters $a = 9.081$ Å and $c = 3.711$ Å. These values agree well with those reported in other studies of $Sm_2Ni_{12}P_7$ [15, 20].

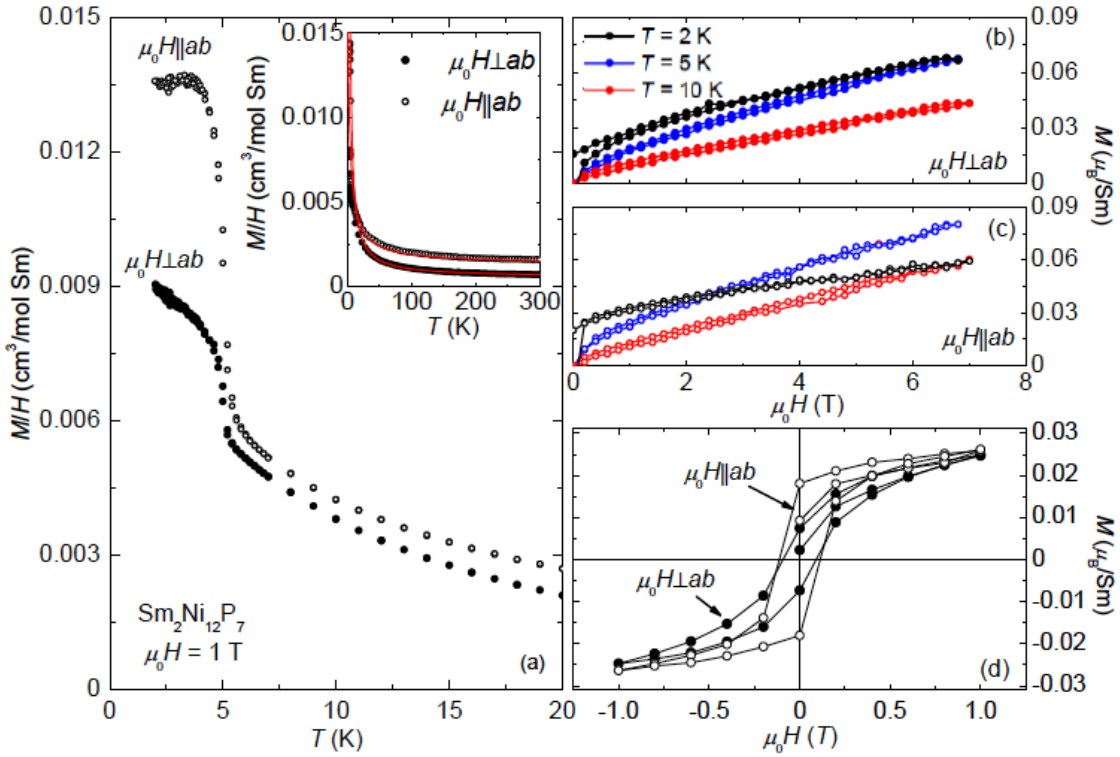

Figure IV.1: (a) Magnetization M/H versus temperature T for a magnetic field $\mu_0 H$ applied parallel and perpendicular to the ab-plane in the T range between 2 to 20 K. M/H data for T between 2 to 300 K are plotted in the inset. Red lines represent modified Curie-Weiss law fits to the data using Eq. (1) as described in the text. (b) Isothermal magnetization M versus $\mu_0 H$ for $\mu_0 H \perp$ab-plane at 2 K, 5 K, and 10 K. (c) Isothermal magnetization M versus $\mu_0 H$ for $\mu_0 H \|$ab-plane. (d) Hysteresis curve at $T = 2$ K in the range -1 $< \mu_0 H <$ 1 T with magnetic field applied along each direction.

Measurements of the magnetization as a function of temperature, $M(T)/H$, from 2 to 300 K in an applied magnetic field $\mu_0 H = 1$ T, aligned both parallel and perpendicular to the basal plane, are presented in Figure VI.1(a). Both sets of data show a ferromagnetic transition at a Curie temperature of $T_C \sim 5$ K. The difference in the magnitude for each direction indicates that the easy direction lies within the *ab*-basal plane, providing an enhanced M/H value as $T \rightarrow 0$ K of $M_0/H \sim 0.0135$ cm^3/Sm when $H \parallel$ ab, relative to the value obtained for the hard direction ($M_0/H \sim 0.0098$ cm^3/Sm).

Since Sm^{3+} ions have excited angular momentum states that are separated by relatively low energy from the Hund's rule $J = 5/2$ ground state, a simple Curie-Weiss law is insufficient to describe the $M(T)/H$ data for $Sm_2Ni_{12}P_7$. As is shown in the inset of Figure VI.1(a), $M(T)/H$ data are fitted well with Eq. (1) and the best fits are represented by the red lines. Equation (1),

$$\frac{M(T)}{H} = \frac{N_A}{3k_B}\left[\frac{\mu_{eff}^2}{(T-\theta)} + \frac{\mu_B^2}{\delta}\right] + \chi_P, \qquad \text{(IV.1)}$$

consists of a Curie-Weiss term due to the $J = 5/2$ ground state contribution and a temperature-independent Van Vleck term due to coupling with the excited $J = 7/2$ multiplet located a temperature δ above the ground state, [**?**] where N_A is Avogadro's number, k_B is Boltzmann's constant, μ_{eff} is the effective magnetic moment, θ is the Curie-Weiss temperature, and μ_B is the Bohr magneton. A Pauli-like contribution term, χ_P, from the conduction electrons can be estimated from the χ_P contribution to $Lu_2Ni_{12}P_7$ magnetic susceptibility data; [20] we estimate an upper limit of $\chi_P \leq 0.00025$ emu/mol Lu. If crystalline electric field (CEF) effects are neglected, the theoretical Sm^{3+} free-ion moment is described as $\mu_{eff} = g_J\sqrt{J(J+1)}\ \mu_B = 0.85\ \mu_B$/Sm, where the Landé g factor is $g_J = 0.286$ and $J = 5/2$. The best fit of Eq. (1) to the $M(T)/H$ data is obtained with the parameters θ = -3.5 and 1.1 K, δ = 112 and 416 K, and $\mu_{eff} = 0.66$ and 0.65 μ_B/Sm for the easy and hard directions, respectively. This analysis assume χ_P is 0.00025 emu/mol Sm. The values of μ_{eff} are somewhat less than the theoretical Sm^{3+} free ion value;

possible valence fluctuations of the Sm ion might be responsible for these reduced values of μ_{eff}. We are able to calculate the temperature difference between the J = 5/2 and 7/2 states, Δ, using the relationship $\delta = 7\Delta/20$. [12, 27] The results are Δ = 112 and 1189 K as obtained from fits to measurements with the magnetic field applied along the easy and hard directions, respectively; these values are less than the $\Delta \sim 1500$ K value estimated for the free Sm^{3+} ion. [28] In the case of $Sm_2Fe_{12}P_7$, the reported Δ value is estimated to be Δ = 1503 K. [19] A reduced value of Δ is often found in other Sm-based compounds including $SmRh_4B_4$ (Δ = 1080 K), $SmCo_2Cd_{20}$ (Δ = 412 K), and $SmRu_2Cd_{20}$ (Δ = 265 K). [27, 29]

The results of isothermal magnetization, $M(H)$, measurements, made in magnetic fields up to $\mu_0 H = 7$ T for $T = 2$, 5, and 10 K, are shown in Figure VI.1(b) and (c). Even though saturation is not achieved at $T = 2$ K along either direction, magnetization values of μ_{sat} = 0.059(1) and 0.024(1) μ_B/Sm can be estimated for the easy and hard directions by using the measured values at $\mu_0 H = 7$ T. These values are less than 10% of the theoretical value of μ_{sat} = 0.71 μ_B/Sm for the Sm^{3+} ion. The ratios of the effective magnetic moment to the saturation magnetic moment, also referred to as the Rhodes-Wolfarth ratio, [30] are $\mu_{eff}/\mu_{sat} \sim 11$ and 12 when using values obtained from measurements with magnetic field applied along the easy and hard directions, respectively. These reduced values of μ_{sat} are consistent with itinerant-electron ferromagnetic order. [30] A small unsaturated value of the magnetization is also observed in other weak itinerant ferromagnets, such as $ZrZn_2$, Ni_3Al, and Sc_3In. [31, 32]

The magnetization data from measurements with $H \| ab$ at $T = 2$ K and T = 5 K intersect near $\mu_0 H \sim 3$ T. This result indicates the possibility of a magnetic field-induced antiferromagnetic (AFM) transition at a temperature below $T_C \sim$ 5 K, when $H \| ab$ and $\mu_0 H \geq 2.5$ T. The related compound $Sm_2Fe_{12}P_7$ exhibits multiple magnetic phase transitions at $T_C \sim 6.3$ K and $T_N \sim 3.7$ K, indicating that magnetism in $Sm_2T_{12}P_7$ compounds, associated with magnetic moments from Sm-ions, is complicated. [19] Furthermore, $Sm_2Fe_{12}P_7$ exhibits a similar intersec-

tion of $M(H)$ curves that is identified as evidence of a metamagnetic transition when $H \| c$. [19] Since, the Pauli paramagnetic susceptibility of itinerant electron states is proportional to $N(E_F)$ another possible explanation for the decrease of magnetization at $T = 2$ K could be the opening of a gap on the Fermi Surface with assuming T_K is higher than 2 K and lower than 100 K which temperature range is lower than the temperature range for fitting Eq. (1). The formation of an energy gap [33] on the Fermi surface near $\mu_0 H \sim 3$ T might be responsible for the reduction in M/H. The ferromagnetic phase transition can clearly be seen in Figure VI.1(d) where the low field curvature is more pronounced at lower temperatures and clear hysteresis is observed at 2 K. These results reveal the presence of weak ferromagnetic order below $T_C = 5$ K. At 2 K, a higher remanent magnetization of $M_R \sim 0.008(1)$ μ_B/Sm is observed for the easy direction than $M_R \sim 0.004(1)$ μ_B/Sm for the hard direction.

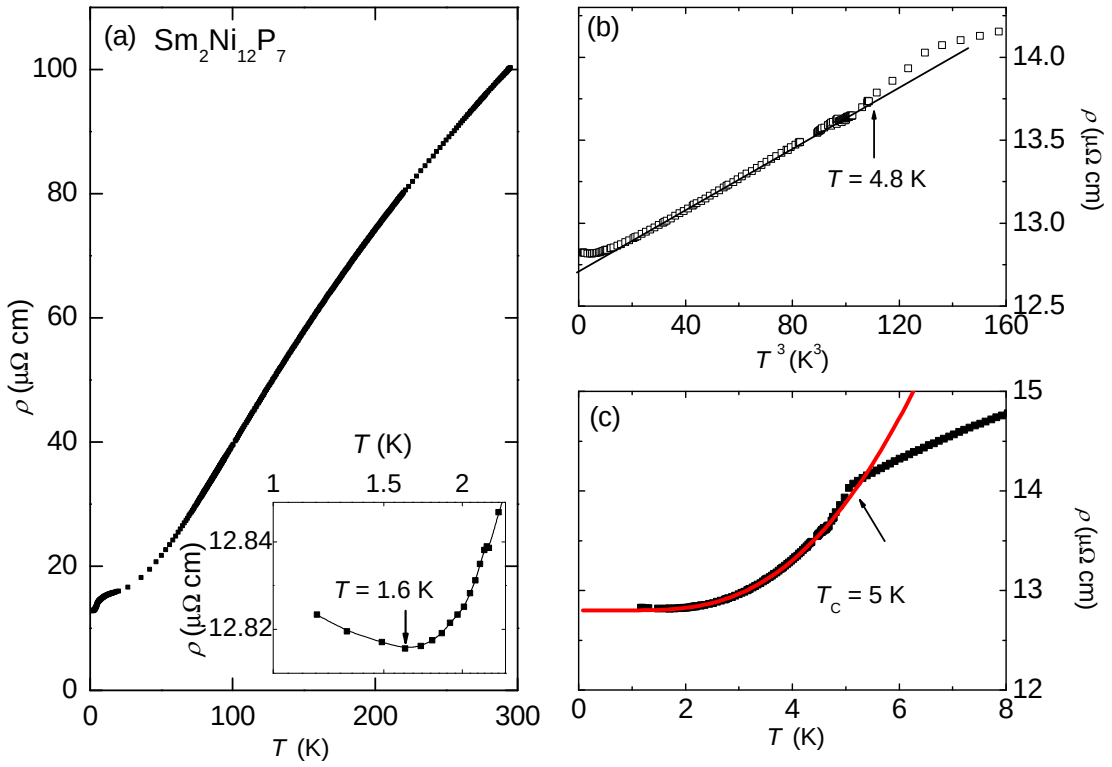

Figure IV.2: (a) Electrical resistivity ρ as a function of temperature T. The inset shows low-temperature $\rho(T)$ data with a logarithmic temperature scale, revealing an upturn below $T \sim 1.6$ K. (b) ρ versus T^3 data for $Sm_2Ni_{12}P_7$ with a linear fit between 1.6 K $< T \leq$ 4.8 K. (c) An arrow highlights the onset of ferromagnetic order near $T_C = 5$ K. A solid line represents a fit to the $\rho(T)$ data using Eq. (2), which includes magnetic excitations.

The electrical resistivity as a function of temperature, $\rho(T)$, for $Sm_2Ni_{12}P_7$ is plotted in Figure VI.2(a). $\rho(T)$ decreases smoothly from room temperature to a shoulder feature near $T \sim 30$ K, which can be related to depopulation of an excited state of the $J = 5/2$ multiplet that has split from the ground state by the CEF. A low-temperature feature near $T_C \sim 5$ K is associated with ferromagnetic order which is consistent with the T_C determined from the magnetization data in Figure VI.1. As we present in the inset of Figure VI.2, an upturn is observed below $T < 1.6$ K, which might be associated with Kondo-like spin-flip scattering. NFL behavior of the form $\rho = \rho_0 \pm AT^n$ where $n \leq 1.5$ [34] is another possible scenario to explain this upturn behavior; however, we were unable to observe evidence for NFL behaviour in the other physical properties, so this scenario is less likely. It will be necessary to measure $\rho(T)$ of $Sm_2Ni_{12}P_7$ to much lower temperatures (lower than $T < 1.2$ K) to clarify the origin of this upturn. As is presented in Figure VI.2(b), the $\rho(T)$ data are fitted well up to ~ 4.8 K with a power-law behavior $\rho = \rho_0 + AT^n$ where $n \sim 3$; this value of n is inconsistent with the expected results for both FL ($n \sim 2$) and NFL ($n \leq 1.5$) behavior. [34] The $\rho(T)$ data, in this temperature range, include contributions from scattering with magnons below T_C, so this T^3 behavior arises from a contribution of scattering with itinerant quasiparticles and magnons.

In Figure VI.2(c), we present ρ data for $T \leq 8$ K; the low-temperature feature at $T_C \sim 5$ K is associated with the ferromagnetic phase transition, which is concomitant with the formation of a gap opening on the Fermi surface as we observe in C/T data presented below. At temperatures less than $T_C = 5$ K, the scattering of electrons with ferromagnetic excitations can be estimated by fitting the electrical resistivity data with the expression, [1, 2]

$$\rho(T) = \rho_0 + B\frac{T}{\Delta_{\rho,SW}}(1 + 2\frac{T}{\Delta_{\rho,SW}})\exp(-\frac{\Delta_{\rho,SW}}{T}), \qquad \text{(IV.2)}$$

where ρ_0 is the residual electrical resistivity, B is a coefficient, and $\Delta_{\rho,SW}$ is the spin-wave energy gap associated with ferromagnetic order. Red lines represent best

fits of Eq. (2) to the experimental data presented in Figure VI.2(c). We obtained best-fit values of $\rho_0 = 12.8(1)$ $\mu\Omega$ cm, $B = 0.3(1)$ $\mu\Omega$ cm, and $\Delta_{\rho,SW} = 3.8$ K.

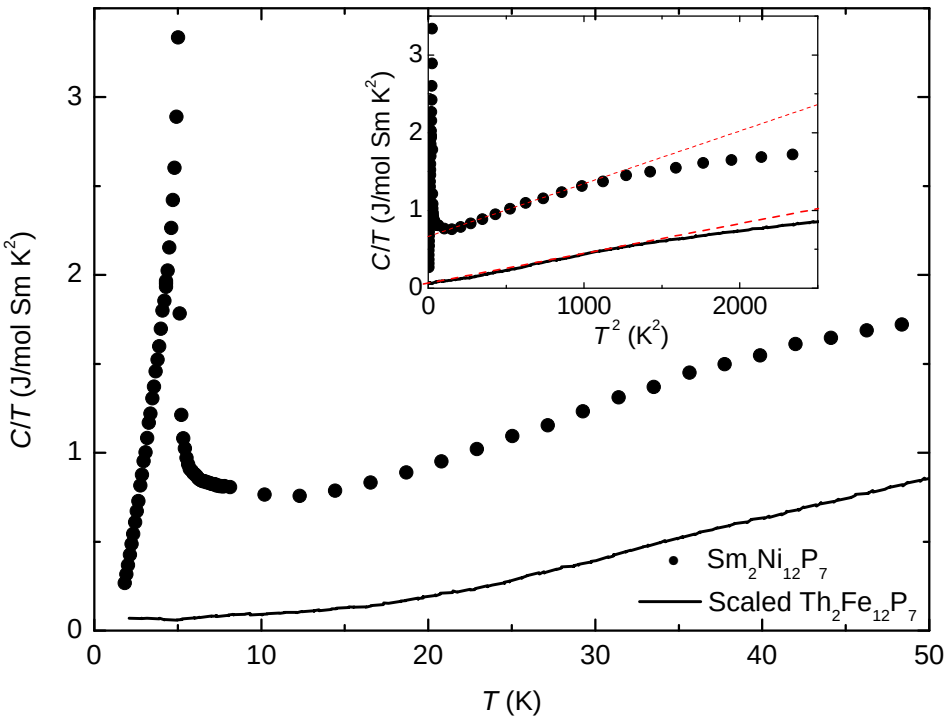

Figure IV.3: Specific heat C divided by temperature T for $Sm_2Ni_{12}P_7$ and $Th_2Fe_{12}P_7$; the data for $Th_2Fe_{12}P_7$ are from Ref. [17] and they have been scaled by factors of $\sqrt{m_{Sm}/m_{Th}}$ and $\sqrt{m_{Ni}/m_{Fe}}$ to account for differences in the Debye temperatures of $Th_2Fe_{12}P_7$ and $Sm_2Ni_{12}P_7$. The inset shows C/T data versus T^2 for $Sm_2Ni_{12}P_7$ and $Th_2Fe_{12}P_7$ (scaled). The dashed red lines are linear fits to these data.

The specific heat divided by temperature, $C(T)/T$, for $Sm_2Ni_{12}P_7$ is shown in Figure VI.3 with $C(T)/T$ data for $Th_2Fe_{12}P_7$ that have been scaled by factors of $\sqrt{m_{Sm}/m_{Th}}$ and $\sqrt{m_{Ni}/m_{Fe}}$ to account for differences in mass between Th and Sm, and Ni and Fe; we use the scaled $C(T)/T$ data for $Th_2Fe_{12}P_7$ to estimate the phonon contribution to $C(T)/T$ data for $Sm_2Ni_{12}P_7$. A pronounced peak at $T_C \sim 5$ K is commensurate with the ferromagnetism observed as a cusp in $M(T)$ data and the analogous feature in $\rho(T)$ data. As presented in the inset of Figure VI.3 as a dashed red line, C/T data for $Sm_2Ni_{12}P_7$ above the transition can be described as $C/T = \gamma + \beta T^2$ where $\gamma \sim 644$ mJ/mol Sm K^2 and $\beta \sim 1.4$ mJ/mol Sm K^4. We obtain a Debye temperature $\theta_D \sim 308$ K from this value of β. We are able to estimate $\theta_D \sim 364$ K for scaled $C(T)/T$ data for $Th_2Fe_{12}P_7$ using $\beta = 0.8$ mJ/mol K^4; this value of θ_D is higher than the θ_D value for $Sm_2Ni_{12}P_7$, but the difference between them is sufficiently small to justify using the scaled $C(T)/T$ data for $Th_2Fe_{12}P_7$ to estimate the phonon contribution to $C(T)/T$ data for $Sm_2Ni_{12}P_7$.

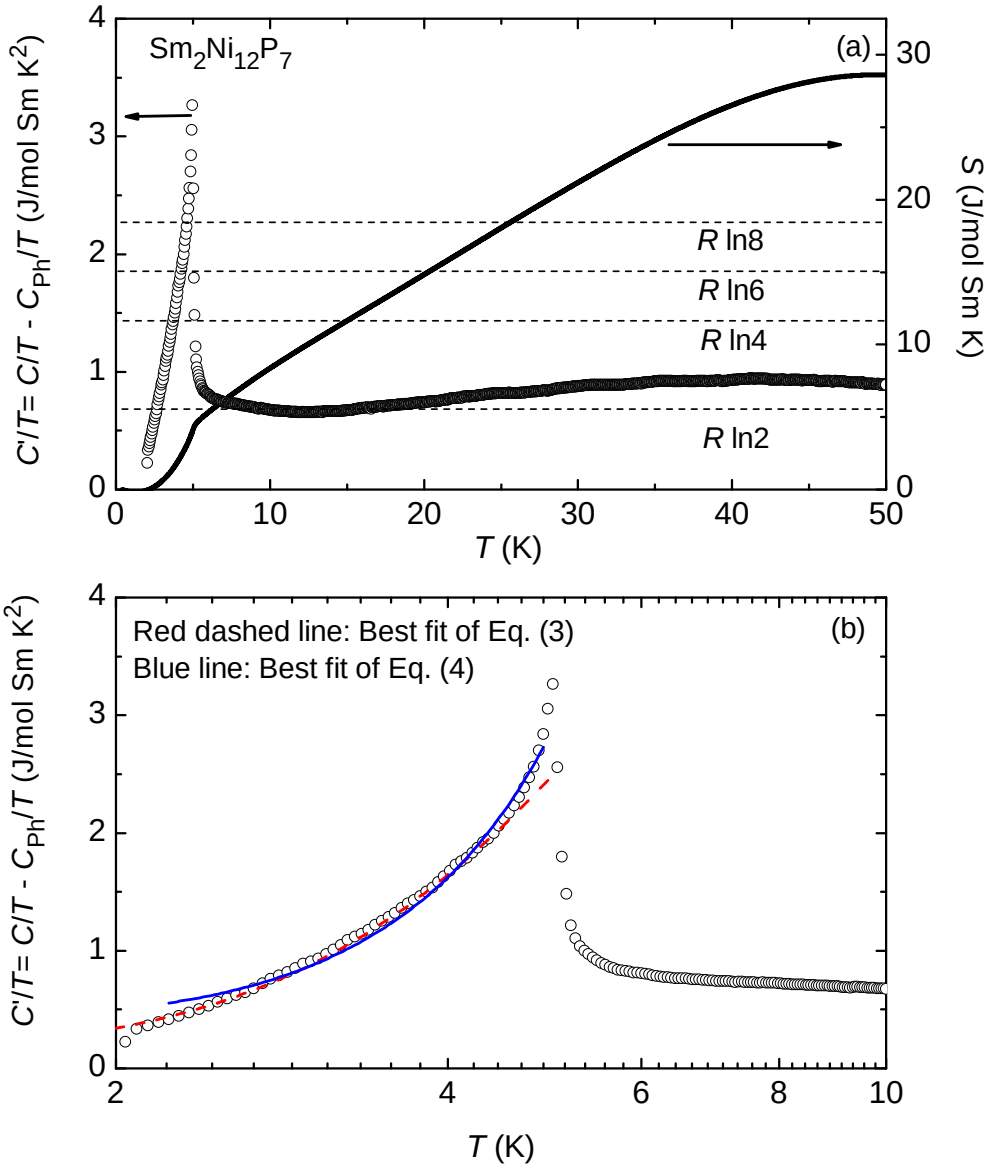

Figure IV.4: (a) The specific heat $C'(T)/T$ after subtracting the phonon contribution. The solid line represents the combined electronic and magnetic entropy, $S(T)$, of $Sm_2Ni_{12}P_7$, calculated by integrating $C'(T)/T$ data. Dashed lines denote specific entropy values which are explicitly labeled. (b) $C'(T)/T$ data plotted vs. $\ln T$ along with best fits of Eq. (3) and Eq. (4) to the data for $T < T_C$, presented as a red dashed line and blue line, respectively.

IV.D Discussion

Figure VI.4 shows specific heat data for $Sm_2Ni_{12}P_7$, $C'(T)/T$, obtained by subtracting the phonon contribution as estimated by scaled data for the non-magnetic reference compound $Th_2Fe_{12}P_7$ (see Figure 3). We can estimate the Sommerfeld coefficient value using $C'(T)/T$ data in the paramagnetic state ($T >$ 5 K) to be $\gamma_P = 650$ mJ/mol Sm K^2. This relatively large value is similar to the value of γ, which was estimated from a linear fit of C/T vs. T^2 data in the inset of Figure 3, by assuming that the low-temperature behavior could be modelled as $C/T = \gamma + \beta T^2$. We observe a broad hump at $T \sim 40$ K in $C'(T)/T$ data, which coincides with the temperature of the shoulder feature in $\rho(T)$ data. The origins of these features are likely both associated with splitting of the $J = 5/2$ Sm multiplet by the CEF.

The entropy associated with the electronic and magnetic degrees of freedom, $S(T)$, has been calculated by integration, $S(T) = \int (C'/T)dT$, and is presented in Figure VI.4(a). The total entropy released at T_C is $0.9R\ln 2$ J/mol Sm K and reaches 28 J/mol Sm K at 50 K, which shows excess entropy relative to theoretical magnetic contributions $R\ln(2J+1) = 14.9$ J/mol Sm K for $J = 5/2$ or 17.3 J/mol Sm K for $J = 7/2$. This is primarily a result of including the large electronic contributions to the entropy. In order to determine the magnetic contribution to entropy near T_C, the electronic contribution needs to be subtracted from $S(T)$, which is estimated to be γT_C. Using this estimate for the electronic contribution to entropy below T_C, a magnetic entropy of $0.3R\ln 2$ J/mol Sm K is released at T_C. This value is much less than the value expected for localized magnetic moments from spin 1/2, as predicted by the Stoner-Wohlfarth theory, [35] and provides further evidence that $Sm_2Ni_{12}P_7$ is an itinerant ferromagnet.

The feature in C'/T data at $T_C \sim 5$ K is associated with ferromagnetic order, consistent with our $M(T)$ and $\rho(T)$ data. $C'(T)/T$ decreases exponentially for $T < T_C$, suggesting that an energy gap opens on the Fermi surface. In order to

study this behavior, we performed fits involving two scenarios. First, we assume that the gap is associated with the spin-wave (magnon) spectrum. In this case, the C'/T data at low temperature can be described by the expression, [36]

$$C'/T = C/T - C_{Ph}/T = C_{el}/T + C_{mag}/T = \gamma_0 + \beta_0 T^{1/2} \exp(-\frac{\Delta_{C,SW}}{k_B T}), \quad \text{(IV.3)}$$

where $\Delta_{C,SW}$ is the magnon energy gap, β_0 is a coefficient, and γ_0 is defined as C'/T in the limit $T \rightarrow 0$ K. The best fit of $C'(T)/T$ data by Eq. (3) yielded values of $\gamma_0 = 165$ mJ/mol Sm K^2, $\beta_0 = 9.9$ J/mol Sm K$^{3/2}$, and $\Delta_{C,SW} = 6.5$ K. The $\Delta_{C,SW}$ value is reasonably close to $\Delta_{\rho,SW} = 3.8$ K. However, γ_0 is obviously reduced relative to γ_P, but is still considerably larger than for a conventional uncorrelated metal. This difference between γ_0 and γ_P values can be explained by the formation of an energy gap over a portion of the Fermi surface in $Sm_2Ni_{12}P_7$. We find that the gap removes about $\gamma_0/\gamma_P \sim 70$ - 75% of the Fermi surface. A fit of the data can also be made with the expression,

$$C' = \gamma_0 + \beta_1 \exp(-\frac{\Delta_{C,FS}}{k_B T}), \quad \text{(IV.4)}$$

which is a general behavior associated with an energy gap opening on the Fermi surface. The best fit values from such a fit are with $\beta_1 = 14.2$ J/mol Sm K and $\Delta_{C,FS} = 8.9$ K (red dashed line in Figure 4(b)) where $\Delta_{C,FS}$ is the energy gap which opens on the Fermi surface. It is interesting to note that the values of the energy gap from Eq. (3) and Eq. (4) are comparable to each other. In order to determine whether the energy gap opens on the Fermi surface or is associated with a gap in the spin-wave spectrum, it will be necessary to measure the spin-wave spectra using neutron scattering or muon scattering measurements.

The Wilson-Sommerfeld ratio, $R_W = (\pi^2 k_B^2/(\mu_{eff}^2))\chi_0/\gamma_0$, where k_B is the Boltzmann constant, μ_{eff} is the effective magnetic moment, and χ_0 is the Pauli susceptibility, [37] is close to 1 for a free electron gas. [38] By using $\gamma_0 =$

165 mJ/mol Sm K^2 and the χ_0 value obtained at the lowest temperatures when the magnetic field is applied along the easy direction, we are able to estimate $R_W \sim 0.9$, and $R_W \sim 1.1$ for the hard direction; these values are close to 1. We used γ_0 instead of γ_P because the χ_0 value was obtained in the temperature limit $T \ll T_C$, and γ_P was determined for $T > T_C$. This result provides additional support for identifying $Sm_2Ni_{12}P_7$ as a heavy-fermion compound.

IV.E Summary

We reported measurements of the electrical resistivity, magnetization, and specific heat for single crystals of the noncentrosymmetric compound $Sm_2Ni_{12}P_7$. This compound exhibits ferromagnetic order with $T_C = 5$ K that is associated with itinerant electron states as indicated by the calculated Rhodes-Wolfarth ratio and the relatively small magnetic entropy released at T_C. We have observed evidence that $Sm_2Ni_{12}P_7$ is also a heavy-fermion compound. The Sommerfeld coefficient determined for $T > T_C$, $\gamma_P = 650$ mJ/mol Sm K^2, is large and the Wilson-Sommerfeld ratio is calculated to be 0.9 - 1.1 depending on the experimental values used to calculated it. These properties of $Sm_2Ni_{12}P_7$ are comparable to those of the isostructural compound $Sm_2Fe_{12}P_7$; [19] for example, both compounds exhibit a large Sommerfeld coefficient value ($\gamma \simeq 650$ mJ/mol Sm K^2 and $\gamma \simeq 450$ mJ/mol Sm K^2 for T = Ni and T = Pd, respectively) and ferromagnetic transitions at $T_C \simeq 5$ K and $T_C \simeq 6.3$ K, respectively. Furthermore, the ferromagnetic order that develops in each compound is associated with itinerant electron states. On the other hand, a single magnetic phase transition is observed in $Sm_2Ni_{12}P_7$ while at least three distinct magnetic phases were observed in $Sm_2Fe_{12}P_7$. Our results for $Sm_2Ni_{12}P_7$, which are quite similar to those reported for the isostructural HF ferromagnet $Sm_2Fe_{12}P_7$, suggest that $Sm_2Ni_{12}P_7$ should be added to the exclusive list of Sm-based HF ferromagnets.

Acknowledgements

A portion of the text and data presented in Chapter 2 are reprints of material that appears in "Itinerant ferromagnetism in noncentrosymmetric heavy-fermion compound $Sm_2Ni_{12}P_7$" S. Jang, B. D. White, D. Yazici, C. A. McElroy, Young H. Kang, and M. B. Maple (in preparation). The dissertation author was the first author of the article.

Bibliography

[1] H. N. Andersen and H. Smith, Phys. Rev. B **19**, 384 (1979).

[2] M.B. Fontes, J.C. Trochez, S.L. Bud'ko, D.R. Sanchez, E.M. Baggio-Saitovitch, and M.A. Conti-nentino, Phys. Rev. B **60**, 6781 (1999).

[3] A. Menth, E. Buehler and T.H. Geballe, Phys. Rev. Lett. **22**, 295 (1969).

[4] D.J. Kim, S. Thomas, T. Grant, J. Botimer, Z. Fisk and J. Xia, Sci. Rep. **3**, 3150 (2013).

[5] S. Bakanowski, J. Crow and T. Mihalisin, Solid State Commun. **22**, 241 (1977).

[6] L.D. Long, R. McCallum, W. Fertig, M.B. Maple and J. Huber, Solid State Commun. **22**, 245 (1977).

[7] M.B. Maple, Z. Henkie, W. Yuhasz, P.C. Ho, T. Yanagisawa, T. Sayles, N.P. Butch, J.R. Jeeries, and A. Pietraszko, J. Magn. Magn. Mater. **310**, 182 (2007).

[8] H. Sato, D. Kikuchi, K. Tanaka, H. Aoki, K. Kuwahara, Y. Aoki, M. Kohgi, H. Sugawara and K. Iwasa, J. Magn. Magn. Mater.**310**, 188 (2007).

[9] C. Sekine, T. Uchiumi, I. Shirotani and T. Yagi Science and Technology of High Pressure, Universities Press, Hyderabad, (2000).

[10] M. Yoshizawa, Y. Nakanishi, M. Oikawa, C. Sekine, I. Shirotani, S.R. Saha, H. Sugawara and H. Sato, J. Phys. Soc. Jpn. **74**, 2141(2005).

[11] S. Sanada, Y. Aoki, H. Aoki, A. Tsuchiya, D. Kikuchi, H. Sugawara and H. Sato, J. Phys. Soc. Jpn. **74**, 246 (2005).

[12] W.M. Yuhasz, N.A. Frederick, P.C. Ho, N.P. Butch, B.J. Taylor, T.A. Sayles, M.B. Maple, J.B. Betts, A.H. Lacerda, P. Rogl and G. Giester, Phys. Rev. B **71**, 104402 (2005).

[13] Y.M. Prots and W. Jeitschko, Inorg. Chem.**37**, 5431 (1998).

[14] W. Jeitschko, D.J. Braun, R.H. Ashcraft and R. Marchand, J. Solid State Chem. **25**, 209 (1978).

[15] W. Jeitschko and B. Jaberg, J. Phys. Chem. Solids **54**, 1527 (1993).

[16] R.E. Baumbach, J.J. Hamlin, L. Shu, D.A. Zocco, J.R. O'Brien, P.C. Ho and M.B. Maple, Phys. Rev.Lett. **106403**, 209 (2010).

[17] R.E. Baumbach, J.J. Hamlin, M. Janoschek, I.K. Lum and M.B. Maple, J. Phys.: Condens. Matter **23**, 094222 (2011).

[18] S. Jang, B.D. White, P.C. Ho, N. Kanchanavatee, M. Janoschek, J.J. Hamlin and M.B. Maple, J. Phys.: Condens. Matter**42**, 425601 (2014).

[19] M. Janoschek, R.E. Baumbach, J.J. Hamlin, I.K. Lum and M.B. Maple, J. Phys.: Condens. Matter **23**, 094221 (2011).

[20] T. Nakano, K. Tsuchiya, A. Ohashi, T. Nashimoto, H. Ono, N. Takeda and N. Shirakawa, J. Phys. Soc. Jpn. **81**, 074601 (2012).

[21] S. Jang, B.D. White, P.C. Ho, N. Kanchanavatee, M. Janoschek, J.J. Hamlin and M.B. Maple, J. Phys.: Condens. Matter**42**, 425601 (2014).

[22] N. Takeda and M. Ishikawa, Physica B **329**, 460 (2013).

[23] S. Ramakrishnan, K. Ghosh, A.D. Chinchure, V.R. Marathe and G. Chandra, Phys. Rev. B **52**, 6784 (1995).

[24] H.M. Rietvelt, J. Appl. Crystallogr. **2**, 65 (1969).

[25] A.C. Larson and R.B. Von Dreele, Los Alamos National Lavoratory Report LAVR (2000).

[26] D. Wagner Introduction to the Theory of Magnetism, Oxford: Pergamon (1972).

[27] H.C. Hamaker, L.D. Woolf, H.B. MacKay, Z. Fisk and M.B. Maple, Solid State Commun. **32**, 289 (1979).

[28] J.H. Van Vleck The Theory of Electric and Magnetic Susceptibilities, Oxford University Press, London (1932).

[29] D. Yazici, B.D. White, P.C. Ho, N. Kanchanavatee, K. Huang, A.J. Frieman, A.S. Wong, V.W. Burnett, N.R. Dilley and M.B. Maple, Phys. Rev. B **90**, 144406 (2014).

[30] P. Rhodes and E.P. Wholfarth, Proc. R. Soc. A **247**, 273 (1963).

[31] S. Foner, E.J. McNiff and V. Sadagopan, Phys. Rev. Lett. **19**, 1233 (1967).

[32] F.R. Boerde , C.J. Schinkel, J. Bieserbos and S. Proost, J. Appl. Phys. **40**, 9017 (1989).

[33] G. Gruner and A. Zettl, Phys. Rep.**117**, 119 (1985).

[34] M.B. Maple, R.E. Baumbach, N.P. Butch, J.J. Hamlin and M. Janoschek, J. Low Temp. Phys. **161**, 4 (2010).

[35] E.C. Stoner and E.P. Wohlfarth, Phil. Trans. Royal Soc. London **599**, 240 (1948).

[36] A. Bohm, R. Caspary, U. Habel, L. Pawlak, A. Zuber, F. Steglich and A. Loidl, J. Magn. Magn. Mater. **76**, 150 (1988).

[37] P. Gegenwart, J. Custers, Y. Tokiwa, C. Geibel and F. Steglich, Phys. Rev. Lett. **94**, 076402 (2005).

[38] Z. Fisk, H.R. Ott and G. Aeppli, Jpn. J. Appl. Phys. **62**, 1882 (1987).

Chapter V

Synthesis and characterization of the $Zr_2Fe_{12}P_7$-type compound $Hf_2Fe_{12}P_7$

V.A Introduction

A relatively high incidence of interesting properties have recently been reported for members of the so-called "2-12-7" family of non-centrosymmetric compounds, [1, 2, 3, 4, 5] suggesting that this family of materials may represent a largely unexplored reservoir of strongly correlated electron phenomena. Several members of the 2-12-7 family have yet to be subjected to comprehensive characterization of basic transport, thermal, and magnetic properties. The magnetic behaviors of these compounds with generic chemical formula $R_2T_{12}P_7$ are quite variable depending on the ions that occupy the R and T sites. For example, 2-12-7 compounds are magnetic when T = Co (usually ordering ferromagnetically near 140 K), but tend to be non-magnetic when occupied by T = Mn, Fe, or Ni. [6, 7] The R site can be occupied by almost all of the rare earths as well as some alkali metal, alkaline earth, and group 4 elements.

We have recently embarked on a systematic search of 2-12-7 materi-

als that are expected to be non-magnetic with the hope that one of these non-centrosymmetric compounds might display superconductivity. In the course of these studies, we have synthesized a new 2-12-7 compound, $Hf_2Fe_{12}P_7$, which was also reported by Jeitschko *et al.*. [8] This compound exhibits a nearly linear dependence of the electrical resistivity on temperature, which motivated us to carry out further measurements.

V.B Experimental details

Polycrystalline samples of $Hf_2Fe_{12}P_7$ were prepared by solid state reaction. Hafnium chunks, iron powder, and pre-reacted FeP were weighed and mixed in the stoichiometric ratio. A total mass of 0.5 g of sample was sealed in a quartz tube under vacuum. The first heating cycle consisted of an initial ramp at 10-20 °C/hr up to 1000 °C for 72 hours. For the second heating cycle, the sample was ground to a fine powder and cold pressed into a pellet. The pellet was sealed in a quartz tube under vacuum, heated at a rate of 20-50 °C/hr to 1000 °C, and held at this temperature for 24 hours. Finally, the pellet was re-ground and pressed into a pellet for a third firing. The heating schedule for the third firing consisted of an initial ramp rate of 100 °C/hr to 1135 °C, with a dwell time of 72 hours. To investigate the magnetic behavior of possible impurity phase Fe_2P, we also prepared this compound in polycrystalline form by solid state reaction. Iron and phosphorus powders were weighed and mixed in the stoichiometric ratio. They were well mixed, pressed into pellets, encapsulated in evacuated quartz tubes, and annealed at 1000 °C for 48 hours. This process was repeated an additional time to promote homogeneity of the sample.

X-ray powder diffraction measurements were made using a Bruker D8 x-ray diffractometer utilizing copper K_α radiation. The resulting powder diffraction pattern was fit by means of a Rietveld analysis [9] implemented in the program suite GSAS+EXPGUI. [10] The magnetization was measured from room temperature

down to ~ 2 K and in magnetic fields H up to 7 T using a Quantum Design (QD) Magnetic Property Measurement System (MPMS). Specific heat measurements in the temperature range $T \sim 2 - 50$ K were carried out with a QD Physical Property Measurement System (PPMS) Dynacool, in magnetic fields $H = 0$ - 9 T. Measurements of the electrical resistivity were performed using a standard four-wire technique down to ~ 2 K in a home-built ^{4}He system, while measurements down to ~ 50 mK were made in an Oxford Instruments Kelvinox ^{3}He-^{4}He dilution refrigerator. At the lowest temperatures, the electrical resistivity measurements were repeated using several different excitation currents in order to ensure that there was no spurious heating of the sample.

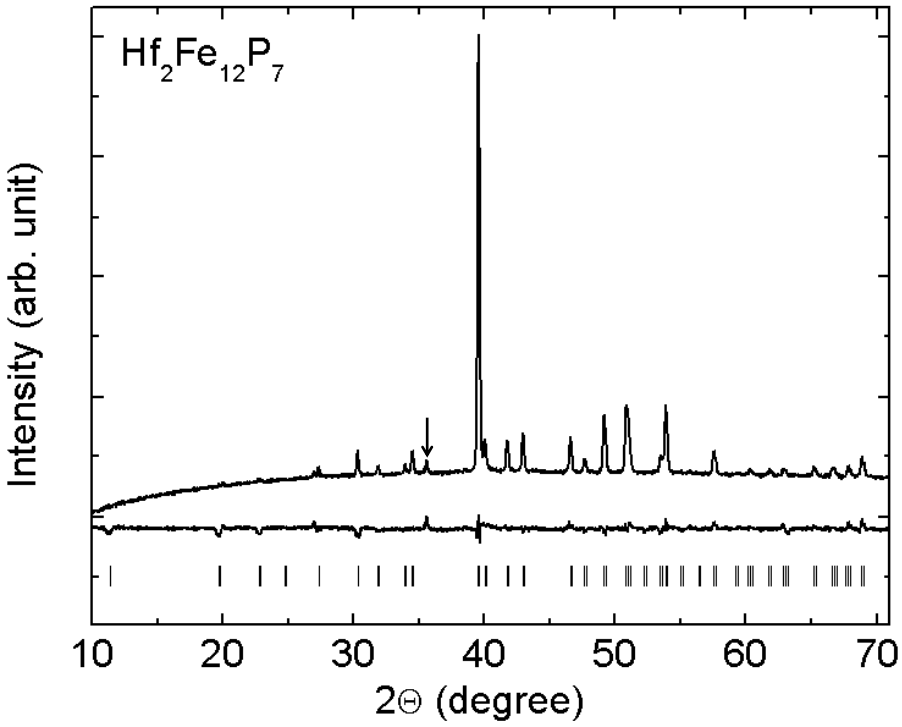

Figure V.1: Powder x-ray diffraction data and residuals of the Rietveld refinement fit. Vertical tick marks indicate the locations of expected Bragg reflections. The space group is $P\overline{6}$ with lattice constants of $a = 9.023$ Å and $c = 3.580$ Å. The arrow indicates a peak that may be related to the presence of a small amount of an impurity phase.

V.C Results and discussion

Figure 1 shows an analysis of the x-ray diffraction measurements. We present the residuals of the Rietveld refinement instead of the Rietveld refinement fit in order to show details of the measured data, which confirm the $Zr_2Fe_{12}P_7$-type crystal structure (space group $P\overline{6}$) with lattice constants $a = 9.023$ Å and $c = 3.580$ Å. These lattice constants are similar to those recently reported by Jeitschko *et al.*. [8] Though many 2-12-7 polycrystalline samples have been reported to contain substantial impurities such as oxides [12] or iron phosphorus compounds, [11] the results presented in Figure 1 indicate that the sample is nearly single phase. A small Bragg reflection near 36 degrees could be from either Fe_2P or HfO.

Isothermal magnetization M vs. magnetic field H measurements for $Hf_2Fe_{12}P_7$ at various temperatures are plotted in Figure 2(a). At and above 25 K, the curves are roughly linear with insignificant negative curvature at low magnetic fields. This curvature might be related with the Fe_2P impurity phase. By extrapolating the high-field slope of the magnetization curve at 100 K back to $H = 0$ T, the saturation moment μ_{sat} was determined to be $\sim$0.002 μ_B/Fe which suggests that the compound has $\sim$0.04 % of Fe_2P inclusions. At lower temperatures, the curves appear to be composed of two parts: a linear component and a saturating, Brillouin function-like contribution. It is possible that the saturating contribution is related to the presence of a small amount of another iron-containing paramagnetic impurity phase. In an effort to extract the intrinsic magnetic behavior of $Hf_2Fe_{12}P_7$, we have attempted to estimate the contribution from a possible paramagnetic impurity phase using a method similar to that previously applied to the analysis of the magnetic properties of $Y_{0.8}U_{0.2}Pd_3$. [13] The data measured at 2 K were chosen to estimate the paramagnetic impurity contribution, since these data exhibit the most pronounced non-linearity compared to the other data. Figure 2(b) shows an analysis of the magnetization data measured at 2 K, where the data are modeled as the sum of an intrinsic contribution $M_{int} = \chi_{int}H$, which is

linear in H with an intrinsic magnetic susceptibility, $(M/H)_{int}$, and a Brillouin-like impurity contribution $M_{imp} = M_0 B_J = n_{imp} M_s B_J$, where M_s is the saturation magnetization. The Brillouin function, B_J, is given by the following equation:

$$B_J(y) = \frac{2J+1}{2J} \coth\left(\frac{2J+1}{2J} y\right) - \frac{1}{2J} \coth\left(\frac{y}{2J}\right), \tag{V.1}$$

where

$$y = \frac{g_J J}{k_B T} H. \tag{V.2}$$

As H/T becomes large, the impurity contribution saturates to a value of M_0, which can be expressed

$$M_0 = n_{imp} g_J \mu_B J, \tag{V.3}$$

where g_J is the Landé g-factor and n_{imp} represents the number of ions which collectively produce the impurity contribution. As shown in Figure 2(b), the $M(H, T = 2\text{ K})$ data can be fitted very well with the sum of an intrinsic linear contribution and a $M_0 B_J$ term with total angular momentum $J = \frac{5}{2}$. The fit is shown as a solid line and the individual components are also plotted in Figure 2(b). In general, J is the sum of the orbital angular momentum L and the spin angular momentum S; however, since L is quenched in the case of Fe, $J = S$. Since the concentration of Fe_2P determined by extrapolating the high-field slope of the magnetization curve at 100 K back to $H = 0$ T is very small, $\sim$0.04 %, it was ignored from the impurity analysis described above. On the other hand, the behavior of M vs. H curves below $T = 25$ K might also be related with short-range magnetic correlations below that temperature.

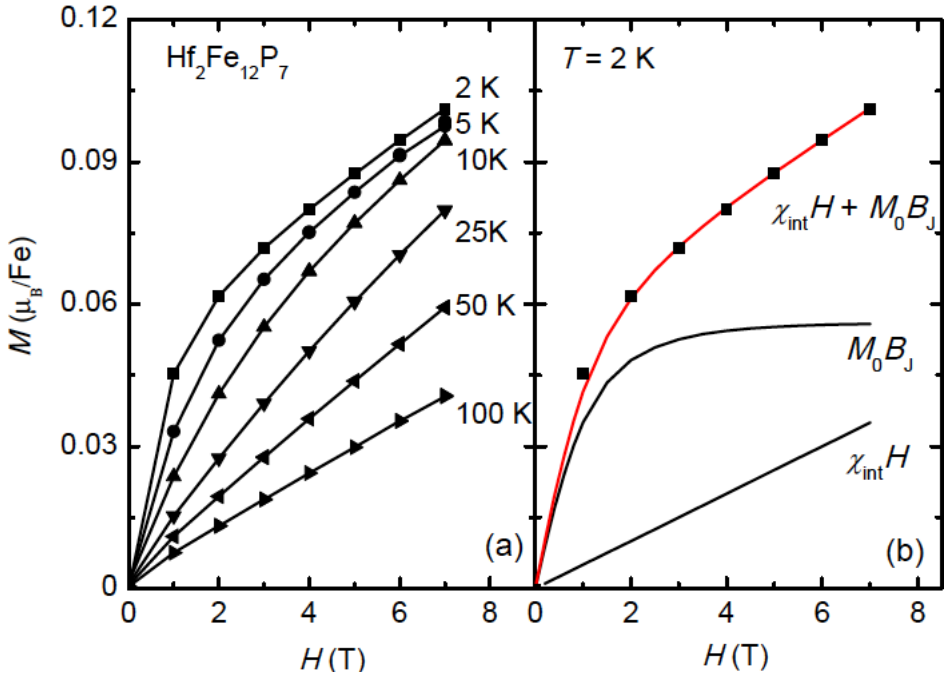

Figure V.2: (a) Isothermal magnetization, M, plotted vs. magnetic field, H, for several temperatures. (b) The filled squares indicate measured data, while the red solid line represents a fit to the data which assumes M is composed of the sum of linear $M_{int} = \chi_{int}H$ and nonlinear $M_{imp} = M_0 B_J$ (Brillouin function) contributions. These contributions are also plotted in the figure.

Measurements of magnetization in an applied magnetic field of $H = 0.5$ T, M/H, as a function of temperature, T, are presented in Figure 3(a) where the filled circles indicate the measured M/H. H/M is plotted in Figure 3(b), where it is again represented as filled circles. The inset of Figure 3(b) displays M/H vs. T data measured at $H = 0.1$ T of Fe_2P with a Curie temperature $T_C = 225$ K, which may be present as an impurity phase in $Hf_2Fe_{12}P_7$. H/M displays a broad feature near 150 - 250 K; these temperatures are comparable to the T_C of the ferromagnetic compound Fe_2P. Between 30 - 150 K, H/M is roughly linear. M/H in this temperature range can be described by a Curie-Weiss law, $M/H = C/(T - \theta)$, with a Curie-Weiss temperature θ = -46 K and an effective magnetic moment μ_{eff} that can be calculated from

$$C = N\frac{\mu_{eff}^2}{3k_B}. \tag{V.4}$$

Using Equation (4), we obtain $\mu_{eff} = 2.3\ \mu_B$/Fe. The value of μ_{eff} is close to $2.2\mu_B$/Fe, which is typically observed in Fe-based compounds. [**?**] The relatively large, negative Curie-Weiss temperature is probably related to antiferromagnetic correlations rather than being associated with antiferromagnetic ordering.

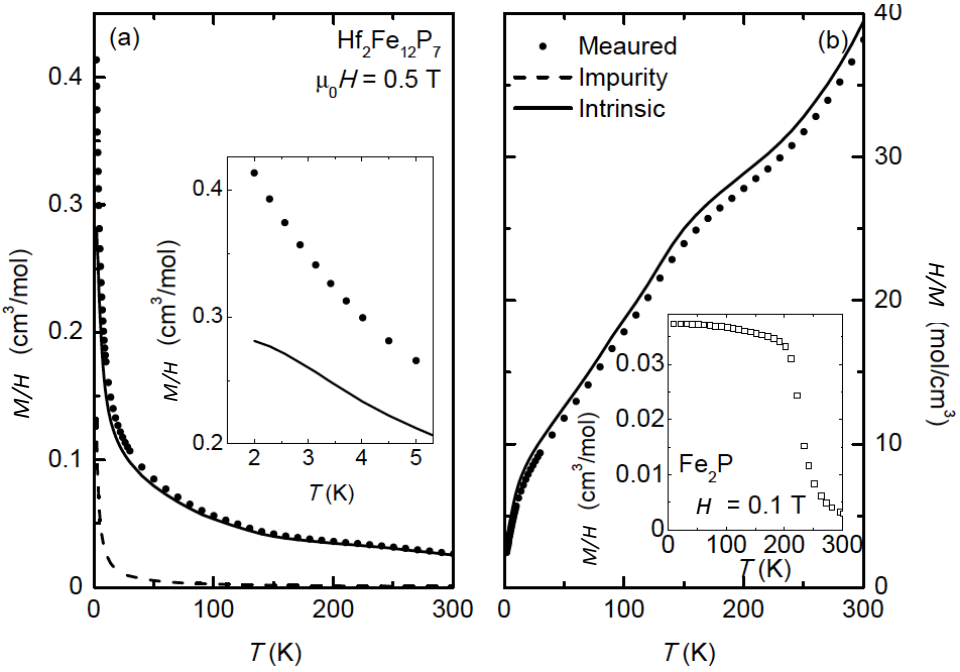

Figure V.3: (a) Magnetization in an applied magnetic field of $H = 0.5$ T, M/H as a function of temperature T for $Hf_2Fe_{12}P_7$ (filled circles). The inset shows the estimated intrinsic M/H at low temperature. The impurity contribution, estimated as described in the text, is indicated by the dashed line. The solid line represents the estimated intrinsic contribution to M/H after subtracting the impurity contribution from the measured data. (b) H/M as a function of temperature (filled circles). The inset presents M/H as a function of temperature for Fe_2P measured in an applied magnetic field of $H = 0.1$ T.

As we have noted, the measured data in Figure 3 include an impurity contribution $(M/H)_{imp}$. The impurity contribution $(M/H)_{imp}$ can be estimated by using the results from the analysis we conducted on M vs. H data measured at 2 K. The result is shown in Figure 3(a). We have calculated the Curie constant associated with the impurity contribution,

$$C_{imp} = N_{imp}\frac{\mu_{eff}^2}{3k_B}, \tag{V.5}$$

where

$$\mu_{eff} = g_J\mu_B\sqrt{J(J+1)}. \tag{V.6}$$

If we continue to assume the impurities are Fe-based, then $J = \frac{5}{2}$ and $g_J = 2$ so that $\mu_{eff} = \sqrt{35}\mu_B$ per impurity ion. Since $M_0 = 4.98\ \mu_B$/Fe, the impurity concentration n_{imp} is determined by Equation (3) ($n_{imp} = 0.01$). We can then calculate C_{imp} and the intrinsic magnetic susceptibility $(M/H)_{int}$ can be estimated. After subtracting $(M/H)_{imp}$ from the measured magnetic susceptibility $(M/H)_{meas}$, the intrinsic magnetic susceptibility $(M/H)_{int}$ saturates towards a temperature independent behavior at low temperature (see inset of Figure 3(a)). Estimating the intrinsic effective magnetic moment $\mu_{eff,int}$ from the magnetic susceptibility with the impurity contribution subtracted results in the value $\mu_{eff,int} \approx 2.3\ \mu_B$/Fe which is identical to the result we obtained without subtracting the impurity contribution. This result suggests that such a small amount of impurity contribution, $n_{imp} = 0.01$, does not effect the magnetic susceptibility at high temperatures. This result strengthens the possibility of short-range magnetic correlations below $T =$ 25 K. However, the behavior of M/H is very sensitive to the magnitude of the impurity contribution at low temperature as indicated in the inset of Figure 3(a).

Specific heat, C, divided by temperature, T, data, measured in magnetic fields of $H = 0$ and 9 T, are shown in Figure 4(a) for the temperature range T = 2 - 30 K. The specific heat well below the Debye temperature, Θ_D, can be approximated by $C(T) = \gamma T + \beta T^3$, where γ represents the electronic specific heat

coefficient, and β characterizes the lattice contribution. The values of β and γ can be obtained from the slope and intercept, respectively, of a linear fit to a plot of C/T vs. T^2 at low temperatures. The fit is shown in Figure 4(c), where the data below $T^2 = 400$ K^2 ($T = 20$ K) have been omitted from the fit due to the presence of a broad hump, and yields $\beta = 0.53$ mJ/mol-K^4, corresponding to a Debye temperature $\Theta_D = 414$ K, and electronic specific heat coefficients $\gamma = 92.5$ mJ/mol-K^2-Hf and $\gamma = 88.5$ mJ/mol-K^2-Hf for $H = 0$ T and $H = 9$ T, respectively. These values of γ are very close to the values found for $Th_2Fe_{12}P_7$ ($\gamma \sim 95$mJ/mol-K^2, [**?**]) suggesting that the Hf d-electrons do not contribute significantly to the density of electronic states at the Fermi level.

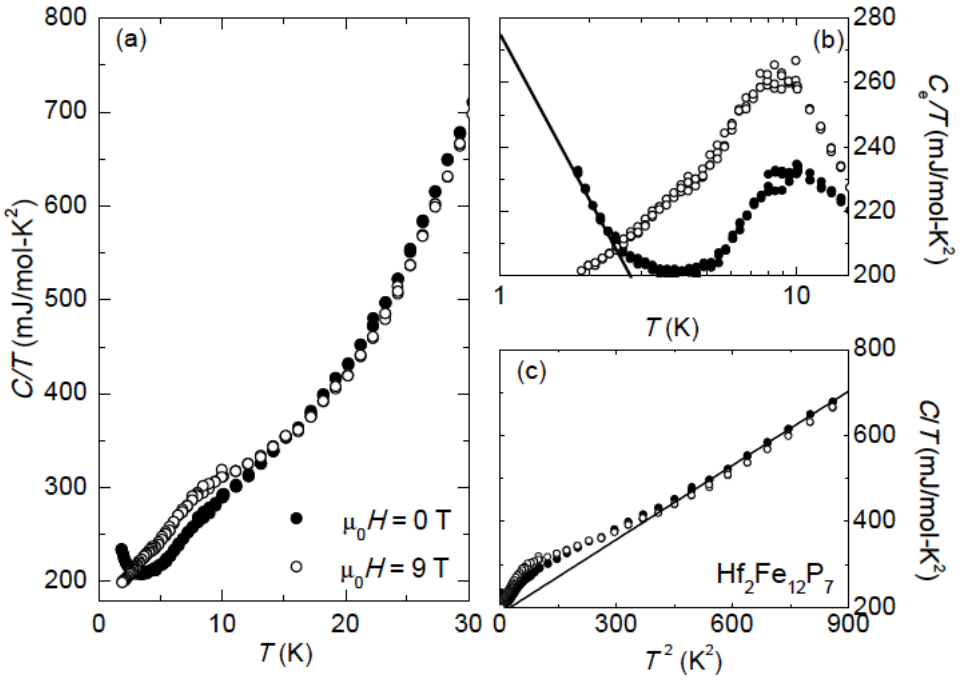

Figure V.4: (a) Specific heat C divided by temperature T measured in magnetic fields of $H = 0$ T (filled circles) and $H = 9$ T (open circles). (b) Electronic contribution to the specific heat, C_e, divided by T vs. ln$T$ where the solid line represents a fit of the expression $C_e(T)/T = a(\ln(T_0/T))$ to the data at low temperature. (c) C/T data are plotted versus T^2. The linear fit provides an estimate of the electronic specific heat coefficient, γ, and the coefficient, β, as described in the text.

There is a broad hump in the $C(T)/T$ data near $T \sim 10$ K, as shown in Figure 4(a). Displayed in the Figure 4(b) are plots of $C_e(T)/T$ vs. lnT, where C_e is the electronic contribution to the specific heat, obtained by subtracting the lattice contribution (βT^3) from $C(T)$. A peak clearly emerges near 10 K in the C_e/T data. This peak could potentially be related to magnetic order. Small entropy changes near $T \sim 10$ K of $\Delta S \sim 1.76$ J/mol K and 1.97 J/mol K, suggest that the peak might be related to short range magnetic order which supports the results obtained from M/H vs. T and the character of M vs. H below 25 K. Below 4 K, the C/T data exhibit a distinct upturn that is suppressed by the application of magnetic field as shown in Figure 4(b). There are at least three possible explanations for the low T upturn in $C(T)/T$ at $H = 0$ T: (1) It represents the high temperature tail of a nuclear Schottky anomaly, which is highly improbable because the feature is suppressed by applied magnetic field and the $C(T)$ data below 4 K can not be described by an expression of the form $C(T) = AT^{-2}$; (2) the feature is related to the onset of magnetic order; (3) the upturn derives from the onset of non-Fermi liquid (NFL) behavior, which can be characterized by a $C/T \sim \ln(T_0/T)$ temperature dependence. [15, 16] Figure 4(b) presents a reasonable fit to the data of the expression $C_e(T)/T = a(\ln(T_0/T))$, where $a = 78.9$ mJ/mol-K^2 and $T_0 = 35.9$ K. The suppression of the upturn with H suggests that the NFL behavior is suppressed by an applied field. Several origins of NFL behavior are known, e.g., a magnetic instability leading to a quantum phase transition, or single-ion effects as the multichannel Kondo effect, or a distribution of Kondo temperatures. [15, 16] However, none of these phenomena seem to be relevant in $Hf_2Fe_{12}P_7$. An applied magnetic field would also tend to suppress antiferromagnetic order, so this observation is consistent with that scenario as well. A more definitive understanding of the origin of this upturn will require additional specific heat measurement to lower temperatures.

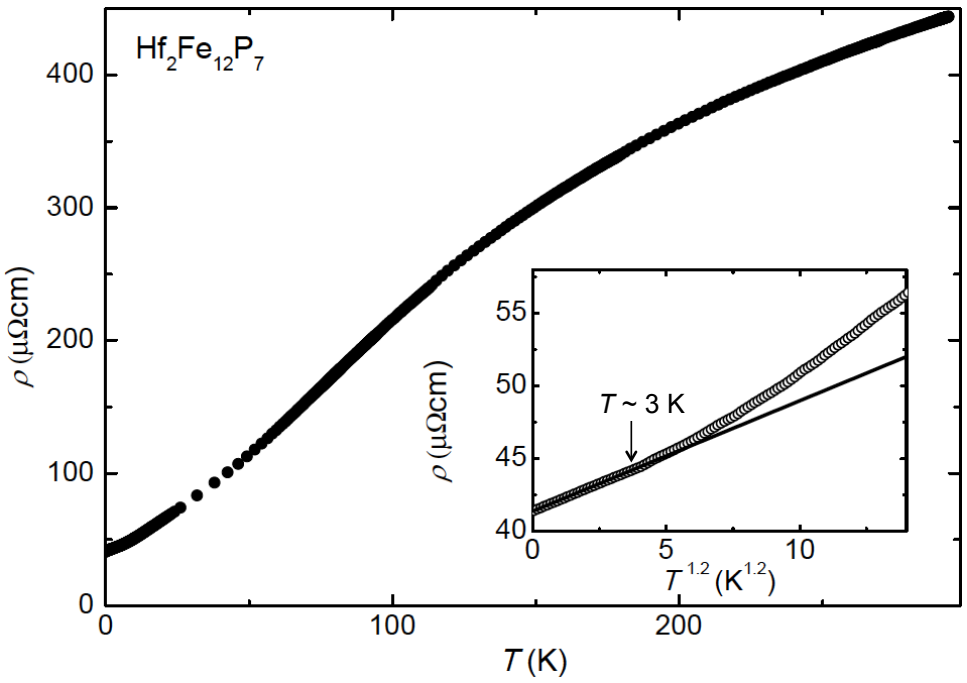

Figure V.5: Electrical resistivity ρ vs. temperature T. The inset shows low temperature ρ vs. $T^{1.2}$. The solid line emphasizes the temperature range over which the temperature dependence of ρ exhibits power law behavior with exponent 1.2.

The temperature dependence of the electrical resistivity, $\rho(T)$, is presented in Figure 5 for $T \sim 0.05$ - 300 K. From room temperature down to ~ 80 K, the electrical resistivity exhibits negative curvature, which may be due to $s-d$ scattering as described by Mott and Jones. [18] Interestingly, no anomaly in the resistivity is observed at low temperature, where analysis of the specific heat suggested the presence of a (possibly antiferromagnetic) phase transition. The inset of Figure 5 shows the $\rho(T)$ between 0.05 - 3 K is nearly a linear function of temperature. The electrical resistivity in this temperature range can be described by a power law of the form $\rho(T) = \rho_0 + AT^n$, where the best fit yields $\rho_0 \sim 41.6$ $\mu\Omega$cm, $A = 0.543$ $\mu\Omega\text{cm/K}^{1.2}$ and $n \sim 1.2$. An electrical resistivity with a power-law T dependence with an exponent close to 1 at low temperature is typically cited as evidence of NFL behavior. The electrical resistivity deviates from the nearly linear T-dependence at temperature above ~ 3 K, which is comparable to the temperature where the upturn in C/T begins. Despite the fact that none of the reported origins of NFL behavior appear to be relevant in $Hf_2Fe_{12}P_7$, [15, 16] the behavior of $\rho(T)$ between 0.05 - 3 K is consistent with NFL behavior.

V.D Summary

We have reported measurements of the electrical resistivity, magnetization, and specific heat in magnetic fields $H = 0$, 9 T and temperatures T down to 50 mK on polycrystalline samples of the compound $Hf_2Fe_{12}P_7$. The samples were found to contain a minor amount of secondary impurity phase as confirmed by measurements of x-ray diffraction and magnetization. $Hf_2Fe_{12}P_7$ exhibit a linear temperature dependence of electrical resistivity data at temperatures $0.05 < T < 3$ K, an upturn in specific heat data at $H = 0$ T with a $C/T \sim -\ln T$ temperature dependence, and possible short-range magnetic correlations according to the magnetization measurements. Fits to magnetization data at $T = 2$ K with a Brillouin function were used to estimate the paramagnetic impurities contribution that was

subtracted from the data to determine the intrinsic M/H of this compound.

Acknowledgements

A portion of the text and data presented in Chapter 3 are reprints of material that appears in "Synthesis and characterization of the $Zr_2Fe_{12}P_7$-type compound $Hf_2Fe_{12}P_7$" S. Jang, J. J. Hamlin, M. Janoschek, B. D. White, D. Yazici, and M. B. Maple (in preparation). The dissertation author was the first author of the article.

Bibliography

[1] W. Jeitschko, D. J. Braun, R. H. Ashcraft, and R. Marchand, J. Solid State Chem. **25**, 309 (1978).

[2] R. E. Baumbach, J. J. Hamlin, L. Shu, D. A. Zocco, J. R. O'Brien, P. C. Ho, and M. B. Maple, Phys. Rev. Lett. **105**, 106403 (2010).

[3] R. E. Baumbach, J. J. Hamlin, M. Janoschek, I. K. Lum, and M. B. Maple, Philos. Mag. **92**, 647 (2012).

[4] M. Janoschek, R. E. Baumbach, J. J. Hamlin, I. K. Lum, and M. B. Maple, J. Phys.: Condens. Mat. **23**, 094221 (2011).

[5] J. J. Hamlin, M. Janoschek, R. E. Baumbach, B. D. White, and M. B. Maple, J. Phys.: Condens. Mat. **23**, 094222 (2011).

[6] M. Reehuis and W. Jeitschko, J. Phys. Chem. Solids **50**, 563 (1989).

[7] M. Reehuis, N. Stüßer, A. Nientiedt, T. Ebel, W. Jeitschko, B. Ouladdiaf, and others, J. Magn. Magn. Mater. **177**, 805 (1998).

[8] W. Jeitschko, U. Meisen, and E. J. Reinbold, Z. Anorg. Allg. Chem. **638**, 770 (2012).

[9] H. M. Reitvelt, J. Appl. Cryst. **65**, 2 (1969).

[10] A. Larson and R. V. Dreele, Los Alamos National Laboratory Report, 86-748 (2000).

[11] D Bellavance, J Mikkelsen, and A Wold, Physica B **2**, 285 (1970).

[12] B. K. Cho, F. J. DiSalvo, J. S. Kim, G. R. Stewart, and S. L. Bud'ko, Physica B **253**, 40 (1998).

[13] H. G. Lukefahr, O. O. Bernal, D. E. MacLaughlin, C. L. Seaman, M. B. Maple, and B. Andraka, Phys. Rev. B **52**, 3038 (1995).

[14] S. Sinneman, R. J. Radwanski, J. J. M. Franse, D. B. de Mooij, and K. H. J. Buschow, J. Magn. Magn. Mater. **44**, 333 (1984).

[15] C. L. Seaman, M. B. Maple, B. W. Lee, S. Ghamaty, M. S. Torikachvili, J. -S. Kang, L. Z. Liu, J. W. Allen, and D. L. Cox, Phys. Rev. Lett. **67**, 2882 (1984).

[16] B. Andraka and A. M. Tsvelic, Phys. Rev. Lett. **67**, 2886 (1991).

[17] N. H. Andersen and H. Smith, Phys. Rev. B **19**, 384 (1979).

[18] N. F. Mott and H. Jones, The Theory of the Properties of Metals and Alloys (1958).

Chapter VI

Resolution of the discrepancy between the variation of the physical properties of $Ce_{1-x}Yb_xCoIn_5$ single crystals and thin films with Yb composition

VI.A Introduction

The unusual effect of Yb substituents compared to that of other lanthanide substituents on the normal and superconducting state properties of the heavy fermion compound $CeCoIn_5$ has attracted much recent interest. [1, 2, 3, 4, 5, 6, 7, 8, 9, 10, 11] Measurements of the electrical resistivity $\rho(T)$, magnetic susceptibility $\chi(T)$, specific heat $C(T)$, and tetragonal a- and c-lattice parameters as a function of x, performed on flux-grown bulk single crystal specimens in independent studies by Capan *et al.* [1] and Shu *et al.* [2], yielded results that are

in general agreement with one another. In the work of Shu *et al.* [2], the weak variations of the coherence temperature T^* and superconducting critical temperature T_c with Yb concentration x were attributed to stabilization of the correlated electron state in the $Ce_{1-x}Yb_xCoIn_5$ system over a large range of x. Based on the strong deviation of the tetragonal a- and c-lattice parameters and unit cell volume $V = a^2c$ as a function of x from Vegard's law (linear variation of a- and c-lattice parameters with x), [12] it was suggested [2] that the stability of the correlated electron state in $Ce_{1-x}Yb_xCoIn_5$ could be due to cooperative behavior of the Ce and Yb ions involving their unstable valences that can range from 3+ to 4+ in the case of Ce and 2+ to 3+ for Yb. Since the $4f$-electron states of the Ce and Yb ions are admixed with conduction electron states, they communicate with one another through the conduction electrons. It was reasoned that the Ce and Yb ions could then self-consistently adjust their valences so as to stabilize the heavy electron state over a large range of Yb concentrations x. However, spectroscopic measurements (EXAFS, XANES, and ARPES) by Booth *et al.* [3] and Dudy *et al.* [8] found that the valence of Ce remains close to 3+ for $0 \leq x \lesssim 1$, whereas the valence of Yb remains close to 2.3+ for $0.2 \lesssim x \leq 1$. These results are not consistent with the aforementioned proposal [2] that the Ce and Yb valences vary with Yb concentration. It is noteworthy that the experiments of Dudy *et al.* [8] revealed that Yb undergoes a valence transition from 3+ at $x \approx 0$ to ~2.3+ at $x \approx 0.2$. While there are issues of phase separation at values of x above ~0.8, [1, 2] we emphasize that the valence of the pure $YbCoIn_5$ end-member compound ($x = 1$) was found to be ~2.3+,[3, 8] which is important for the analysis presented herein.

Subsequent investigations of the $Ce_{1-x}Yb_xCoIn_5$ system revealed evidence for other electronic transitions at $x \sim 0.2$, including a reconstruction of the Fermi surface above $x \approx 0.2$, accompanied by a significant reduction in the quasiparticle effective mass [5], and suppression of the quantum critical field associated with the correlated heavy fermion state to 0 K at a quantum critical point (QCP) at $x \approx 0.2$. [7, 9] Surprisingly, these transitions have little effect on

the unconventional superconductivity and non-Fermi liquid (NFL) behavior. Measurements of T_c vs. x in the range $x = 0$ and $x = 0.7$ show that T_c decreases linearly with x from 2.3 K at $x = 0$ and extrapolates to 0 K at $x \approx 1$, with no features near $x = 0.2$. The NFL signatures in $\rho(T)$, $C(T)$, and $\chi(T)$ persist from 0 to $x \approx 0.8$ with an abrupt crossover to Fermi liquid (FL) behavior slightly above this value of x: [2, 9] this suggests that the NFL behavior could be associated with a new state of matter rather than being a consequence of the underlying quantum phase transition at $x \approx 0.2$ and opens up the possibility that some other type of electronic transition occurs near $x \approx 0.8$. [13] The region $0.8 \leq x \leq 1$ is currently being explored.

Measurements of electrical transport properties on $Ce_{1-x}Yb_xCoIn_5$ thin films revealed that the variation of the physical properties is much stronger than that observed in the $Ce_{1-x}Yb_xCoIn_5$ single crystals, but weaker than that which is found for other lanthanide substituents in $CeCoIn_5$ single crystals; [6] the rate of depression of T^* and T_c with Yb concentration for the thin films is about three times greater than that observed in the single crystals. In this paper, we describe an analysis we have performed on bulk single crystals of $Ce_{1-x}Yb_xCoIn_5$ that apparently resolves the discrepancy between the bulk single crystal and thin film experiments. The analysis involves the application of Vegard's law to estimate the actual composition $x_{\rm act}$ using the variation of the tetragonal a- and c-lattice parameters and the spectroscopically-determined valences of Ce and Yb as a function of nominal composition x in flux-grown $Ce_{1-x}Yb_xCoIn_5$ single crystals. The analysis is unusual, since we are using the known valences of Ce and Yb as a function of x to determine the actual Yb concentration $x_{\rm act}$ (assuming that all of the lanthanide sites in the compounds are occupied by Ce or Yb ions; *i.e.*, no lanthanide vacancies). In the usual Vegard's law analysis, the lanthanide sites are occupied by lanthanide ions according to their nominal concentrations, and the deviations of the lattice parameters from Vegard's law are used to estimate the valence of one of the lanthanide ions. [15, 16] Direct support for the Vegard's law analysis

is provided by energy dispersive x-ray spectroscopy (EDS), wavelength dispersive x-ray spectroscopy (WDS), and transmission x-ray absorption edge spectroscopy (TXAS) measurements on selected single crystals, which are reported herein. Although XAS usually refers to both fluorescence and transmission data, only the step height in transmission data is proportional to the number of atoms within the x-ray beam and we use the designation TXAS to highlight this difference. The Vegard's law analysis of the a- and c-lattice parameters indicates that the actual Yb composition of the single crystals is about 1/3 of the nominal composition in the range $0 \leq x \lesssim 0.5$, resolving the discrepancy between experiments on $Ce_{1-x}Yb_xCoIn_5$ single crystals and thin films. It is noteworthy that the actual composition of the $Ce_{1-x}Yb_xCoIn_5$ single crystals prepared from a molten indium flux is in registry with the nominal composition of the starting material contained in the molten flux, but is only about 1/3 of its value in the range $0 \leq x \lesssim 0.5$. The sharpness of the specific heat feature associated with the superconducting transition, [1, 2] which reflects the bulk behavior of the crystals, indicates that the $Ce_{1-x}Yb_xCoIn_5$ single crystals are homogeneous up to Yb nominal compositions of $x \sim 0.5$. As a result, all of the experiments on $Ce_{1-x}Yb_xCoIn_5$ single crystals that have been performed in the range $0 \leq x \lesssim 0.5$ are still valid but the actual Yb concentration is about 1/3 of the nominal concentration; *i.e.*, $x_{\rm act} \approx x/3$. At higher x, the Vegard's law analysis indicates that the ratio of $x_{\rm act}$ to x increases continuously with x to the value of 1 at $x = 1$, as it must for the pure $YbCoIn_5$ end member compound.

In the study by Shu *et al.*, [2] the samples selected for $\rho(T)$, $\chi(T)$ and $C(T)$ measurements had actual Yb compositions $x_{\rm act}$, as determined from EDS measurements, that were close to the nominal composition x. We have performed further EDS measurements on samples with the same values of x as those reported in the work of Shu *et al.* and found that the values of $x_{\rm act}$, inferred from EDS measurements, exhibit bimodal behavior in which $x_{\rm act} \approx x/3$ for some crystals, whereas $x_{\rm act} \approx x$ for other crystals, with large uncertainties in the values of $x_{\rm act}$.

A possible reason for this bimodal behavior of $x_{\rm act}$ may be that the single crystals have a bimodal Yb surface composition $x_{\rm act} \approx x/3$ and $x_{\rm act} \approx x$ and a bulk composition $x_{\rm act} \approx x/3$. As we explain in the following, this result is consistent with an analysis based on the application of Vegard's law to the unit cell volume, V, vs. x data, where V was determined from powder x-ray diffraction measurements of the tetragonal a- and c-lattice parameters (*i.e.*, $V = a^2c$).

VI.B Experimental details

Single crystals of $Ce_{1-x}Yb_xCoIn_5$ were grown using a molten indium flux method in alumina crucibles, as described previously [17]. Powder x-ray diffraction measurements, performed at room temperature, reveal that the $Ce_{1-x}Yb_xCoIn_5$ single crystals form in the tetragonal $HoCoGa_5$ structure. The tetragonal a- and c-lattice parameters were determined from a least-squares fit of the peak positions in the x-ray powder diffraction pattern using GSAS and EXPGUI, [**?**, 14] It should be noted that our lattice parameter values are in good agreement with those of Capan *et al.*; [1] however, in the analysis described below, we use the data for the a- and c-lattice parameters of Capan *et al.*, since the scatter in their data is smaller than in ours.

Energy dispersive x-ray spectroscopy (EDS) measurements were carried out at the University of California, San Diego on various samples that have been prepared for the experiments reported in Refs. [2, 4, 7, 8, 9, 10, 11], the wavelength dispersive x-ray spectroscopy (WDS) measurements were performed at Iowa State University, Ames National Laboratory, on samples studied in the penetration depth experiments and on several other samples with different Yb concentrations, [10] while the transmission x-ray absorption edge spectroscopy (TXAS) measurements were performed at the Stanford Synchrotron Radiation Laboratory on samples specifically prepared for the TXAS measurements. The EDS, WDS, and TXAS measurements are discussed in more detail below.

Measurements of electrical resistivity were performed down to ∼1.1 K in a ^{4}He Dewar using a Linear Research LR700 ac resistance bridge. Four wires were adhered to gold-sputtered contact pads on each single crystal using silver epoxy. Typical contact resistances of 100 mΩ or less were measured at room temperature by comparing two- and four-wire resistance measurements.

VI.C Results and discussion

Before determining the actual Yb concentration $x_{\rm act}$ in single-crystalline samples of $Ce_{1-x}Yb_xCoIn_5$, we demonstrate that Yb is incorporated into the single crystals systematically and in registry with the nominal Yb concentration x. In Fig. 1(a), the inverse of the residual resistivity ratio (RRR) is plotted vs x. We calculated the inverse of the RRR from electrical resistivity $\rho(T)$ measurements (not shown) on several single crystals as $\rho_0/\rho(300\ {\rm K})$, where ρ_0 is the residual electrical resistivity. The data are plotted this way because $\rho_0/\rho(300\ {\rm K})$ does not suffer from errors associated with measuring the geometrical factor. It is clear that the data in Fig. 1(a) are linear up to $x = 0.5$, convincingly demonstrating that Yb is incorporated into the crystal structure systematically (*i.e.*, temperature-independent impurity scattering characterized by ρ_0 increases relative to $\rho_0/\rho(300$ K) with increasing nominal Yb concentration x). We are also able to demonstrate that the variation of the physical properties of the $Ce_{1-x}Yb_xCoIn_5$ system is a systematic function of the RRR as seen in the plot of superconducting critical temperature T_c vs. RRR in Fig. 1(b). This result further emphasizes that the RRR values meaningfully characterize the level of disorder in the single crystals, and that $x_{\rm act}$ is in registry with x.

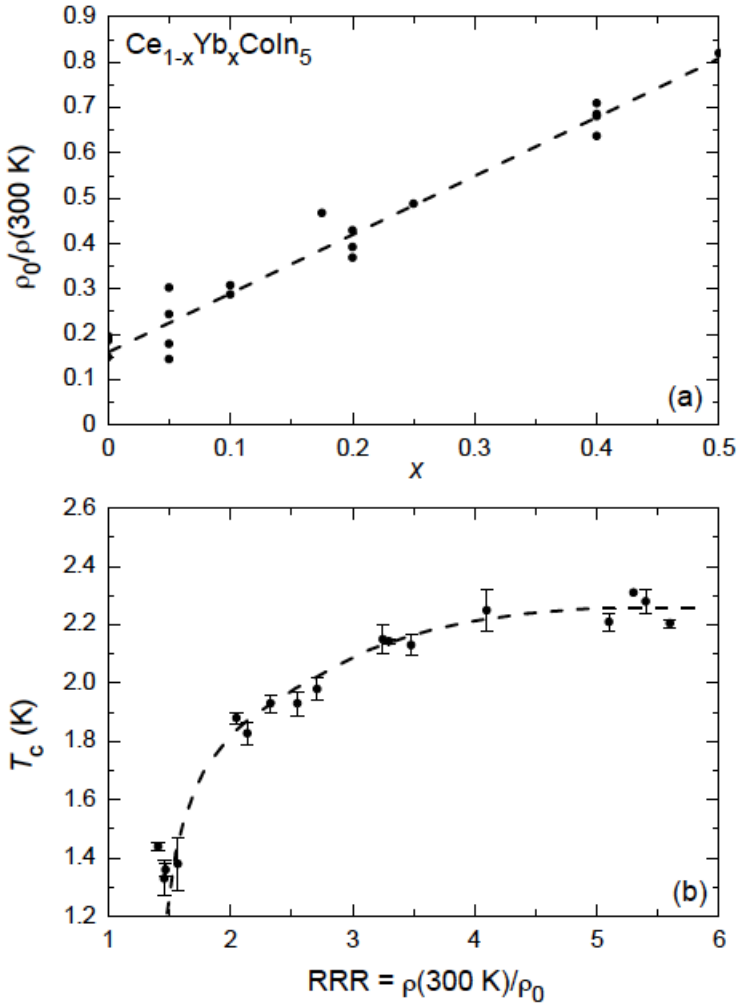

Figure VI.1: (a) Inverse of the residual resistivity ratio (RRR), calculated as $\rho_0/\rho(300\ \mathrm{K})$ from measurements of electrical resistivity on distinct samples, plotted vs.nominal Yb concentration x for the $Ce_{1-x}Yb_xCoIn_5$ system. The dashed line is a guide to the eye. (b) Superconducting critical temperature T_c plotted vs. RRR from the same measurements shown in panel (a). The dashed curve is a guide to the eye. Vertical bars characterize the width of the superconducting transitions and were calculated using the temperatures where $\rho(T)$ drops to 90% and 10% of its normal-state value just above T_c.

VI.C.1 Estimate of actual Yb concentration using Vegard's law

Vegard's law refers to the linear variation of the lattice parameters or unit cell volume when an element is substituted for another element in a compound for which the crystal structure does not change and the chemical composition is known. This relation is often used to estimate the valence of lanthanide ions, which have valence instabilities such as Ce, whose valence can range from 3+ to 4+, and Sm, Eu, Tm, and Yb, whose valence can range from 2+ to 3+ [15, 16]. In this work, we instead employ Vegard's law in a different manner to estimate the actual Yb concentration $x_{\rm act}$ in the $Ce_{1-x}Yb_xCoIn_5$ system using the valences of the Ce and Yb ions, derived from spectroscopic measurements, and the tetragonal a- and c-lattice parameters, determined from x-ray diffraction measurements on powdered $Ce_{1-x}Yb_xCoIn_5$ samples, as a function of nominal Yb concentration x. Since previous investigations have shown that the valence of Yb changes from 3+ to 2.3+ between $x = 0$ and $x = 0.2$ [8] and remains 2.3+ for all concentrations greater than $x = 0.2$ [3, 8], the unit cell volume $V = a^2c$ of $Ce_{1-x}Yb_xCoIn_5$ should be a linear function of x between 0.2 and 1.0, according to Vegard's law. We would expect a subtle non-linear variation of V with x for $x < 0.2$ as the Yb valence changes from 3+ to 2.3+ in the range $0 < x \leq 0.2$. In Fig. 2, we show a plot of the measured unit cell volume V vs. x, based on the x-ray diffraction measurements of a and c-lattice constants for $Ce_{1-x}Yb_xCoIn_5$ as a function of x, and a plot of V vs. x based on Vegard's law. The lattice parameter data of Capan *et al.* [1] were used since they show less scatter than the data of Shu *et al.* [2]. By adjusting the measured values of V to the Vegard's law curve (illustrated by the arrows in Fig. VI.2), we can estimate the actual concentration $x_{\rm act}$ of Yb. The values of $x_{\rm act}$ determined by means of this procedure are shown in the $x_{\rm act}$ vs. x plot in Fig. 3(b). For values of x below ∼0.5, the actual bulk Yb concentration $x_{\rm act}$ is about 1/3 of the nominal concentration x. For comparison, Fig. VI.3(a) shows $x_{\rm act}$ vs. x data based on EDS and PIXE measurements on flux grown $Ce_{1-x}Yb_xCoIn_5$ single crystals prepared at UC, Irvine and UC, San Diego. In Fig. 3(a), the $x_{\rm act}$

vs. x data are consistent with $x_{\mathrm{act}} \approx x/3$ for x values up to $x \approx 0.6$. Shown in Fig. 3(b) are measurements of the bulk concentration of Yb based on EDS, WDS, TXAS, described in the following, that are also seen to be consistent with $x_{\mathrm{act}} \approx x/3$ up to $x \approx 0.5$.

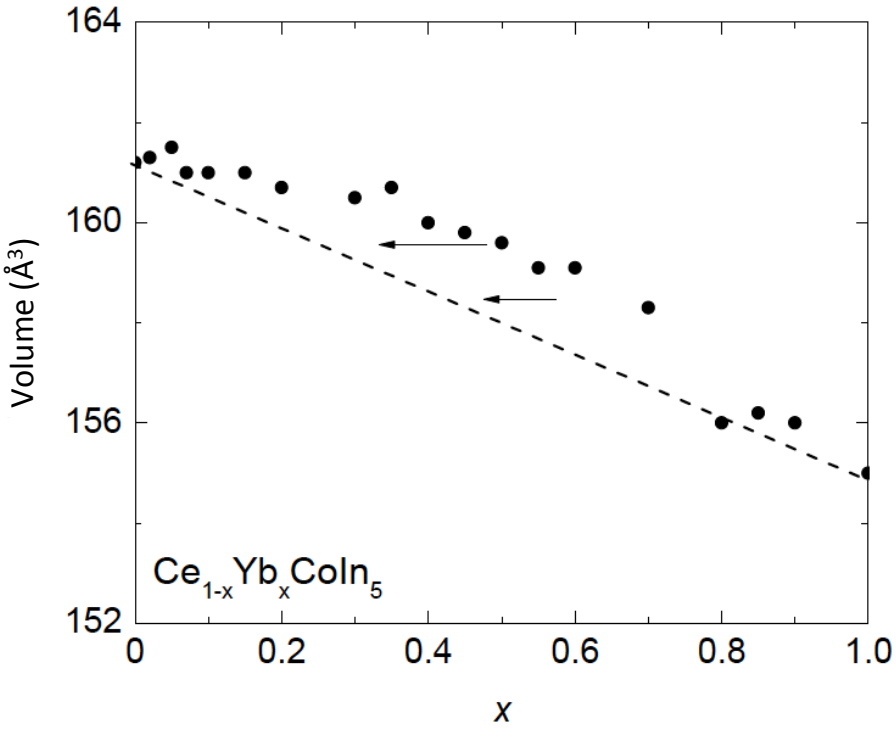

Figure VI.2: Unit cell volume V vs. nominal Yb concentration x for the system $Ce_{1-x}Yb_xCoIn_5$ (filled circles) based on the data of Capan *et al.* [1]. The dashed straight line represents Vegard's law between the unit cell volumes of the end member compounds $CeCoIn_5$, in which the Ce ion has a valence of 3+, and $YbCoIn_5$, in which the Yb ion has an intermediate valence of 2.3+. Since the Yb ion has a valence of 2.3+ in the range $0.2 \leq x \leq 1$, the unit cell volume V should conform to the dashed line in this range of x values, with small deviations in the range $0 < x < 0.2$ where the Yb ions undergo a valence transition between 3+ and 2.3+. The actual concentration of Yb, $x_{\rm act}$, can be estimated by displacing the observed $V(x)$ data (solid circles) to the left, as illustrated by the horizontal arrows, so that they lie on the linear Vegard's law relation (dashed black line).

VI.C.2 EDS, WDS, and TXAS measurements of the actual Yb concentration

The results of EDS measurements on selected $Ce_{1-x}Yb_xCoIn_5$ samples are shown in the $x_{\rm act}$ vs. x plot in Fig. 3(b). The method in which the data were taken is illustrated in Fig. VI.4, which shows photographs of several $Ce_{1-x}Yb_xCoIn_5$ samples with nominal Yb concentrations of $x = 0.175$ and 0.2, labeled with the letters A, B, C, and D, that have been affixed to conducting carbon tape for the EDS measurements. The EDS measurements were made on each of the samples at several different spots defined by the regions outlined by the black rectangles on the photographs of the crystals. The measured values of x, x_{meas}, for each of the regions are indicated in the lower panel of Fig. 4 for the crystals labeled A, B, C, and D for the two selected Yb compositions, where the dashed lines indicate the average value of all the data for each Yb nominal concentration. The average values of the measurements and the error derived from the standard deviation are plotted as $x_{\rm act}$ vs. x in Fig. 3(b).

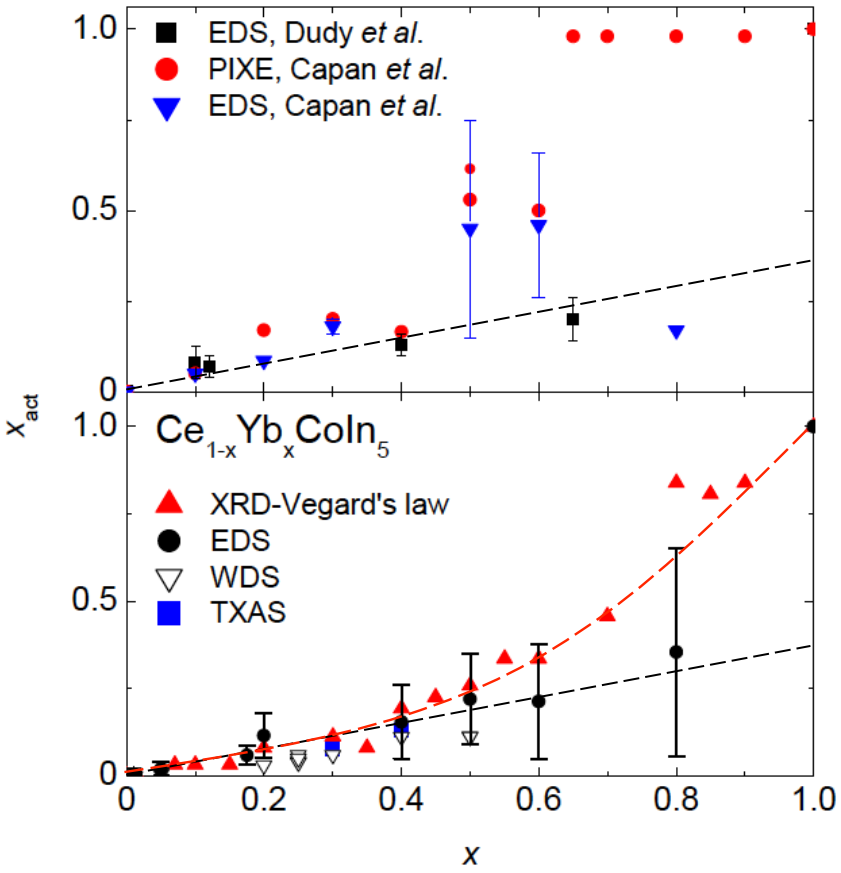

Figure VI.3: (a) Actual Yb concentration x_{act} vs. nominal Yb concentration x as obtained from EDS measurements reported by Dudy *et al.* [8] (solid black squares) and PIXE and EDS measurements reported by Capan *et al.* [1] (solid red circles and solid inverted blue triangles, respectively). (b) Actual Yb concentration x_{act} vs. nominal Yb concentration x based on: (1) Vegard's law analysis of $V(x)$ measurements (solid red triangles); (2) average value of the measured Yb concentration from several EDS measurements with error bars defined as the standard deviation (solid black circles); (3) WDS measurements (inverted unfilled triangles); (4) TXAS measurements (solid blue squares).

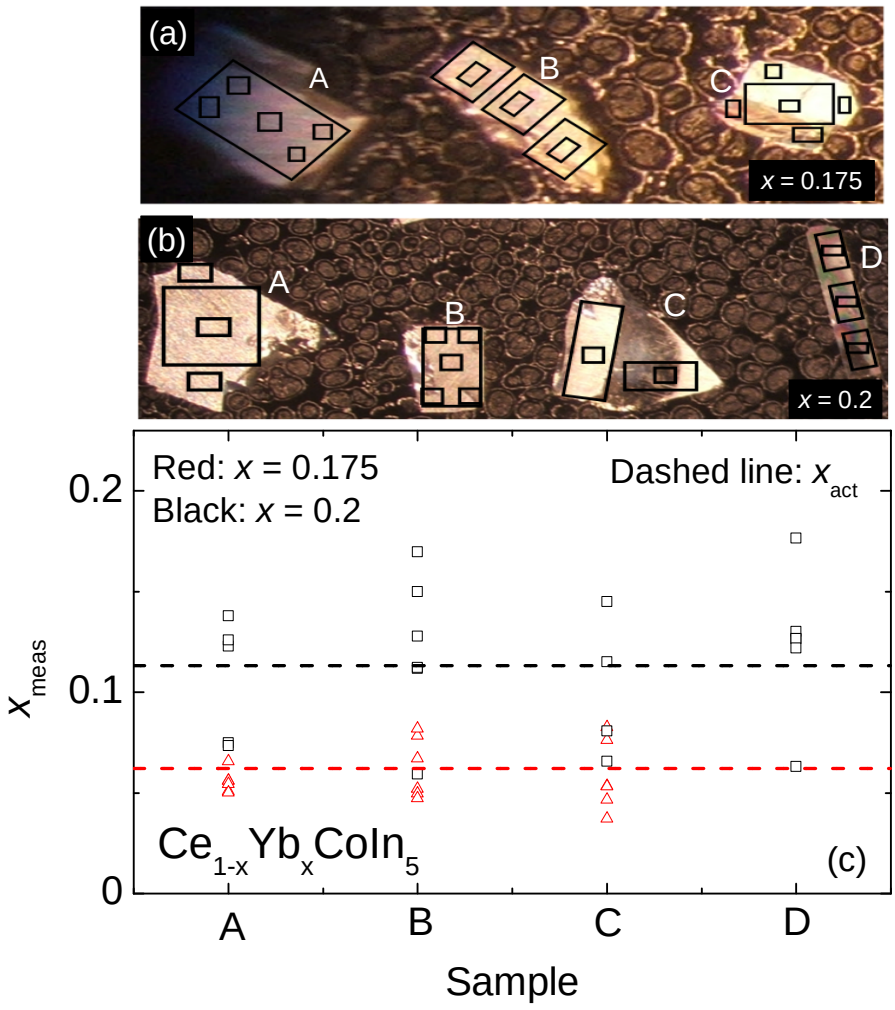

Figure VI.4: Illustration of method for acquiring EDS data on the single crystals. Two samples with $x = 0.175$ and 0.2 were affixed to conducting carbon tape for EDS measurements labeled with the letters A, B, C, and D. The EDS measurements were made on each sample within several different regions with varying sizes enclosed by the black rectangles. The results of the measurements are plotted as the red and black solid circles for $x = 0.175$ and 0.2, respectively. The dashed lines represent the average value of the data and are denoted as x_{act} in Fig. 3 for each of the two concentrations.

VI.C.3 Wavelength dispersive x-ray spectroscopy (WDS) measurements

Wavelength dispersive x-ray spectroscopy (WDS) measurements were performed using a JEOL JXA-8200 electron microprobe on all samples used in the London penetration depth study [10] and several representative samples at other nominal concentrations of Yb, including samples with Yb from different sources. The composition of each single crystal was measured at twelve different locations on typically 0.5×0.5 mm^2 samples and averaged, yielding statistical error of compositional measurement of about $\Delta x = \pm 0.005$. This error bar is substantially smaller than that of the EDS measurements because of the weakness of the Yb line, which causes the EDS measurements to have significantly lower spectral resolution and a small signal to noise ratio. The M-lines of Yb as measured in materials with Yb^{3+}, YbF_3 and $YbRh_2Si_2$ are shown in Fig. 5(a) and in Fig. 5(b) for data normalized at the peak position. The data for $YbCoIn_5$ and $Ce_{1-x}Yb_xCoIn_5$ with a nominal Yb concentration of $x = 0.40$ are also shown in Figs. 5(a) and (b). Two features in the data should be noted. First, the M-lines in compounds with Yb^{3+} are slightly shifted with respect to the lines in both $YbCoIn_5$ and $Ce_{1-x}Yb_xCoIn_5$, where the lines coincide. These observations are consistent with an Yb valence that is different from 3+ in $Ce_{1-x}Yb_xCoIn_5$ compounds for the whole series and are in agreement with previous spectroscopic measurements of the Yb valence [3, 8]. This result provides direct evidence that Yb substitution induces hole doping, similar to Cd substitution [19]. Furthermore, both direct comparison of the spectra in Fig. 5(a) and more quantitative analysis of x, taking into account mutual absorption, show that the actual Yb concentration $x_{\rm act}$ is proportional to and smaller in magnitude than the nominal Yb concentration x, roughly by a factor of 3, as shown in Fig. 3.

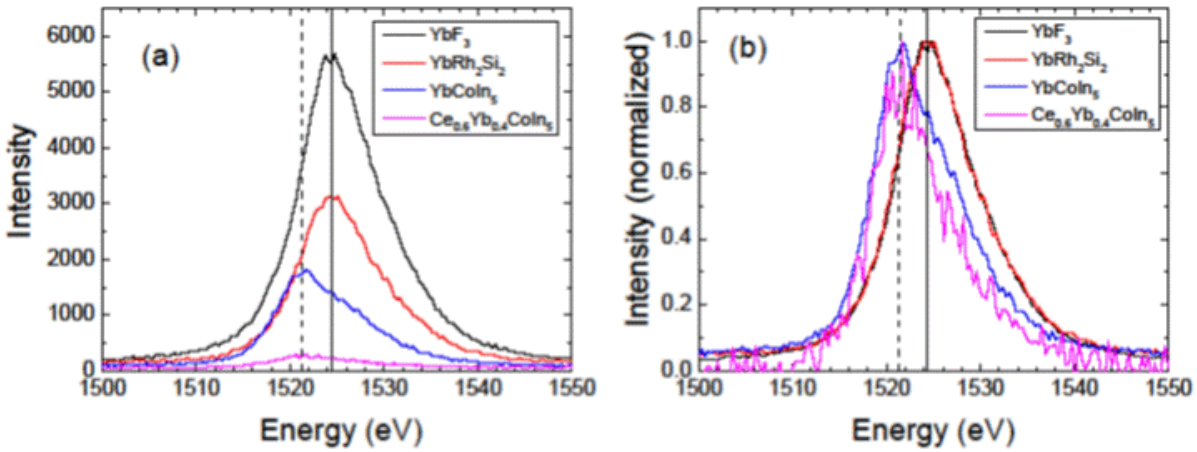

Figure VI.5: Results of wavelength dispersive x-ray spectroscopy (WDS) measurements performed on samples used in a penetration depth study [10] for two representative samples with nominal Yb concentrations $x = 0.4$ and $x = 1$ and two compounds in which Yb is trivalent, YbF_3 and $YbRh_2Si_2$. (a) M-line of Yb for the four compounds. (b) Data in Fig. VI.5(a) normalized at the peak position. Note that the M-lines in the compounds with Yb^{3+} are slightly shifted with respect to the lines in both $YbCoIn_5$ and $Ce_{1-x}Yb_xCoIn_5$, where the lines coincide. These observations are consistent with an Yb intermediate valence of 2.3+ for $Ce_{1-x}Yb_xCoIn_5$ in the range $0.2 \leq x \leq 1$.

VI.C.4 Transmission X-ray absorption spectroscopy (TXAS) measurements

To determine the Ce and Yb concentrations relative to Co from x-ray absorption spectroscopy, the absorption step heights at the Ce and Yb L_{III} edges and the Co K edge were measured in transmission. The advantage of transmission measurements is that they do not just detect the atoms near the surface of the material, but instead probe all the atoms of interest, since the x-ray beam passes through the sample. The drawback is that they also detect atoms associated with inclusions that consist of the flux (in this case, indium) or impurity phases. For each thin powdered sample, transmission data were collected at the same point on the sample. The transmission step height is a direct measure of the number of atoms in the beam; using thin layers minimizes the effects of sample pinholes and inclusions. We have also checked that using a thicker sample (twice as thick) gives the same step-height ratios. Examples at the Yb L_{III} and Co K-edge are shown in Fig. 6. To obtain the atomic ratios, we first normalize each step by the known absorption step per atom for that element, from the MacMaster x-ray absorption cross-sections [20]; then the atomic ratios are given by the ratios of these normalized step heights. Assuming the Co site is fully occupied, this ratio directly gives the Yb or Ce concentration. The errors in such concentration measurements are about 5%. A similar approach was used to determine the Zn concentration in Zn doped $LiNbO_3$ [21]. The measured Ce concentrations are close to the nominal values, but the Yb concentrations are much lower than expected. The Yb concentrations are plotted in Fig. 3(b), which shows x_{act} vs. x, for two samples with nominal Yb concentrations of 0.3 and 0.4.

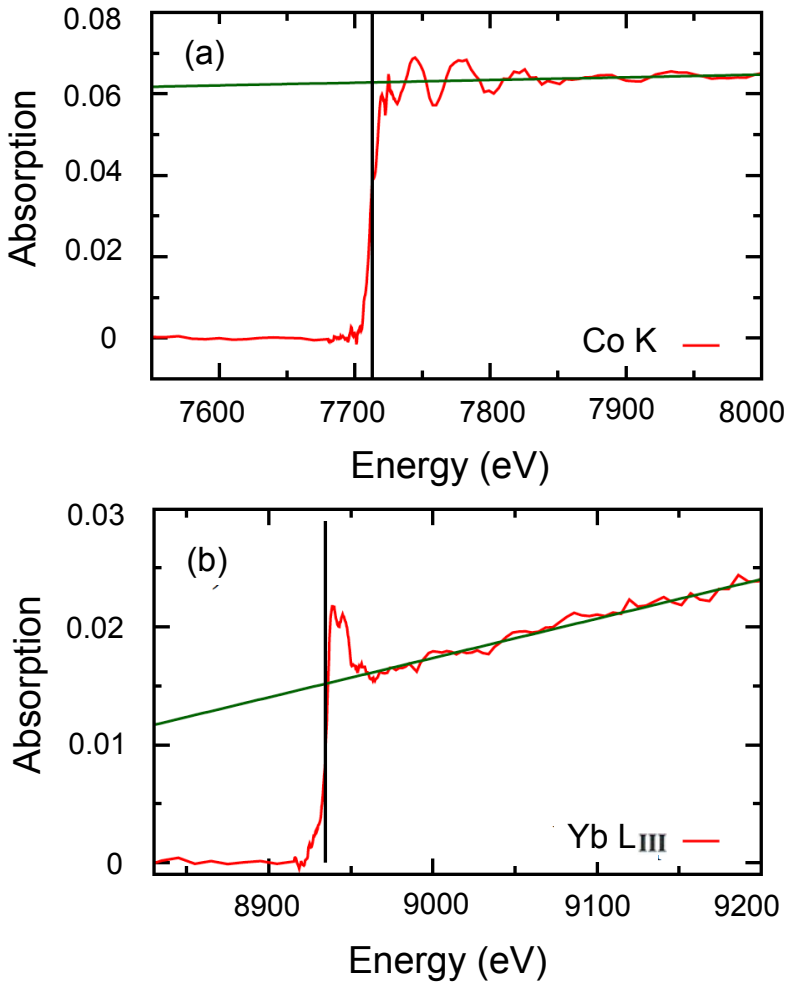

Figure VI.6: Plots of the Co K (a) and Yb L_{III} (b) edges after a linear pre-edge subtraction, which sets the pre-edge region at zero. A straight line fit above the edge shown as a black line, provides an estimate of the step height at the edge. The data just above each edge that contain the XANES structure were not included in this straight line fit.

VI.C.5 Correction of the T vs. Yb concentration phase diagram

The values of the actual Yb concentration, $x_{\rm act}$, determined from the Vegard's law procedure and supported by the measurements of $x_{\rm act}$ described above, can now be used to correct the T vs. Yb concentration phase diagram proposed in Refs. [1, 2]. In Fig. 7, the values of the superconducting critical temperature T_c are shown vs. the actual concentration $x_{\rm act}$, and compared to the data for the studies on thin films by Shimozawa *et al.*. [6] The T_c vs. $x_{\rm act}$ phase boundary for both the bulk single crystal and thin film measurements are in good agreement with one another, which supports the procedure to determine the actual Yb concentration we have employed in this work. A revised phase diagram that includes the T_c vs. $x_{\rm act}$ phase boundary and the dependence of the Kondo lattice coherence temperature T^* on $x_{\rm act}$ is displayed in Fig. 8. The only remaining discrepancy between the behavior of bulk single crystals and thin film samples is that, while T^* is monotonically suppressed in the thin film samples with increasing $x_{\rm act}$, T^* increases with increasing $x_{\rm act}$ above $x_{\rm act} \sim 0.25$ in single crystals. While we do not understand the origin of this discrepancy, we note that the thin film samples differ from the single crystals through the presence of the substrate, arrested a-lattice parameter, etc. [6].

This revision of the phase diagram of $Ce_{1-x}Yb_xCoIn_5$ does not change any of the interesting physics that has been found for this extraordinary system, but simply readjusts the concentration at which various phenomena occur. In particular, we now conclude that the valence transition of Yb from 3.0+ to 2.3+ occurs between $x = 0$ and $\sim$0.07.

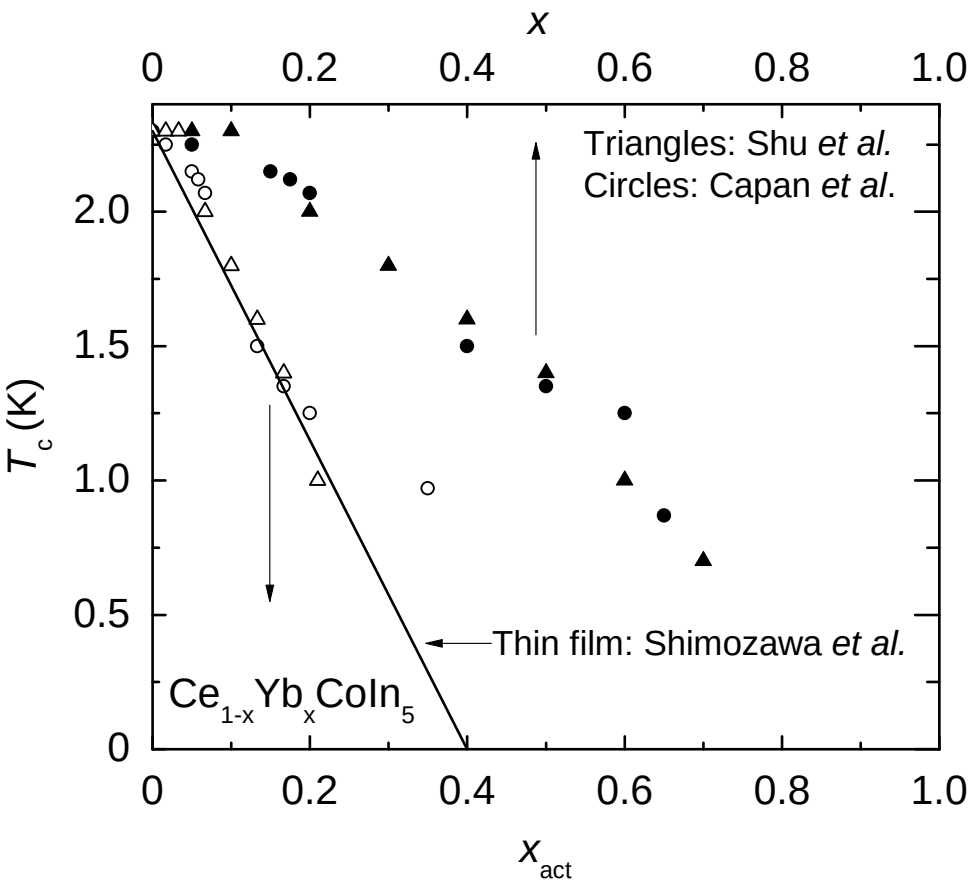

Figure VI.7: Superconducting critical temperature T_c, determined from measurements of $\rho(T)$ vs. x for $Ce_{1-x}Yb_xCoIn_5$. The data of Shu *et al.* [2] (filled circles) and Capan *et al.* [1] (filled triangles) for flux grown single crystals are plotted vs. x, where x represents the nominal concentration (upper horizontal axis). The unfilled circles and triangles indicate those same T_c values plotted vs. $x_{\rm act}$, where $x_{\rm act} \approx x/3$ represents the actual Yb concentration (lower horizontal line). The solid line indicates the evolution of T_c with x for thin film samples reported by Shimozawa *et al.*. [6] In the case of the thin films, the actual concentration is identical to the nominal concentration x.

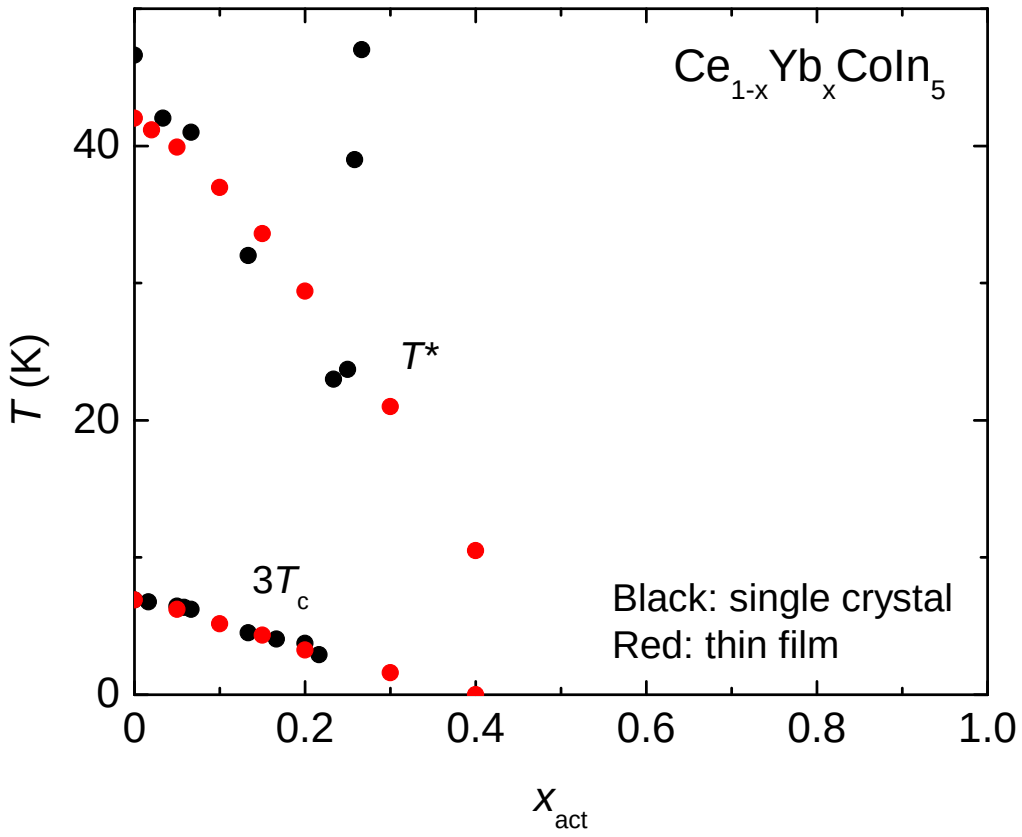

Figure VI.8: Coherence temperature T^* and superconducting critical temperature T_c vs. actual Yb composition, $x_{\rm act}$, for flux grown single crystals [2] and thin films. [6] The actual Yb concentration $x_{\rm act}$ for the single crystals was inferred from the nominal concentration as described in the text, while $x_{\rm act}$ for the thin films is the same as the nominal Yb composition.

VI.D Concluding remarks

The analysis involving Vegard's law and the spectroscopically-determined valences of Ce and Yb in the $Ce_{1-x}Yb_xCoIn_5$ system have yielded estimates of the actual Yb concentration $x_{act} \approx x/3$ for x below $\sim$0.5. The relation between x_{act} and x derived from this analysis is supported by the results of EDS, WDS and TXAS measurements reported in this work.

The subnominal Yb concentration encountered in $Ce_{1-x}Yb_xCoIn_5$ single crystals is not without precedent for other substituents in $CeCoIn_5$. For instance, Cd, Hg, and Sn substitution on the indium site occurs at fractional values of the nominal concentration [19, 22, 23]. In addition, there is a strong preference for substitution on the In(1) site [3], which has implications for how the electronic structure is tuned. Similar obstacles are also seen for Pt and Ru substitution. [23, 25] Moreover, in the case of $CeCo_{1-x}Ru_xIn_5$, not only is the measured x less than the target x, but it is also seen that the Ru ions form clusters in the 115 lattice (at least on the surface of the flux grown crystals). [25] There is evidence that such problems may also be found in other transition metal substitution series: *e.g.*, the broad region of coexistence of antiferromagnetism and superconductivity in the T-x phase diagram for $CeCo_{1-x}Rh_xIn_5$ may suggest phase separation in localized regions of individual crystals. [26] An exception to these difficulties is seen for lanthanide substitution of the Ce site (*e.g.*, in $Ce_{1-x}R_xCoIn_5$ (R = Y, La, Pr, Nd, Gd, Dy, Er, and Lu)), which appears to be straightforward. [27, 28, 29]

However, as we have described above, R = Yb substitution is problematic and occurs only at fractional values of the nominal concentration, similar to what is seen for substitution on the indium and transition sites. This result accounts for our earlier reports of an exceptional T-x phase diagram for $Ce_{1-x}Yb_xCoIn_5$ and, upon rescaling of x, our phase diagram is now in close agreement with that of thin films of $Ce_{1-x}Yb_xCoIn_5$. Notably, it is important and interesting that the actual concentration x_{act} is in registry with the nominal concentration x of the starting

material in the molten In flux. As a result, none of the interesting physics that has been found for this extraordinary system is changed; the various electronic transitions and phenomena simply occur at an actual Yb concentration $x_{\rm act} \approx x/3$ for x below ∼0.5. In particular, we now conclude that the valence transition of Yb from 3.0+ to 2.3+ occurs between $x = 0$ and ∼0.07. As we noted above, Vegard's law is ordinarily used to determine changes of valence of lanthanide ions with unstable valence when the lanthanide sites are completely occupied by lanthanide ions. In the present case, we use the known valences of the Ce and Yb ions as a function of x, determined from spectroscopy, and Vegard's law to estimate the actual concentration $x_{\rm act}$ of the Yb ions. This resolves the discrepancy between the variation of the coherence temperature T^* and the superconducting critical temperature T_c with Yb substituent concentration in the $Ce_{1-x}Yb_xCoIn_5$ bulk single crystals and thin films.

Acknowledgements

A portion of the text and data presented in Chapter 4 are reprints of material that appears in "Resolution of the discrepancy between the variation of the physical properties of $Ce_{1-x}Yb_x$xCoIn$_5$ single crystals and thin films with Yb composition" S. Jang, B. D. White, I. K. Lum, H. Kim, M. A. Tanatar, W. E. Staszheim, R. Prozorov, T. Keiber, F. Bridges, L. Shu, R. E. Baumbach, M. Janoscheck, M. B. Maple, Philosophical Magazine **94**, 4219 (2014). The dissertation author was the first author of the article.

Bibliography

[1] C. Capan, G. Seyfarth, D. Hurt, B. Prevost, S. Roorda, A.D. Bianchi and Z. Fisk, Eur. Phys. Lett. **92**, 47004 (2010).

[2] L. Shu, R.E. Baumbach, M. Janoschek, E. Gonzales, K. Huang, T.A. Sayles, J. Paglione, J. OBrien, J.J. Hamlin, D.A. Zocco, P.C. Ho, C.A. McElroy, and M.B. Maple, Phys. Rev. Lett.**106**, 156403 (2011).

[3] C.H. Booth, T. Durakiewicz, C. Capan, D. Hurt, A.D. Bianchi, J.J. Joyce, and Z. Fisk, Phys. Rev. B **83**, 235117 (2011).

[4] B.D. White, J.J. Hamlin, K. Huang, L. Shu, I.K. Lum, R.E. Baumbach, M. Janoschek, and M. B. Maple, Phys. Rev. B **86**, 100502(R) (2012).

[5] A. Polyakov, O. Ignatchik, B. Bergk, K. Gotze, A.D. Bianchi, S. Blackburn, B. Prevost, G. Seyfarth, M. Cote, D. Hurt, C. Capan, Z. Fisk, R.G. Goodrich, I. Sheikin, M. Richter, and J. Wosnitza, Phys. Rev. B **85**, 245119 (2012).

[6] M. Shimozawa, T. Watashige, S. Yasumoto, Y. Mizakami, M. Nakamura, H. Shishido, S.K. Gho, T. Terashima, T. Shibauchi, and Y. Matsuda, Phys. Rev. B **86**, 144526 (2012).

[7] T. Hu, Y.P. Singh, L. Shu, M. Janoschek, M. Dzero, M.B. Maple, and C.C. Almasan, Proc. Natl. Acad. Sci. USA **110**, 7160 (2013).

[8] L. Dudy, J.D. Denlinger, L. Shu, M. Janoschek, J.W. Allen, and M.B. Maple, Phys. Rev. B **88**, 165118 (2013).

[9] Y.P. Singh, D.J. Haney, X.Y. Huang, I.K. Lum, B.D. White, M. Dzero, M.B. Maple, and C.C. Almasan, Phys. Rev. B**89**, 115106 (2014).

[10] H. Kim, M.A. Tanatar, R. Flint, C. Petrovic, R. Hu, B.D. White, I.K. Lum, M.B. Maple and R. Prozorov, arXiv:1404.3700v1 [cond-mat.supr-con] (2014).

[11] Y. Song, M. Liu, B. White, B. Maple and P. Dai, APS March Meeting **59**, 1 (2014).

[12] L. Vegard, Z. Physik **5**, 17 (1921).

[13] O. Erten and P. Coleman, arXiv: 1402.7361v1 [cond-mat.supr-con] (2014).

[14] A. C. Larson, and R. B. Von Dreele, "General Structure Analysis System (GSAS)," Los Alamos National Laboratory Report LAUR 86-748 (2000).

[15] M. B. Maple and D. Wohlleben, Phys. Rev. Lett. **27**, 511 (1971).

[16] M. B. Maple and D. Wohlleben, AIP Conf. Proc. **18**, 447 (1974).

[17] V. S. Zapf, E. J. Freeman, E. D. Bauer, J. Petricka, C. Sirvent, N. A. Frederick, R. P. Dickey, and M. B. Maple, Phys. Rev. B **65**, 014506 (2001).

[18] H.M. Rietveld, J. Appl. Cryst. **2**, 65 (1969).

[19] L. D. Pham, T. Park, S. Maquilon, J. D. Thompson, and Z. Fisk, Phys. Rev. Lett **97**, 056404 (2006).

[20] W.H. MacMaster, N. Kerr Del Grande, J.H. Mallett and J.H. Hubbell, Compilation of X-Ray Cross Sections, UCRL-50174 Section II Revision I, Lawrence Livermore National Laboratory Report, 1969, available from National Technical Information Services L-3, U.S. Dept. of Commerce.

[21] F. Bridges, J. Castillo-Torres, B. Car, S. Medling and M. Kozina, Phys. Rev. B **85**, 064107 (2012).

[22] E. D. Bauer, C. Capan, F. Ronning, R. Movshovich, J. D. Thompson, and J. L. Sarrao, Phys. Rev. Lett. **94**, 047001 (2005).

[23] K. Gofryk, F. Ronning, J. X. Zhu, M. N. Ou, P. H. Tobash, S. S. Stoyko, X. Lu, A. Mar, T. Park, E. D. Bauer, J. D. Thompson, and Z. Fisk, Phys. Rev. Lett. **109**, 186402 (2012).

[24] C. H. Booth, E. D. Bauer, A. D. Bianchi, F. Ronning, J. D. Thompson, J. L. Sarrao, J. Y. Cho, J. Y. Chan, C. Capan, and Z. Fisk, Phys. Rev. B **79**, 144519 (2009).

[25] M. N. Ou, K. Gofryk, R. E. Baumbach, S. S. Stoyko, J. D. Thompson, J. M. Lawrence, E. D. Bauer, F. Ronning, A. Mar, and Y. Y. Chen, Phys. Rev. B **88**, 195134 (2013).

[26] J. R. Jeffries, N. A. Frederick, E. D. Bauer, H. Kimura, V. S. Zapf, K. D. Hof, T. A. Sayles, and M. B. Maple, Phys. Rev. B **72**, 024551 (2005).

[27] J. Paglione, T. A. Sayles, P. C. Ho, J. R. Jeffries, and M. B. Maple, Nature Phys. **3**, 703 (2007).

[28] R. Hu, Y. Lee, J. Hudis, V. F. Mitrovic, and C. Petrovic, Phys. Rev. B **77**, 165129 (2008).

[29] C. Petrovic, S.L. Bud'ko, V.G. Kogan and P.C. Canfield, Phys. Rev. B **66**, 054534 (2002).